Rotor-stator spinning disc reactor

Document Version:
Publisher's PDF, also known as Version of Record (includes final page, issue and volume numbers)

Please check the document version of this publication:

• A submitted manuscript is the version of the article upon submission and before peer-review. There can be important differences between the submitted version and the official published version of record. People interested in the research are advised to contact the author for the final version of the publication, or visit the DOI to the publisher's website.
• The final author version and the galley proof are versions of the publication after peer review.
• The final published version features the final layout of the paper including the volume, issue and page numbers.

[Link to publication](#)

ROTOR-STATOR SPINNING DISC REACTOR

A STUDY ON THE USE IN FERMENTATION PROCESSES

Proefschrift

ter verkrijging van de graad van doctor
aan de Technische Universiteit Eindhoven,
op gezag van de rector magnificus prof. dr. S.K. Lenaerts,
voorzitter van het College voor Promoties,
in het openbaar te verdedigen op maandag 19 juni 2023 om 13:30 uur

door

Christianus Johannes Wouterus Hop

geboren te Dongen.

Dit proefschrift is goedgekeurd door de promotoren en de samenstelling van de promotiecommissie als volgt:

Voorzitter:	prof. dr. E. Rebrov
1^e promotor:	prof. dr. ir. J. van der Schaaf
2^e promotor:	prof. dr. F. Gallucci
Leden:	Prof. Dr. Dipl. -Ing. K.-O. Hinrichsen (TU München)
	prof. dr. ir. M. van Sint Annaland
	prof. dr. ir. N.G. Deen
	prof. dr. D.Z. Machado de Sousa (WUR)

Het onderzoek of ontwerp dat in dit proefschrift wordt beschreven is uitgevoerd in overeenstemming met de TU/e Gedragscode Wetenschapsbeoefening.

Two things are infinite:
the universe and the human stupidity;
and I'm not sure about the universe.

Albert Einstein

TU/e

Christianus Johannes Wouterus (Vince) Hop
Rotor-Stator Spinning Disc Reactor -
A Study on the Use in Fermentation Processes
Eindhoven University of Technology, 2023

CONTENTS

NOMENCLATURE

Latin

$\langle k \rangle$	Resolved turbulent kinetic energy	$m^2\ s^{-2}$
A	Absorbance	$-$
a_{GL}	Specific surface area	$m^2_{int}\ m^{-3}_R$
B_m	Parameter activity coefficient	M^{-1}
C	Concentration	$mol\ m^{-3}$
c	Proportionality constant for r_{trans}	$-$
C_D	Drag coefficient	$-$
C_i	Concentration of species i	M
C_L	Concentration in the liquid phase	$mol\ m^{-3}_L$
C_{q_r}	Local throughflow coefficient	$-$
C_{sat}	Equilibrium concentration at the gas-liquid phase	$mol\ m^{-3}_L$
D	Dilution rate	h^{-1}
D_m	Molecular diffusion coefficient	$m^2\ s^{-1}$
D_t	Turbulent diffusion coefficient	$m^2\ s^{-1}$
D_{ax}	Axial dispersion coefficient	$m^2\ s^{-1}$

D_{CO}	Diffusion coefficient of CO in water	$2.05 \cdot 10^{-9} \; m^2 \; s^{-1}$
D_{st}	Diameter flat disc agitator	m
d_{tube}	Diameter of 1/4" Swagelok tube	$4.57 \cdot 10^{-3} \; m$
E	Engulfment rate	s^{-1}
E_{dr}	Power exerted by rotor	W
E_{RTD}	Residence time distribution curve	s^{-1}
f	Passive scalar	$-$
$F_{D,k}$	Drag force	$kg \; m \; s^{-2}$
H	Henry's constant	$mol \; Pa^{-1} \; m_L^{-3}$
h	Axial rotor-stator gap	m
h_d	Thickness of the disc	m
I	Current	A
I_0	Idle current	A
I_s	Ionic strength	M
K	Entrainment coefficient	$-$
k	Turbulent kinetic energy	$m^2 \; s^{-2}$
K_B	Equilibrium constant iodine-triiodide	M^{-1}
k_i	Reaction rate constant of species i	$M^{-4} \; s^{-1}$
k_{GL}	Mass transfer coefficient	$m_G^3 \; m_{int}^{-2} \; s^{-1}$
$k_{GL} a_{GL}$	Volumetric mass transfer coefficient	$m_G^3 \; m_R^{-3} \; s^{-1}$
k_{HB}	Consistency coefficient of the Herschel-Bulkey model	$m^2 \; s^{-2}$
L	Domain length	m
l	Path length UV/Vis cell	m
M	Frictional torque	Nm
M_C	Motor characteristic	$Nm \; A^{-1}$

N	Number of counts	$-$
n	Number of tanks in series	$-$
n_i	Number of moles of species i	mol
n_{HB}	Order of the Herschel-Bulkey model	$-$
OD	Optical density at 600 nm	$-$
P	Pressure	Pa
Q	Flow rate	$m^3\ s^{-1}$
Q_G	Gas flow rate	$mL\ s^{-1}$
Q_L	Liquid flow rate	$mL\ min^{-1}$
Q_t	Flow rate tracer	$m^3\ s^{-1}$
R	Gas constant	$8.314\ J\ K^{-1}\ mol^{-1}$
r	Radius	m
r^+	Wall normal coordinate, radial direction	$-$
R_D	Radius disc	m
R_i	Reaction rate of species i	$M\ s^{-1}$
R_s	Radius stator	m
r_s	Shaft radius	m
r_{trans}	Transition radius	m
s	Axial clearance rotor-stator	m
S_{ij}	Strain tensor	s^{-1}
T	Temperature	K
t	Time	s
u	Velocity	$m\ s^{-1}$
V	Volume	m^3
V_B	Buffer vessel	mL

v_G	Gas velocity	$m\ s^{-1}$
v_L	Liquid velocity	$m\ s^{-1}$
V_m	Volume of the mixing zone	m^3
V_R	Volume reactor	m^3
$V_{injection}$	Injection volume	m^3
V_{SD}	Volume rs-SDR	mL
V_{total}	Total volume	m^3
X	Biomass concentration	$g_{CDW}\ L^{-1}$
X_{UV}	Inlet signal UV/VIS meter	$-$
Y	Selectivity	$-$
y^+	Wall normal coordinate, axial direction	$-$
Y_{UV}	Convoluted outlet signal UV/VIS meter	$-$
z_i	Valence of ion i	$-$

Greek

α	Volume fraction	$-$
α_ϵ	Experimental parameter for ϵ_{loc}	$kg\ s^{-3}\ m^{-5/2}$
δ_B	Bödewadt layer thickness	m
δ_K	Von Kármán layer thickness	m
Δ_r	Radial rotor-stator gap	m
$\Delta_{sol}H$	Enthalpy of dissolution	$J\ mol^{-1}$
$\dot{\gamma}$	Shear rate	s^{-1}
ϵ	Energy dissipation rate	$m^2\ s^{-3}$
ϵ_L	Liquid hold up	$m_L^3\ m_R^{-3}$
ϵ_M	Molar absorption coefficient	$m^3\ mol^{-1}$
η	Kolmogorov length	m

γ	Activity coefficient	$-$
ν	Kinematic viscosity	$m^2\ s^{-1}$
ν_0	Kinematic viscosity at low shear rates	$m^2\ s^{-1}$
ν_G	Kinematic viscosity of gas	$1.53{\cdot}10^{-5}\ m^2\ s^{-1}$
ν_L	Kinematic viscosity of liquid	$1.00{\cdot}10^{-6}\ m^2\ s^{-1}$
ν_t	Turbulent viscosity	$m^2\ s^{-1}$
ν_{eff}	Effective turbulent kinematic eddy viscosity	$m^2\ s^{-1}$
ω	Rotational rate	s^{-1}
ϕ	Proportionality factor for engulfment model	$-$
ρ	Density	$kg\ m^{-3}$
τ	Residence time	s^1
τ_0	Density normalised yield stress	m^2
τ_r	Shear stress at the rotor	$N\ m^{-2}$
θ	Rotation angle around the z-axis	$-$

Subscripts

0	Initial
θ	Tangential direction
B	Bottom rotor-stator cavity
b	Begin position
$bulk$	Bulk phase
c	Continuous phase
$core$	In the core region
d	Dispersed phase
$eddy$	Referring to a single eddy
$extra$	Additional due to in- and external tubing

f	Final position	
in	Inlet	
loc	Local	
mix	In mixing zone	
out	Outlet	
r	Radial direction	
ref	Reference	
$rotor$	In the rotor region	
T	Top rotor-stator cavity	
tot	Total	
$wall$	At the wall	
x	Horizontal direction	
y	Vertical direction	
z	Axial direction	

Dimensionless numbers

Θ	Dimensionless time	$t\,\tau_{PFR}^{-1}$
C_M	Momentum coefficient	$2\mathrm{M}\,(\rho\omega^2 R_D^5)^{-5}$
C_w	Dimensionless flowrate	$Q\,\nu^{-1}\,R_D^{-1}$
Co	Courant Friedrichs Lewy (CFL) number	$u_{r,\theta,z}\,\Delta t\,\Delta_{r,\theta,z}^{-1}$
G	Gap ratio	$h_T\,R_D-1$
Pe	Péclet number	$u\,L\,D_{ax}^{-1}$
Re	Rotational Reynolds number	$\omega\,R_D^2\,\nu^{-1}$
Re_G	Gaseous Reynolds number	$v_G\,d_{tube}\,\nu_G^{-1}$
Re_h	Reynolds number with respect to axial gap	$\omega\,h^2\,\nu^{-1}$
Re_L	Liquid Reynolds number	$v_L\,d_{tube}\,\nu_L^{-1}$

Re_{ii}	Normalised Reynolds stress	$\overline{u_i'^2}\,\omega^{-2}\,r^{-2}$
Sc_L	Schmidt number	$\nu_L\,D_{CO}^{-1}$
Sc_t	Turbulent Schmidt number	$\nu_t\,D_t^{-1}$
Sh_{GL}	Sherwood	$k_{GL}\,d_{tube}\,D_{CO}^{-1}$
U	Dimensionless velocity	$u\,\omega^{-1}\,r^{-1}$
Z	Dimensionless length	$z\,L^{-1}$

Abbreviations

ADP Adenine Diphospate

ATP Adenine TriPhospate

$ATPase$ ATP synthase

CAD Computer Aided Design

CFD Computational Fluid Dynamics

$CODH$ carbon monoxide hydrogenase

$CSTR$ Continuously Stirred Tank Reactor

DIC Diagonal-based Incomplete Cholesky

DNS Direct Numerical Simulations

Fd Ferredoxin

$FDIC$ Faster Diagonal-based Incomplete Cholesky

$GAMG$ Geometric aglomerated Algebraic MultiGrid

Hyt Hydrogenase

LES Large Eddy Simulations

$MPLICU$ Multicut Piecewise Linear Interface Calculation

$NADH$ Nicotinamide Adenine Dinucleotide

$NADPH$ Nicotinamide Adenine Dinucleotide Phosphate

Nfn electron bifurcating ferredoxin dependent transhydrogenase

PCG Preconditioned Conjugate Gradient

PFR Plug Flow Reactor

$PIMPLE$ Pressure IMplicit with splitting of operator for Pressure-Linked Equations

$PISO$ Pressure Implicit Splitting Operator

$RANS$ Reynolds Averaged Navier-Stokes

Rnf ferredoxin, NAD$^+$ dependent oxireductase

$rs-SDR$ Rotor-Stator Spinning Disc Reactor

RSM Reynolds Stress Model

RTD Residence time distribution

SGS Sub-Grid Scale

$SIMPLE$ Semi-Implicit Method for Pressure Linked Equations

SS Steady State

$tf-SDR$ Thin-Film Spinning Disc Reactor

TKE Turbulent Kinetic Energy

VoF Volume of Fluids

$WALE$ Wall Adapting Local Eddy viscosity

WLP Wood-Ljungdahl Pathway

SUMMARY

The chemical industry can contribute greatly to the energy transition, reducing the utilisation of fossil based resources and promoting sustainable resources. However, sustainable resources are difficult to implement at large scale production due to its limited and non-consistent availability. Therefore, it is important to that the chemical industry changes towards smaller scale and more decentralised and flexible production as this would promote the utilisation of locally available resources (e.g. biomass, solar or wind). This however leads to challenges such as, smaller equipment and extreme conditions. A way to achieve this is by intensifying the current processes and develop novel systems that outperform the current equipment, this is generally known as process intensification. Process intensification has a broad spectrum of techniques to improve processes, such as increasing mass/heat transfer rates ans operating at higher concentrations, pressures and temperatures. One example of an intensified reactor is the rotor-stator Spinning Disc Reactor (rs-SDR). The rs-SDR uses high velocity gradients in a small spacing to create high shear forces and as a results, increasing the mass and heat transfer rates significantly. This thesis focuses on the implementation of the rs-SDR in a fermentation process. Fermentation is the utilisation of microbes (acetogens in this work) in combination with gaseous substrates to produce valuable chemicals and feedstock. However, this process in generally limited by mass transfer and the rs-SDR would therefore be an ideal solution.

First, investigations were performed towards the effect of elevated pressures on the productivity for a fermentation process in Chapter 2.

The fermentation took place with pure CO as a substrate and *Clostridium autoethanogenum* as the acetogen to produce acetic acid, ethanol and butane-2,3-diol. The goal was to study the effect of increasing the mass transfer rates on the cultivation by varying the CO pressures (2, 5 and 10 bar(a)) and gas flow rates (5, 10 and 20 mL/min). In total six different steady operations were obtained during an experiment of 3800 h and the best ethanol productivities were obtained at a CO inflow of 20 mL/min and at pressures of 5 (0.27 g/L/h) and 10 (0.24 g/L/h) bar(a). Additionally, ethanol/acetic acid selectivities of 2.1 were obtained. However, long term operation at 10 bar(a) had a negative influence on the productivity, but the selectivity at this pressure increased with a factor two. In general, the ethanol productivity and selectivity increased at elevated CO pressures. However, the CO utilisation was not efficient (CO conversion < 21%) and therefore optimisation of the CO uptake rate is still possible and with that, also an increase in productivity.

Additional to the pressure increase, an increase in mass transfer rates can be obtained by implementing the rs-SDR. Therefore, a study on the mass transfer rates in the rs-SDR was performed in Chapter 3. This work focused on the effect of gas/liquid ratios (1, 3 and 9 m_G^3 m_L^{-3}), viscosity (1, 5, 10 and 25 mPa*s) and rotational velocity of the rotor (50 to 2000 rpm). It was found that the mass transfer rate increased with increasing gas/liquid ratio and rotational velocity, but decreased with increasing viscosity. The highest value (14 m_L^3 m_R^{-3} s^{-1}) was therefore obtained with a gas/liquid of 9, viscosity of 1 mPa*s and rotational velocity of 2000 rpm. The obtained value was 60-100 times higher than conventional fermentation units, such as bubble columns and stirred vessels. Lastly, a correlation based on the power input was fitted to the experimental results for the laminar and turbulent regime. The correlation had an R^2 of 0.93 and 0.95 for laminar and turbulent flows respectively.

In order to further analyse the performance of the rs-SDR, a CFD model was developed to study the hydrodynamics in a rs-SDR with Large Eddy Simulations (LES). The work is executed in OpenFOAM in combination with the wall-adapting local eddy viscosity sub-grid-scale model (WALE) and is described in Chapter 4. During this study, experimental residence time distributions (RTD) were determined in the rs-SDR. These values were used to verify a new developed reactor model that describes the rs-SDR based on axial dispersion. The model was used in combination with the RTD results to determine the plug flow (PFR) volume fraction, Péclet number and the radial position where the flow transitions from PFR behavior into ideally mixed (CSTR). The obtained results were used

to validate the LES. The simulations were performed at four different Reynolds number, of which one was laminar, one transitional and two turbulent cases. It was found that the turbulent cases were in good agreement with the experimentally obtained results, but the other two simulations were off. Additionally, the turbulent boundary layers and entrainment coefficient agreed with correlations from literature and it was concluded that the simulations predicted the flow field in the rs-SDR well. Lastly, the turbulent behaviour was investigated from the simulated flow and it could be concluded that the intensity of the turbulence was the highest at the rim of the disc. Also, the centripetal flow has a 10% higher turbulent intensity than the centrifugal flow.

In Chapter 5, the investigation of the micromixing efficiency by the turbulent boundary layers was presented. During this work, the Villermaux-Dushman reaction in combination with an injection probe was used to experimentally determine the micromixing times at different positions between the rotor and the stator. The experimental work showed that the mixing intensity was the highest near the rotor (Von Kármán layer) and the lowest near the stator (Bödewadt layer). However, the results deviated from the engulfment model and this was due to the disturbance of the flow field by the injection probe, which was also verified by an analyses in SolidWorks. Besides the experimental investigation, a CFD model with LES in combination with WALE was constructed in OpenFOAM. This time, only simulating the top half of the rs-SDR and the simulation was validated with velocity profiles from literature. The validated flow field was used to determine the micromixing times in Matlab and the obtained results were compared with the experimental mixing times. The simulated values were within the experimental error for the inviscid core, but were deviating in the boundary layers. This was due to the difference in dimensionless gap distance, since it reduces the velocity gradient and therefore also the energy dissipation rate. The results provided new insights and more knowledge about the optimal micromixing location, namely the Von Kármán layer.

From the previous chapters, it appeared that the rs-SDR has potential to increase the productivity of CO fermentation with *Clostridium autoethanogenum* and is presented in Chapter 6. A culture was added to a buffer vessel and the microbes were circulated through the rs-SDR. During the experiments, the productivity, cell growth and cell shape was monitored by an HPLC, UV/VIS and optical microscope respectively. The rs-SDR was operated without dilution rate and a rotational rate of 100, 500, 1000 and 1500 rpm. It appeared from the experiments that no growth or product formation occurred and that the rs-SDR had a negative

influence on the microbes. Thereafter, the cells where analysed with the optical microscope and no visual change in cell shape or size was observed when analysed in Matlab. Lastly, a theoretical analyses was performed in OpenFOAM to analyse the shear effects in a rs-SDR similar flow field. According to the Tresca and the Von Mises criteria, the cell should theoretically not break by the shear forces in the rs-SDR. However, according to a death rate analyses based on energy dissipation rate, the cells should be death. Therefore it is likely that the cells are weakened by the shear forces in combination with the dissolved CO concentration. Especially, with the results in Chapter 2 showing a negative effect at 10 bar(a) and by the impeller.

Overall, this work showed that the rs-SDR is an effective reactor for mass transfer limited systems, high viscosities and mixing applications. However, to perform fermentation in the rs-SDR, another operation method is required. One possibility would be to increase the cell density, as this would increase the viscosity and global CO uptake rate. The increase in viscosity would decrease the mass transfer, hence decreasing the amount of dissolved CO and reduce the risk of CO poisoning. The increase in CO uptake rate, would remove the dissolved CO at a faster rate and reducing the CO contact time, hence reducing the risk of CO poisoning. Next to that, the microbes were pumped through the rs-SDR multiple times per hour and by reducing the flow rate, a reduction is shear exposure occurs, hence the shear effects would be lowered. In general, the fermentation still can be improved by increasing the pressure and the rs-SDR has numerous applications for which it can be deployed with the current knowledge.

CHAPTER 1

INTRODUCTION

If we knew what it was we were doing,
it would not be called research, would it?.

Albert Einstein

We are just an advanced breed of monkeys on a minor planet of a very
average star. But we can understand the Universe. That makes us something
very special.

Stephen Hawking

This thesis studies the implementation of a rotor-stator spinning disc reactor (rs-SDR) in a microbial CO conversion process. During this research, investigations were performed on a bioreactor with elevated pressure and within the rs-SDR, a study on mass transfer rates in viscous systems, turbulence properties, mixing efficiency and shear influence on microbes.

1

1.1. Process Intensification

Currently, the chemical industry is highly dependent on the utilisation of fossil resources (e.g. oil and gas) [1], which results in large emission of greenhouse gasses, such as CO_2. In order to reduce the emission to net-zero by 2050 [2], a transition from fossil into sustainable resources is crucial. Even though sustainable resources can be found everywhere, often they are difficult to utilise and implement in large scale production processes, due to the limited and non-consistent availability (e.g. solar- and wind energy). Therefore, the chemical industry should focus on utilising the sustainable resources more flexible and efficient. Generally, process improvements help to reduce the utilisation of resources and feedstock, and lead to a reduction in equipment size. Hence, smaller equipment results in a more controlled operation, faster responses to deal with energy fluctuations and lower operational/capital costs, while maintaining or improving the production [3, 4]. This is called process intensification and generally focuses on: increasing the heat- and mass transfer rates and operating at higher concentrations, pressures and temperatures [5, 6]. This can result in more small-scale, flexible and decentralized production, hence a reduction in sustainable resource utilisation. This can contribute greatly to the energy transition from fossil into sustainable resources [7]. This thesis focuses therefore on enhancing the transfer of gaseous substrates into the liquid phase, since this is generally a limitation in non-intensified and large scale reactors.

Currently many multiphase processes are limited by its ability to transfer one phase to another and/or the homogeneity of the system, goodness of mixing. The mass transfer rates are determined by the driving force between the two phases (e.g. pressure difference), the interfacial area or the mass transfer coefficient (e.g. bubble or particle size), of which the latter is a function of the power input (e.g. stirring speed) [8, 9]. The mixing is controlled by the amount of energy that is dissipated in a system, mixing time is proportional to the energy dissipation rate [10] and is correlated to the amount of turbulence in a system [11]. The higher levels of turbulence in a chemical reactor would: increase the interfacial surface area, reduce the diffusion path length and increase the homogeneity of a system [12]. Therefore, intensified reactors are often operated in the turbulent regime. However, highly turbulent reactors tend to be difficult to predict due to its chaotic nature and the wide scale of turbulent eddies at which kinetic energy is distributed in turbulent flows [13].

1.2. ROTOR-STATOR SPINNING DISC REACTOR

An intensified reactor that has proven to significantly enhance mass transfer rates is the rotor-stator spinning disc reactor (rs-SDR, see Figure 1.1). This reactor consists out of a rotating disc (rotor) and is surrounded by a stagnant casing (stator), the spacing between the rotor and stator is only a few millimeters [14, 15]. The combination of the high rotational velocities of the rotor and the small rotor-stator gap are resulting in very high shear forces, hence a highly turbulent flow field in the rs-SDR that intensifies heat and mass transfer rate. In general the rs-SDR has great potential for gas-liquid [16, 17], liquid-liquid [18–22] and liquid-solid [22–24] systems. Also, due to cooling channels being present in the stator, high heat transfer rates are obtained [25, 26]. This reactor can also be used for macro- [27, 28], meso- [29] and micromixing [30, 31] applications.
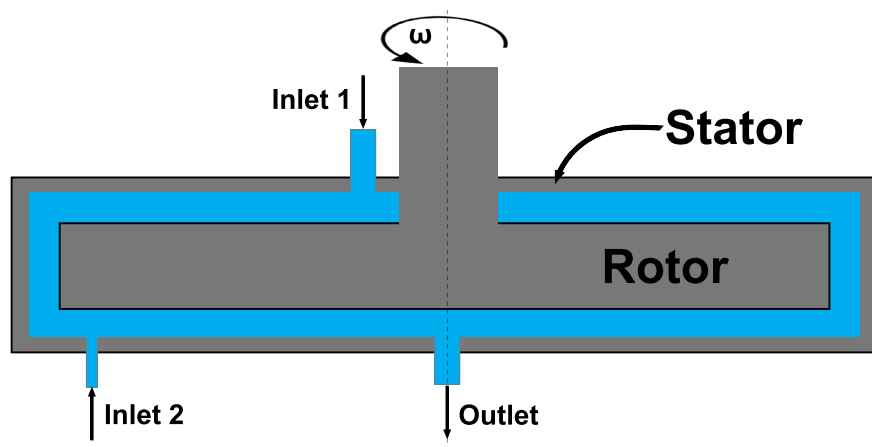
Figure 1.1: Schematic representation of the rs-SDR with an injection port (inlet 2).

On a macroscopic level, the flow behaviour in the rs-SDR with throughflow is divided into two parts. At the lower radial positions (close to the inlet and outlet), a throughflow governed regime exists which behaves as plug flow (PFR). At higher radial positions (close to the rim of the disc) the hydrodynamic behaviour is rotation governed and can be assumed as ideally mixed (CSTR). The transition point between the two varying regimes is based on the flowrate and the rotational rate [32–34]. Within this flowfield, two turbulent boundary layers are formed at high Reynolds numbers, namely a Von Kármán boundary layer (near the rotor) and a Bödewadt boundary layer (near the stator) [35, 36]. These boundary layers can be either merged or separated by an inviscid core [37, 38] and are

1

dependent on the Reynolds number and the dimensionless rotor-stator distance.

More fundamental studies on describing the hydrodynamic behaviour inside the rs-SDR were generally performed with Computational Fluid Dynamics (CFD). The computational work was mainly executed by applying an extended version of Reynolds Avaraged Navier-Stokes simulations (RANS), the Reynolds Stress Model (RSM) [39–41], and Large Eddy Simulations (LES) [42, 43]. The investigations were focused on the validation of the flowfield and describing the flow patterns inside the rs-SDR, but were only done for a single rotor-stator cavity instead of the complete rs-SDR. Additionally, fundamental studies were performed to determine the boundary layer thickness [44, 45] and developing a predictive model that determines the pressure, torque and velocity of the rs-SDR [46].

1.3. COMPUTATIONAL FLUID DYNAMICS

Turbulent structures can be described by mathematical models [47] and is known as Computational Fluid Dynamics. CFD solves the Navier-Stokes equations by numerical discretisation, since no analytical solutions are available. There are multiple approaches to perform CFD simulations and the three most common methods are Reynolds Averaged Navier-Stokes simulations (RANS) [48, 49], Large Eddy Simulations (LES) [50, 51] and Direct Numerical Simulations (DNS) [52, 53]. The RANS technique focuses on solving the Navier-Stokes equations for time-averaged values. The flow field is decomposed into a time averaged value and a fluctuating component. However, with this decomposition an additional term in the Navier-Stokes arises, which represents the turbulent stresses (Reynolds stresses). As a results, the system of equations becomes unclosed and therefore a closure model to solve the Reynolds stresses is required [49]. Since this CFD approach is based on time-averaging, the complexity of the turbulent behaviour is often not completely captured. In order to increase the accuracy of the simulation, LES can be used. The LES method spatially averages the Navier-Stokes equations by applying a filter function. This approach allows to resolve all the large scale eddies, which contain the most turbulence, and the small scale eddies are modelled with closure models [54]. The advantage of LES is that it will resolve all the turbulent structures up to a set filter size, but without resolving the smallest scale eddies, hence less computationally expensive and still statistically accurate [51]. However, LES is more computationally expensive than RANS and LES might be too computationally intensive to resolve large and highly

turbulent systems. Even though, LES solves the majority of the turbulent structures, the small scale eddies are not captured. To resolve also the small scale structures, DNS is required. DNS solves the Navier-Stokes equations numerically and does not use filter functions or averaging of the flow properties. However, DNS requires more computational resources and is therefore computationally more expensive than LES. Therefore, DNS is currently only applicable for small domains, such as flow around an object (e.g. bubble, droplet or solid body) [52, 53]. However, DNS is a useful tool to study the hydrodynamics on a detailed level, which is difficult to do with experiments. As a summary, Figure 1.2 presents the three different approaches and schematically depicts the accuracy of each approach, note that DNS also represents the instantaneous velocity.
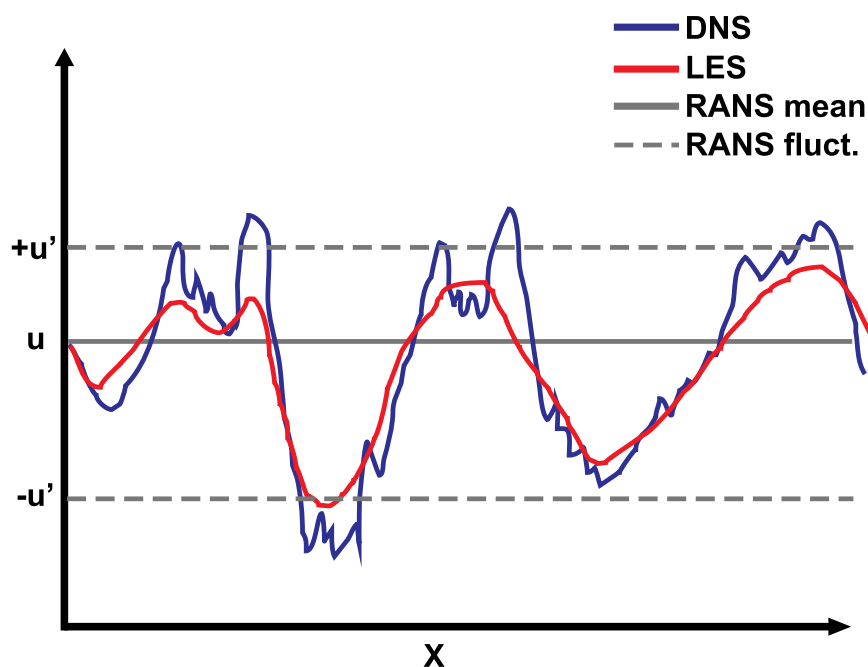
Figure 1.2: Schematic comparison between the different CFD methods, with the distance on the x-axis and the instantaneous velocity on the y-axis. Additionally, for RANS the time averaged velocity and the upper and lower limits of the fluctuating velocity (u') are schematically depicted.

Understanding the hydrodynamic behaviour of turbulent flows leads to a more predictable and efficient operation of reactors, which could be used to intensify reactors. Another way to impose process intensification is the usage of sustainable resources, such as biomass and the recycling

of effluent streams. For example, the production of syngas (mixture of CO_2, CO and H_2) from biomass could help the production of sustainable fuels or feedstock for multiple industries [55] and reduce the emission of greenhouse gasses.

1.4. SYNGAS FERMENTATION

The production of syngas is generally done by the gasification of coal or, in a more sustainable way, biomass [56, 57]. The syngas can be converted into valuable products (e.g. propylene glycol, methanol, dimethyl carbonate), which majorly occurs via metal-based catalytic processes that require high temperature and pressures [58]. However, these process conditions result in large energy consumptions and as a consequence more greenhouse emissions. Therefore, alternative routes towards the production of valuable chemicals are necessary. One of these alternatives is the microbial conversion of syngas towards alcohols, organic/carboxylic acids or other chemicals (e.g. butane-2,3-diol, n-caproate and poly-3-hydroxybutyrate) [59, 60]. Syngas fermentation generally takes place by utilising acetogenic bacteria that convert syngas via the Wood-Ljungdahl pathway, also known as the reductive acetyl-CoA pathway [61, 62]. This process is executed at slightly elevated temperature (30-40 °C), atmospheric pressures and high selectivities are obtained [63, 64].

Currently, industrial scale fermentation is performed in large batch reactors, continuously stirred vessels (CSTR) and bubble columns [63, 65]. Three of the first companies to successfully implement large scale fermentation towards etha- nol were, INEOS Bio in Florida (USA), Coskata in Pennsylvania (USA) and LanzaTech with pilot scale plants in New Zealand and China [66]. However, currently the total combined ethanol production by fermentation is only a fraction (< 1%) of the total world capacity of around 26 billion litre [67] and therefore optimisation steps are needed. Especially with these large scale fermentators being gas to liquid mass transfer limited [68].

Intensification steps that researchers are developing/executing generally consist out of more efficient usage of the microbes in combination with reducing the gas to liquid mass transfer limitation. Since dissolving the gasses are related to the concentration gradient between the gas and liquid phase, increasing the pressure (increased solubility) and decreasing the bubble size (increased contact area) are two of the potential improvements. Increasing the total pressure resulted into an enhanced production of the chemicals, but a rapid increase in pressure lead to a negative effect on the productivity [69–71]. Therefore, operations at elevated pressure have

potential, but the pressurisation speed needs to be low. A reduction in bubble size could be achieved by sparging or increasing the power input (e.g. stirring speed) [72–74], it was shown that with decreasing bubble size and higher agitator speed the productivity increased. However, these techniques are generally limited by the mechanical properties of the system, and a design that could deliver high power input without breaking the cells would have great potential [75]. Other intensification steps are, improving the process conditions [76], recycling of the liquid [77], biofilm deposition on packing/membranes [78] or different substrate compositions [79, 80], but these methods are still limited by the mass transfer rates or mechanical designs. Therefore a novel reactor design, such as the rs-SDR, could bring great possibilities.

1.5. THESIS OUTLINE

This thesis investigates whether it is possible to implement the rs-SDR into a syngas fermentation process and investigate if it would be compatible with the industrial standard. The work focuses on enhancing the mass transfer rates for syngas fermentation with *Clostridium autoethanogenum* by increasing the pressure and the usage of an intensified reactor, the rs-SDR.

Chapter 2 contains the experimental investigations towards fermentation at elevated CO pressures. This system was operated continuously for multiple liquid dilutions and total CO pressures of 2, 5 and 10 bar(a). It was found that the increase in pressure resulted in an increase in productivity and selectivity towards ethanol. However it seemed that the high pressures had negative effects over longer periods of time (930 h) and therefore a more intensified system was required to reduce the pressure, but maintaining high mass transfer rates.

Chapter 3 focuses on mass transfer rates in a rs-SDR as a function of viscosity, rotation speed, and gas and liquid velocities. The tested viscosities were 1, 5, 10 and 25 mPa*s and the gas ratios 1, 3 and 9 ($m_G^3 m_L^{-3}$). During the experiments it was found that the mass transfer rate increased with increasing power input and gas/liquid ratio, but decreased with increasing viscosity.

Chapter 4 focuses on simulating a complete stage of a rs-SDR with OpenFOAM. The simulations were done by applying LES with a Wall-Adapting Local Eddy viscosity (WALE) model in OpenFOAM and the model was validated and verified with experimentally obtained residence time distributions and correlations from literature. The results were used to determine where the highest turbulent intensity was present, at the rim

1

of the rotor and overall, the centripetal flow contains more turbulence than the centrifugal flow. As a result, the death rate of the microbes could be estimation since it is correlated to the energy dissipation rate.

Chapter 5 contains investigations on the micromixing efficiency by the turbulent boundary layers in a rotor-stator cavity. During this research, micromixing times were obtained experimentally at different rotor-stator distances and compared with results obtained from CFD simulations with LES and WALE in OpenFOAM. It was observed that the mixing intensity is the highest in the Von Kármán layer and the lowest in the Bödewadt layer. As an addition, the CFD results confirmed the experimentally obtained mixing times.

Chapter 6 investigates the applicability of the rs-SDR on CO fermentation with *Clostridium autoethanogenum*. This study contains an experimental analysis based on the productivity, cell density and morphology (size and shape). Additionally, a theoretical study towards the relation between the death rate and shear forces and a CFD study was performed on the forces acting on a single cell in a turbulent field. During the experiments no growth, product formation or change in morphology was observed. However, the theoretical study resulted in contradicting conclusions, since the cells should start decaying based on the death rate, but the CFD simulations in OpenFOAM showed that the shear forces are not large enough to cause damage to the cell wall. Therefore, it is likely that the cells are not breaking, but staying intact and become death/inactive.

Chapter 7 summarises the obtained results and provides an outlook.

CHAPTER 2

SYNGAS FERMENTATION AT ELEVATED PRESSURES

2
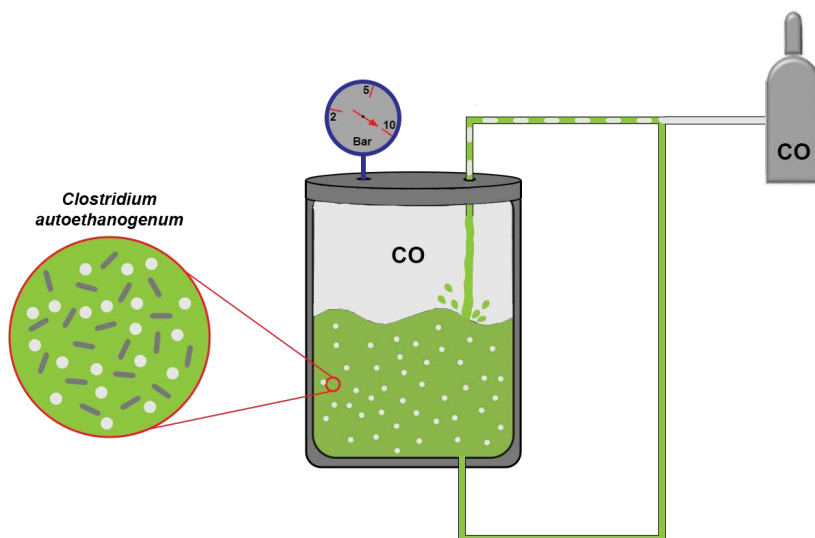
Abstract

Greenhouse gas emissions need to be reduced to net-zero in 2050 in order to limit global warming to 1.5 °C. As one of the major emitters, the chemical industry could carry out a pivotal responsibility in achieving this target. Fermentation of CO-containing flue gas into valuable or feedstock chemicals is an example of a contribution to this industrial pivot. This biological upcoming process often makes use of acetogens, such as Clostridium autoethanogenum. Gas fermentation processes are generally limited by mass transfer, and elevated pressure cultivation could contribute to improving this. Studies on the effects of elevated CO pressure on the microbial catalyst are scarce however. Therefore, this work aimed to study the cultivation of Clostridium autoethanogenum at elevated CO pressures of 2, 5 and 10 bar(a) and different gas flow rates (5, 10 and 20 mL/min). During operation, six different steady states were achieved. The best ethanol productivities (0.27 and 0.24 g/L/h) were obtained at 20 mL/min for 5 bar(a) and 10 bar(a) respectively. This study showed that ethanol productivity increased with increasing CO pressure.

2.1. INTRODUCTION

Greenhouse gas emissions need to be reduced to net-zero in 2050 in order to limit global warming to 1.5 °C [81]. The chemical industry carries a pivotal responsibility to contribute to this goal, being one of the major emitters [82]. Many of these efforts concern the chemical valorization of carbon dioxide (CO_2), the most potent greenhouse gas. In addition, chemical industry needs to transition away from fossil sources, and towards sustainable carbon resources to provide in the need of valuable hydrocarbons. A way to achieve both, CO_2 reduction and a shift away from fossil resources is by producing hydrocarbons from biomass. A potential route is the production of synthesis gas (syngas), a mixture of CO_2, CO and H_2 via the gasification of biomass. Thereafter, the syngas can be converted towards valuable fuels or commodity chemicals, enabling use by multiple industries, such as the chemical, food or pharmaceutical industry [55].

Currently, metal-based catalytic processes provide an outcome to effectively convert syngas into valuable hydrocarbons. Chemical conversion routes under investigation are the hydrogenation of methanol and catalytic ethanol production [58]. Another widely performed and researched process for the hydrogenation of C_1 feedstock (CO_2 and CO) is the Fischer-Tropsch process [83]. However, catalytic processes are energy intensive and suffer from catalyst poisoning (e.g. sulfur or phosphor) [84]. Therefore, the attention over the past decades has extended to syngas conversion using biological processes. Several microbes are able to convert this gas mixture into valuable chemicals, with high selectivities and in a milder temperature range (30-40 °C) compared to conventional processes [63, 64].

This work focuses on the anaerobic conversion of syngas by the acetogenic bacterium *Clostridium autoethanogenum*. This microorganism employs the Wood-Ljungdahl pathway, also known as the reductive acetyl-CoA pathway [61], for the conversion of syngas into various products, such as acetic acid, ethanol and butane-2,3-diol [62]. The pathway is described in more detail in Supporting Information A.1. These components are both valuable chemical feed-stocks as well as valuable products themselves. Especially butane-2,3-diol is a highly valuable component, and its downstream products are estimated to have a global market value of $43 billion in sales [85].

Fermentation processes using microbes like *C. autoethanogenum* are commonly performed in stirred tank reactors or bubble columns [86]. However, cell growth and productivity are restricted by the ability of these reactors to transfer sufficient gas into the liquid phase towards the

microorganisms [68, 80]. To obtain reasonable product concentrations and high product volumes, relatively high reactor volumes are required. This makes the economic feasibility of scaling up gas fermentation processes challenging. In order to compete with rates achieved by metal-based catalysts and fossil based processes, an increase in mass transfer rates is required.

The mass transfer rate for gas liquid processes depends on the concentration gradient (P·H - C_L) between the equilibrium concentration at the gas-liquid interface (Henry's law: C_{sat} = P·H) and the dissolved gas concentration in the liquid phase (C_L), see Equation 2.1, where $k_{GL}a_{GL}$ is the gas-liquid mass transfer coefficient and H Henry's constant for gas solubility. Equation 2.1 shows that the mass transfer rate can be increased by increasing the partial pressure and the gas-liquid transfer coefficient, the latter is a function of the power input (e.g. agitator speed, gas and liquid flow rates) [9].

$$\frac{dC_L}{dt} = \frac{k_{GL}a_{GL}}{\epsilon_L}(P \cdot H - C_L) \qquad (2.1)$$

Previously, successful attempts were done to increase the conversion rates of *C. autoethanogenum* by improving the mass transfer or steering the microbial metabolism. Abubackar et. al. was able to increase the ethanol titer to 0.9 and 4.5 g/L in a fed batch reactor by changing the pH during an experiment to increase the activity of different enzymes and with that the ethanol concentration [62, 76]. Heffernan et. al. increased the mass transfer of a continuous stirred vessel by changing the agitation speed, reaching productivities for biomass, acetic acid and ethanol of 0.5, 6.0 and 6.3 g/L/day respectively [80]. Researchers were able to establish a system that consumed 0.18 mol/L/h of CO in a bubble column with an internal liquid recycling loop. They also reached biomass, acetic acid, ethanol and butane-2,3-diol concentrations of 4.4, 6.8, 12.5 and 0.9 g/L respectively [77, 87, 88]. However, by the authors knowledge, no experiments with *C. autoethanogenum* were performed at higher pressures to increase the gas solubility and how this affects the microbial catalysts and production behaviour.

Studies performing fermentation at higher pressures were primarily done with other microorganisms, and are summarized in a review from Hecke et. al. [71]. It appears that an increase in pressure has a positive effect below 10 bar(a), above that the activity of the microorganisms generally starts to decrease. A study by Stoll et al. concluded that the pressurisation speed (tested 4-6 bar/h) also affects the microbial activity

and that reducing the pressurisation velocity was beneficial for microbial activity [69].

Building on the knowledge from previous studies, this work studied the effects of an increased CO pressure on *C. autoethanogenum*. The process was fed with pure CO at fixed dilution rates. To minimize negative pressurization effects on the microbe, the system was pressurised with a rate of 1 bar/day. The system was operated at 2, 5 and 10 bar(a). In addition to pressure, the gas flow rate was also increased for mass transfer enhancement. During operation the effect on cell growth, productivity, product selectivity and CO consumption was tracked. Our results show that increasing the pressure leads to an increase in ethanol productivity and higher ethanol/acetic acid ratio.

2.2. Experimental section

2.2.1. Bacterial strain and cultivation

Clostridium autoethanogenum (DSM 10061) obtained from the DSMZ strain collection (Braunschweig, Germany), was used for this study. *C. autoethanogenum* was cultivated anaerobically at 37 °C in a medium containing (per liter): 0.4 g KH_2PO_4, 0.53 g $Na_2HPO_4 \cdot 2\,H_2O$, 0.3 g NH_4Cl, 0.3 g NaCl, 0.1 g $MgCl_2 \cdot 6\,H_2O$, 0.01 g $CaCl_2 \cdot 2\,H_2O$ and 0.5 mg resazurin. The medium was supplemented with the following trace-elements (per liter): 1.8 mg HCl, 0.062 mg H_3BO_3, 0.061 mg $MnCl_2$, 0.944 mg $FeCl_2$, 0.065 mg $CoCl_2$, 0.013 $NiCl_2$, 0.067 $ZnCl_2$, 0.013 $mgCuCl_2$, 0.4 mg NaOH, 0.0173 mg Na_2SeO_3, 0.0294 mg Na_2WO_4, 0.0205 mg Na_2MoO_4. 200 mL of medium was dispensed in 575 mL cultivation bottles, which were capped with rubber stoppers and aluminium caps. The medium was autoclaved at 2.0 bar(a) and 133 °C fro 1.5 hours. After autoclaving and when the medium had cooled down, 0.09 volume percent of a vitamin mixture was added containing (per liter vitamin mixture): 20 mg biotin, 200 mg nicotinamid, 100 mg p-aminobenzoic acid, 200 mg thiamin, 100 mg panthotenic acid, 500 mg pyridoxamine, 100 mg cyanocobalamine and 100 mg riboflavine. Per liter, 3.88 g $NaHCO_3$ was added, acting as buffer. Per liter, 0.5 mg L-cysteine HCl and 0.235 mg $Na_2S \cdot 9\,H_2O$ were added acting as reducing agents. Unless stated otherwise, pH was set to 5.75 using NaOH or HCl. Medium was amended with 1 g/L yeast extract, 1 g/L tryptone and 20 mM sodium acetate. Hereafter, the headspace gas of the bottles was exchanged with CO by utilising a vacuum pump and adding from the gas bottle, this procedure was repeated 5 times and the headspace was filled with 1.8 bar(a) of CO. Thereafter, 10 vol% was inoculated from the previous culture

(OD 0.3 - 0.4) and the bottles were cultivated in a shaker at slow speed and constant temperature of 37 °C. The culture was maintained by adding NaOH or HCl to keep the pH close to the optimum growth value of 5.75 and the headspace was refreshed regularly using CO.

When the culture reached the exponential growth phase, the culture was partially transferred to a new bottle, transferred completely into the experimental set-up or the liquid was partially refreshed.

2.2.2. EXPERIMENTAL SET-UP

Figure 2.1 shows the process flow diagram (PFD) of the used set-up. The reactor set-up consists of a double loop system. The first loop is the reaction loop (Figure 2.1, streams 1, 2 and 4) and the second loop is referred to as the sampling loop (Figure 2.1, streams 5, 6, 7, 8, 9 and 10) The reaction loop contains an unbaffled Premex autoclave reactor (V_R) with a volume of 2.6L. The reactor is equipped with a flat disc agitator, containing four equally spaced blades and a blade length of D_{st} = 0.07 m. The reactor is also equipped with a pressure sensor (ATM. 1ST 56 bar(a) from Sensor Technik Sirnach AG) and is heated by an electrical heating jacket. V_R was heated up to a temperature of 150 °C during the autoclaving process. The liquid reaction mixture is pumped out of the reactor using a Gather gear pump having a flow rate (Q_L) of 100 mL/min and controlled using a mini CORI-FLOW M12V14I by Bronckhorst. Gas enters the loop via a T-junction after stream 2 via stream 3. Here, CO and N_2 can be fed separately. For CO, the flow rate (Q_G) was set to 1, 5, 10 and 20 mL/min each via a Bronckhorst mass flow controller. The multiphase flow falls (± 0.1-0.15 m) on top of the liquid level in V_R after circa 1.5 m of 1/4" stainless steel tubing from Swagelok, enhancing gas-liquid mass transfer in the tubing. This concludes the reaction loop (stream 4). Stream 1, 2 and 4 are equipped with heat tracing, maintaining the set temperature of the process outside V_R. The pressure was regulated using an U3L (Equilibar) back pressure regulator (BPR), stream 11, with an DRP70 dual valve controller (Pressure Control Solutions) and was set to 2, 5 and 10 bar(a) during the experiments and after the BPR, the gas flow is vented.

The sampling loop in the set-up is created for sampling and to control the dilution rate (D), connected to the autoclave via stream 5 and 10. After 1635 h of continuous operation, a malfunction occurred in the pumps from streams 7 and 9 and V_B was removed from the system by adding two 3-way valves. From stream 4 a bleed flow (10 to 40 mL/min, depending on the pressure in V_R) is entering the sampling loop via stream 5. The liquid flows through a needle valve via stream 6 into a buffer vessel (V_B) of 600 mL and
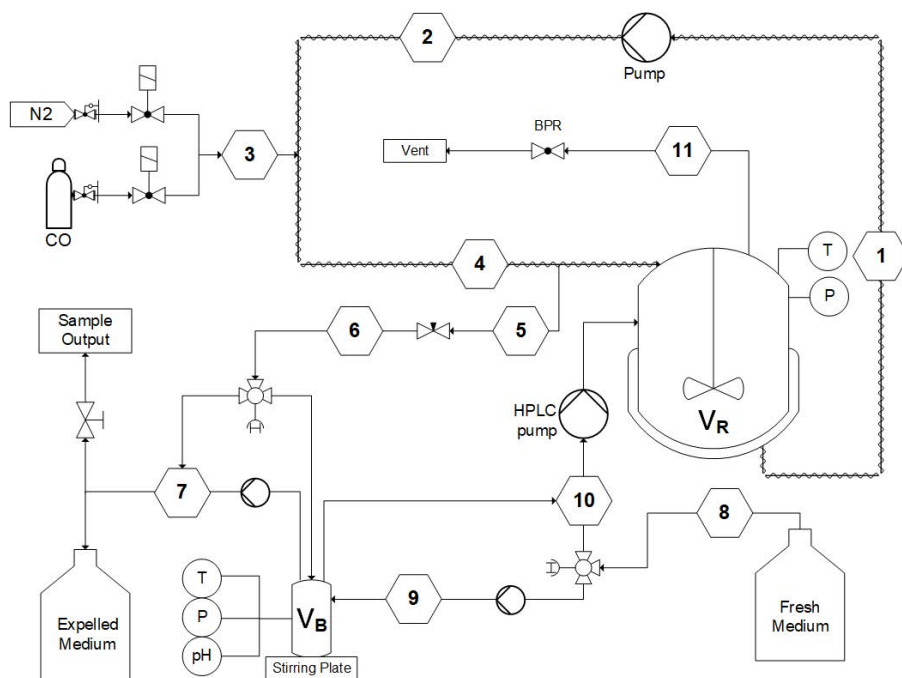
Figure 2.1: Schematic view of the experimental set-up.

after 1635 h directly into stream 7. The pressure of V_B was maintained between 1.1 and 1.5 bar(a) with a pressure sensor (ATM. 1ST 6 bar(a) from Sensor Technik Sirnach AG). The temperature was indicated with a temperature sensor (type K from TC Direkt) and the pH was measured (SP28X of Consort) and logged via pH/ORP 350 control box for logging, the temperature/pressure sensors were logged via a PLC. The pH was maintained at 5.2 ± 0.3 by manually adding 3 mol NaOH or 1 mol HCl into stream 9 or 10 after 1635 h. Furthermore, stream 7 contains a sample port for offline measurements of liquid composition (sample outlet) and also pH with a VWR pH 20 pH meter after 1635 h. At last, dilution was controlled and connected via streams 7 and 8 and maintained for at least one full dilution per experiments. Via stream 8, inflow of fresh medium in 2 L bottles was controlled using a HPLC pump of the type 101U/Shimadzu 10 AT. Outflow of medium was regulated via stream 7 using a peristaltic pump by Watson Marlow (type 101U), collecting the used medium in 2 L bottles. Depending on the dilution rate, bottles containing fresh and used medium needed to be replaced regularly. Both pumps required to operate at equal speed. In this way, an equilibrium is achieved between the addition of fresh

medium and removal of excessive medium, keeping overall liquid volume constant. At last, liquid is pumped into V_R using a Knauer HPLC pump via stream 10 from V_B and stream 8 (after 1635 h).

2.2.3. Offline analysis

Acetic acid and ethanol concentrations were analysed using high pressure liquid chromatography (HPLC) by Shimadzu of the type UFLC XR containing a LC-20AD pump, SIL-20A sampler and CTO-20AC oven, equipped with a Shimadzu Shim-pack GIST C:18 column. Measurements were performed using a Waters 2414 refractive index detector. The column operated at a temperature of 60 °C with 0.01 M H_3PO_4 eluent at a flow rate of 0.5 mL/min. Injected sample volume was 5 μL. Butane-2,3-diol concentrations were analysed via Gas Chromatography Mass Spectrometry (GCMS) by Shimadzu (GCMS QP2010) equiped with an Agilent J&W DB-200 column (length: 30m, diameter: 0.25mm, film thickness: 0.50 μm). The column was operated at 50 °C at 65.7 kPa, using He as a carrier gas.

Cell growth was estimated using a UV-2501PC UV-VIS, measuring optical density at 600 nm. Samples were measured using 1 mL disposable cuvettes with a path length of 10 mm. A correlation between optical density and grams of dry cellular weight per liter of medium was obtained (gDCW/L) and is described in Supporting Information A.2.

2.2.4. Dissolved CO concentrations

Maximum dissolved CO concentration was determined by combining Henry's law and the Van 't Hoff equation (Equation 2.2) to include the temperature (T) dependency [89]. With H(298 K) being Henry's constant at 298 K ($9.37 \cdot 10^{-6}$ mol m_L^{-3} Pa^{-1}) and $\Delta_{sol}H$ the enthalpy of dissolution (-10808.85 J mol^{-1}). This results in a maximum liquid CO concentration of 1.66, 4.14 and 8.28 mol m_L^{-3} at respectively 2, 5 and 10 bar(a), note it was assumed that the liquid keeps the same properties of water throughout the experiment.

$$H(T) = H(298K) exp \left[\frac{-\Delta_{sol}H}{R} \left(\frac{1}{T} - \frac{1}{298} \right) \right] \qquad (2.2)$$

Since there is no stirring present in V_R, it was assumed that the majority of the CO mass transfer takes place in stream 4 (Figure 2.1). The tube was placed vertically and the hydrodynamic regime is Taylor flow, therefore it was assumed that the mass transfer could be determined by the correlation proposed by Yue et. al. (Equation 2.3) [90]. The dimensionless Sherwood number ($Sh_{GL} = k_{GL} \, d_h \, D_C O^{-1}$) can be rewritten to form Equation 2.4,

with D_{CO} the mass diffusivity of CO in water ($2.05 \cdot 10^{-9}$ m^2 s^{-1} [91]) and d_{tube} the internal diameter of the 1/4" Swagelok tubing ($4.57 \cdot 10^{-3}$ m). This resulted in a $k_{GL}a_{GL}$ of 0.064, 0.075 and 0.086 m^3_G m$^{-3}_R$ s^{-1} for respectively 5, 10 and 20 mL min^{-1} of CO inflow. In Supporting Information A.3 a more detailed analysis on the dissolved CO concentration can be found and it shows that the gas flow rate has a minor effect on the concentration, but that the increase in pressure results in the biggest increase due to the increase in the saturation limit (Henry's law).

$$Sh_{GL} \cdot a_{GL} \cdot d_{tube} = 0.084 Re_G^{0.213} Re_L^{0.937} Sc_L^{0.5} \qquad (2.3)$$

$$k_{GL}a_{GL} = \frac{0.084 D_{CO}}{d_{tube}^2} Re_G^{0.213} Re_L^{0.937} Sc_L^{0.5} \qquad (2.4)$$

2.3. RESULTS AND DISCUSSION

2.3.1. PRODUCT FORMATION

C. autoethanogenum was cultivated at increasing CO pressure of 2 to 10 bar(a). To determine the effect of increased CO mass transfer rates and solubility on the fermentation process, the productivity and cell growth were tracked. The fermentation lasted for 157 days and during the operation, different gas flows, pressures and dilution rates were tested, resulting in a total of six different operations (phases) and depicted in Table 2.1. During a phase, the productivity of at least one component (biomass, acetic acid, ethanol or butane-2,3-diol) did not deviate more than 10% from the average value for a minimum of one dilution, phases 3 and 4 were 2.5 dilutions. Also, phase 1, 2 and 4 are repeated during another fermentation experiment and these results are shown in Supporting Information A.4.

Phase	Total P (bar(a))	Q_G (mL/min)	D (h^{-1})	Time (h)
1	2	5	0.012	96
2	2	10	0.016	97
3	5	10	0.015	166
4	5	20	0.034	71
5	10	20	0.027	49
6	10	20	0.002	928

Table 2.1: The experimental condition for every phase with the total pressure (P) of the system, gas flow rate (Q_G), dilution rate (D) and duration. Note, the total pressure is the measured pressure and contains therefore also fractions of CO_2.

The fermentation profile is depicted in Figure 2.2 and it shows the biomass and product concentrations over time. Above the graph are two rows, representing the pressure and gas flow at that time. Note that the bars between the different pressures are wider and it denotes the transition between the two pressure set points. The colored areas are the six different phases (see Table 2.1) and the time stirring speed was set to 500 rpm. In Supporting Information A.5 a more detailed description of the different events that took place during this experiment can be found.
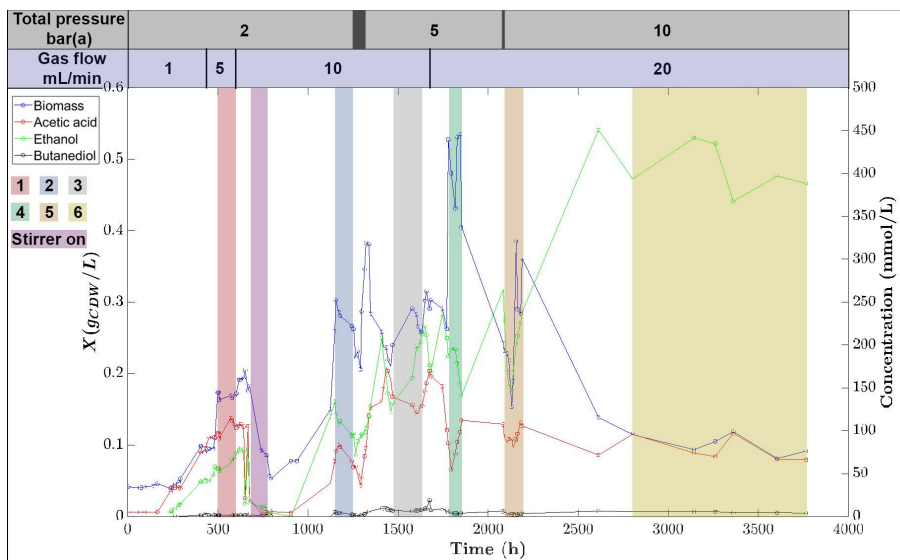

Figure 2.2: Products and biomass formed during CO fermentation by *C. autoethanogenum*. Color coded sections indicate the 6 different phases that were investigated during operation. Above the graph are the tested conditions and the numbers in the legend denote the different phases according to Table 2.1.

With an increasing gas flow rate, an increase in biomass/product concentration is observed (Figure 2.2). This observation suggests mass transfer limitation and is in line with literature that shows that an increase in mass transfer rate results in an increase in productivity [68, 80]. When the stirrer was given a set point of 500 rpm, a sharp decline in biomass/product concentration was observed, defined as "*Stirrer on*" in the figure (Time = 675-771 hours). Due to this negative effect it was decided to switch the stirrer off and not to use it again during the remainder of the experiment. Since the shape of the agitator was chosen to have the least amount of shear [92] and that successful operation in reactors with higher shear rates were performed in literature [76, 80, 93], shear is unlikely to be the cause

of this activity decline. More likely, negative effects were caused by CO poisoning since the sudden increase in CO concentration might be too steep for the metabolism to reduce CO poisoning effects [94]. In the case of *Clostridium ljungdahlii*, CO poisoning eventually decreases cell density [95]. Because *C. autoethanogenum* has similar properties to *C. ljungdahlii* one could infer that the sudden increase in dissolved CO might explain the negative influence of setting on the stirrer.

The increase in pressure is also depicted in Figure 2.2 and it can be observed that increasing the total pressure of the system from 2 to 5 bar(a) results in a positive effect on the biomass/product concentration, however the increase from 5 to 10 bar(a) resulted in a decrease in biomass. This effect was also observed in literature for *Clostridium ljungdahlii* [69, 71, 96]. During phase 6 an increase in ethanol selectivity (up to 4.5 mol ethanol/mol acetic acid) is observed due to the low dilution rates and this could have resulted in product inhibition since the cell density decreases [97]. As can be seen in Table 2.3, 4.5 mol/mol is also an uncommonly high value during continuous fermentation with *C. autoethanogenum*. Also, the higher ethanol concentration reduces the surface tension which may affect the bubble size and therefore the mass transfer in the system [98]. As a result, it is not clear how the mass transfer rate influences the product selectivity.

Phase	Productivity (mg/L/h)			
	Biomass	**Acetic acid**	**Ethanol**	**butane-2,3-diol**
1	2.03 ± 0.05	75.5 ± 6.78	33.2 ± 3.31	1.89 ± 0.16
2	4.47 ± 0.25	71.0 ± 8.89	83.4 ± 10.99	6.18 ± 1.64
3	3.99 ± 0.28	115.3 ± 6.34	127.1 ± 21.18	9.59 ± 0.89
4	16.49 ± 1.91	174.1 ± 40.33	274.8 ± 35.04	12.20 ± 1.86
5	8.15 ± 2.07	151.4 ± 14.86	241.0 ± 43.23	8.18 ± 1.95
6	0.20 ± 0.09	9.38 ± 1.72	37.2 ± 2.64	0.89 ± 0.14

Table 2.2: Growth rate and product formation at the 6 different phases as was shown in Table 2.1.

The average productivity of the components in Figure 2.2 are summarised in Table 2.2. It can be concluded that the highest productivity is reached during phase 4, followed by phase 5. However, the standard deviation is higher during phase 5 in comparison with 4 and the system might have not achieved steady state operation. A comparison between phases 4, 5 and values from the literature is made in Table 2.3. It depicts the obtained product/biomass concentrations and ethanol/acetic acid

selectivities at different studies, mainly bubble columns and continuously stirred vessels. The studies from literature were performed at atmospheric pressures and it can be concluded that the increase in pressure resulted in similar performance, even without optimising the reactor system. Additionally, Supporting Information A.1 showed that the addition of H_2 to the system would increase the productivity and therefore the similar productivity at higher pressures on CO solely are especially promising.
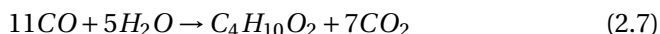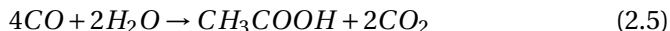
Study	Partial pressures feed (bar(a))	D (h^{-1})	Concentration (g/L)			Y (mol/mol) EtOH/Ace
			Biomass	Ace	EtOH	
Phase 4	5.0 CO	0.034	~0.5	~5.1	~8.1	~2.07
Phase 5	10.0 CO	0.027	~0.3	~5.6	~8.9	~2.07
[80]	0.23 CO & 0.68 H_2	0.021	~0.2	~2.5	~2.4	~1.23
[80]	0.02 CO, 0.23 CO_2 & 0.66 H_2	0.021	~0.5	~6.0	~9.7	~2.11
[77]	0.51 CO & 0.20 CO_2	0.063	~4.4	~6.8	~12.5	~2.40
[79]	0.61 CO	0.042	~1.4	~6.1	~3.8	~0.78
[79]	0.15 CO & 0.46 H_2	0.042	~1.4	~3.8	~11.5	~3.95

Table 2.3: Comparison based on concentration and ethanol/acetic acid selectivity between phases 4 and 5 from this study and studies found in literature. When the gas composition from literature do not reach 1.013 bar(a), the remainder is Ar or N_2. Ace = acetic acid and EtOH = ethanol, Butane-2,3-diol is not shown in this graph due to limited data availability.

2.3.2. CO consumption

The CO utilization could not directly be measured by the outflow rate and therefore a theoretical CO consumption is calculated based on the stoichiometric
biomass/product formation. Equations 2.5-2.7 contain the simplified reactions and Equation 2.8 an approximation for the biomass formation based on an overall elemental composition ($CH_{1.52}N_{0.28}O_{0.46}S_{0.0059}P_{0.042}$) presented by Norman et. al. [99].

$$4CO + 2H_2O \rightarrow CH_3COOH + 2CO_2 \tag{2.5}$$

$$6CO + 3H_2O \rightarrow CH_3CH_2OH + 4CO_2 \tag{2.6}$$

$$11CO + 5H_2O \rightarrow C_4H_{10}O_2 + 7CO_2 \tag{2.7}$$

$$9CO + 3H_2O \rightarrow 4CH_{1.52}N_{0.28}O_{0.46}S_{0.0059}P_{0.042} + 5CO_2 \qquad (2.8)$$
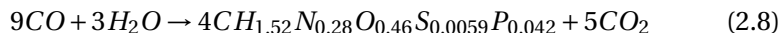
Table 2.4 presents the gas flow into the system and the CO uptake based on Equations 2.5 to 2.8 in combination with Table 2.2. It can be seen that the CO inflow is significantly higher than the theoretical CO uptake. During the fermentation, it is estimated that no more than 40% of all the CO is consumed and the CO conversion decreases with increasing CO availability. Table 2.2 shows that the CO uptake significantly reduces between phases 4 and 5, even though the productivity is comparable. When comparing with literature, the CO conversion is much lower, since CO conversion of 50% and higher were obtained [77, 79, 80]. Therefore it can be concluded that the fermentation can still be optimised further to increase the CO conversion. Especially since CO conversion values of 98% are reported in literature at higher pressures in a similar reactor system (*Clostridium ljungdahlii*) [69]. Another increase in CO conversion could be obtained by the ddition of H_2 (Table 2.3 and Supporting Information A.1), since this resulted in higher product concentrations due to more efficient usage of the Wood-Ljungdahl pathway [79], hence consumption rates. Additionally, bubbling gas into V_R to mimic the operation of a bubble column or by increasing the CO gasflow and pressure in more steps worked for *C. ljungdahlii* [95] would also be possibilities to enhance the CO consumption.

Phase	CO inflow (mmol/h)	CO uptake (mmol/h)	CO conversion (%)	P_{CO} system (bar(a))
1	23.3	9.2 ± 0.86	39.41	1.21
2	46.6	15.8 ± 2.05	34.02	1.32
3	116.4	24.4 ± 3.14	20.94	3.95
4	232.8	47.6 ± 7.23	20.45	3.98
5	465.6	40.9 ± 6.67	8.78	9.12
6	465.6	5.3 ± 4.52	1.14	9.89

Table 2.4: The CO inflow rate based on the pressure and normal gas inflow and the CO uptake rate based on the reactions given by Equation 2.5 to 2.8. The conversion is determined by the average CO uptake and the CO inflow. Additionally, the theoretical partial CO pressure is presented and the difference with the total pressure is due to the formation of CO_2.

Overall, this work shows that fermentation at higher pressures is beneficial with *C. autoethanogenum* and that the limiting factor is rather the low CO consumption rates and the potential CO sensitivity of the

cells. High mass transfer rates were achieved and the system requires an improved CO consumption rate of biological catalysis to prevent CO poisoning. This can be achieved by increasing the cell density or changing the cultivation methods, e.g. metabolic or community engineering, isolation of faster or more tolerant biocatalysts or changing gaseous substrate composition. According to Supporting Information A.1, the addition of H_2 to the system would already lead to a more efficient gas consumption. The mentioned improvements would allow higher productivities and as a result could make the biological conversion of syngas a more competitive technology. However, the elevated pressure increases the productivity, but these experiments were conducted in lab scale and by scaling up to industrial scale, multiple challenges arise (e.g. mass transfer, mixing or handling of the broth) [100–102]. These challenges lead to economic and technical problems that could make the scale-up significantly more difficult.

2.4. CONCLUSION

This study, shows that fermentation with CO at elevated pressures and *Clostridium autoethanogenum* increases the ethanol productivity. Experiments were conducted at 2, 5 and 10 bar(a), with the highest ethanol productivity, 0.27 and 0.24 g/L/h, achieved at 5 and 10 bar(a) respectively. However, when operating at 10 bar(a) for longer time (~ 930 h) a sharp decrease in ethanol productivity was observed. During the long run at 10 bar(a) the ethanol/acetic acid selectivity increased from 2.1 to 4.5 mol/mol, which is uncommon in conventional CO fermentation processes with *C. autoethanogenum*. Additionally, it was shown that the performance of the system increased with an enhancement in gas to liquid mass transfer due to increasing CO inflow and the performance was comparable with bubble columns and continuously stirred vessels at atmospheric pressures. Only in our system, the estimated CO conversion was 20 and 9% for phases 4 and 5 ,which is lower than was observed for bubble columns and continuously stirred vessels (≥ 50%). Therefore, it can be concluded that the performance of this study is comparable with literature, but the CO uptake efficiency is lower. From the observations, it appears that the system is not limited by mass transfer, but it was estimated to be limited by the CO uptake rate of *C. autoethanogenum*. Therefore, the authors suggest to apply high CO pressures at a denser cell culture (≥ 0.5 g/L) or changing the cultivation methods, e.g. different gas composition or different pH.
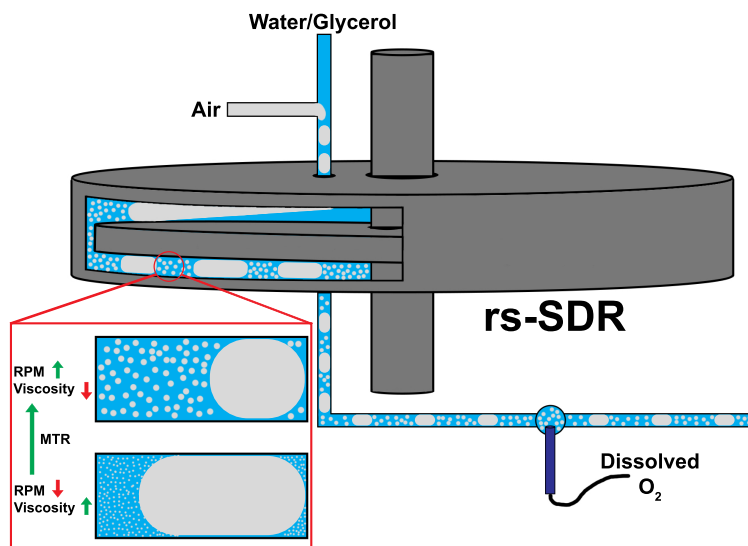
CHAPTER 3

EFFECT OF VISCOUS LIQUIDS ON THE GAS-LIQUID MASS TRANSFER RATE IN A ROTOR-STATOR SPINNING DISC REACTOR

3

Abstract

A study on the mass transfer rates in the rotor-stator Spinning Disc Reactor (rs-SDR) was performed. Previously work generally focused on the mass transfer rates in the rs-SDR for water in combination with relatively low gas/liquid ratios. Therefore, the focus of this work was to study the effect on the mass transfer rates by more viscous systems and higher gas/liquid ratios. During the investigations, the viscosity effect was tested at 1, 5, 10 and 25 mPa*s for gas/liquid ratios (ψ) of 1, 3 and 9 $m_G^3\ m_L^{-3}$. The mass transfer rate increased with increasing ψ and rotational rate, but decreased with increasing viscosity. The highest value (14 $m_L^3\ m_R^{-3}\ s^{-1}$) was found at a gas/liquid ratio of 9 in combination with a viscosity of 1 mPa*s and a power input of ~ 1 MW m_R^{-3}. Two correlations, for laminar and for turbulent flow were fitted as a function of the energy dissipation rate, viscosity and ψ. One would expect that especially the gas flow is important instead of the ratio, however it was observed that ψ influenced the mass transfer and not the flow rate. The correlation had an R^2 of 0.93 and 0.95 for laminar and turbulent flow respectively. This work can be used further to design an rs-SDR for novel mass transfer limited applications, such as viscous systems or gas absorption.

3.1. INTRODUCTION

In the past few decades, a shift towards a more intensified chemical industry has been the focus of a plethora of research studies [103]. A particular focus has been towards making chemical processes more efficient, safer and more sustainable. In the case of multiphase systems, one method of intensification can be through overcoming the mass transfer limitations from one phase to another, thereby removing an unnecessary, often limiting, step in a chemical process. Theoretically, if we consider the case of gas-liquid mass transfer, the mass transfer rate is determined by the mass transfer coefficient, the gas-liquid interfacial area, and the concentration gradient. The mass transfer coefficient itself depends on the frequency of surface renewal as proposed by the work of Higbee and Danckwerts. Furthermore, the average size of gas bubbles generated in a device, determining the gas-liquid interfacial area, depends on the shear stress on the bubbles. By using equipment which can significantly increase the shear stress and surface renewal rate, for instance with the use of high specific energy dissipation into the system, we can significantly improve on the overall mass transfer rate. As we transition our production processes to be more circular and sustainable, the use of such multiphase systems can be expected to become more prevalent. Similarly, as less solvents are used in the process industry[104, 105], it can be expected that highly concentrated and highly viscous fluids are more often encountered. The handling of such complex fluids is often challenging in conventional process equipment and low heat and mass transfer rates are often observed. Consequently, novel reactors and systems need to be developed to counteract these effects and to ensure processes have optimal resource and energy utlization. In this study we focus on a such a novel reactor which has demonstrated its capability for intensification, the rotor-stator spinning disc reactor (rs-SDR). This reactor consists of a cylindrical housing (stator) which encloses a rotating disc (rotor), with the gap between the rotor and the stator being only a few millimeters (Fig.3.1). The small gap in combination with the high rotational rate results in a highly turbulent field [37, 38] which intensifies the heat and mass transfer rates [14, 15]. In addition to a highly turbulent field, the high shear forces present in the reactor volume also results in small bubbles/droplets and increases the surface area [18, 106, 107]. The rs-SDR should also be differentiated from the thin film spinning disc reactor (tf-SDR) where the basis of intensification is based on the reduction of film thickness across a rotating disc. In general, the rs-SDR has great potential for enhancing gas-liquid [16, 108], liquid-liquid [18] and liquid-solid [23] mass transfer

rates. Moreover, high heat transfer rates [25, 26] and low mixing times [30, 31] are obtained. Furthermore, the rs-SDR has already shown to enhance productivity for more concentrated and viscous systems [20–22, 109].
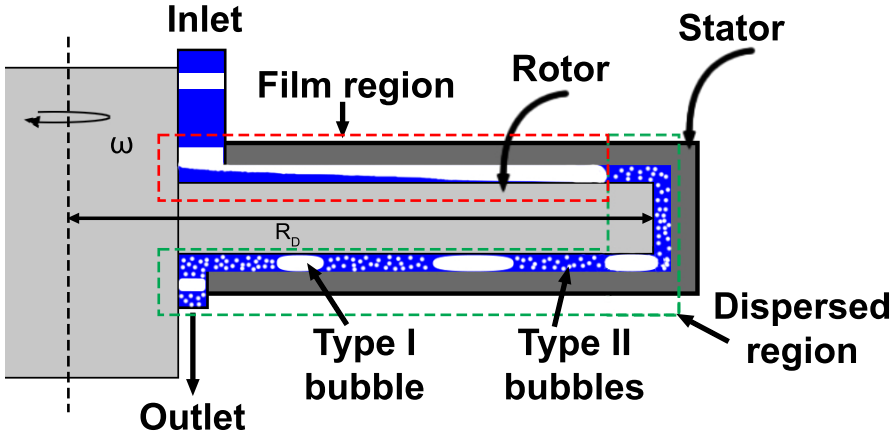

Figure 3.1: Schematic view of co-feeding gas liquid flow into the rs-SDR at the top, this representation is based on [17, 107]. The film region presents a constant gas cap and that leaves a thin liquid film on the rotor. At the higher radial positions, the rotational forces will shear of bubbles from the gas cap to form a dispersed bubble flow. In this flow there are two types of bubbles, with a radius bigger than the rotor stator clearance (type I) and a radius smaller than the clearance (type II).

In previous research, the gas-liquid mass transfer performance was experimentally investigated in the rs-SDR for non-viscous systems (water). These experiments studied the mass transfer rate by investigating multiple parameters including: co- and counter current feeding of the gas and liquid flow, the gas-liquid flow ratio, the rotor diameter, the axial and radial gap between rotor and stator, perforated and solid rotors, as well as the number of rotor-stator stages [16, 106–108, 110]. Furthermore, direct numerical simulations to determine the gas-liquid mass transfer on a single bubble were also performed [111]. While the gas-liquid mass transfer rate at higher viscosity has so far not been investigated in the rs-SDR, past studies have investigated bubbles size analyses of viscous systems in the rs-SDR [112]. On the other hand, for the tf-SDR viscous systems have been investigated both numerically and experimentally for heat and/or mass transfer rates [113]. The aim of this study is to describe the gas-liquid mass transfer for viscous liquids in a rs-SDR system, particularly focusing on the effect on the mass transfer rate due to changing the gas-liquid flow ratios and

rotational rates.

3.2. THEORETICAL BACKGROUND

3.2.1. ROTOR STATOR SPINNING DISC REACTOR

Previous research indicates that for gas-liquid systems, two regions develop in the rotor-stator cavity, a thin film and a dispersed bubble region (Figure 3.1) [106]. The film region develops due to the liquid and gas streams being injected near the center of the disc, forming a structure akin to the structure observed in the tf-SDR. The liquid flows over the rotor and completely wets the rotor [114]. However, in contrast to the tf-SDR, a large bubble (gas cap) is observed to form between the liquid film and the stator. This behaviour will continue until the shear forces are large enough to break down the gas cap into smaller bubbles and the flow will continue as a dispersed bubble flow throughout the remainder of the rs-SDR. The transition from thin film flow into dispersed bubble flow is determined by multiple parameters, e.g. the energy input, viscosity and gas/liquid flow rates [17]. The bubbles have a tangential velocity due to the movement of the liquid and the centrifugal forces causes the bubbles to flow inwards. The bubbles can possibly flow back into the film region and make them re-coalesce with the gas cap. Another flow path the bubbles could follow is between the rotor rim and the stator down into the bottom rotor stator cavity. In this region the centripetal forces causes the bubbles to flow with a spiraling motion towards the outlet of the reactor [106, 110].

Within the dispersed bubble flow, a distinction between two different kind of bubbles can be made, type I and II bubbles [17, 106, 110]. Type I bubbles are squeezed between the rotor and stator (d_b >> h). They have a wide size distribution and are irregular disc-shaped, see Figure 3.1 for a schematic representation. Type II bubbles are smaller than the rotor-stator gap (d_b ≤ h). They are spherical and have a narrow size distribution. De Beer et al. showed that the size of the bubbles decreases and the Type II bubble gas hold-up increases with increasing rotational rates [17, 110]. It was also shown that type II bubbles contribute the most to the total gas-liquid mass transfer.

3.2.2. GAS LIQUID MASS TRANSFER

The gas to liquid mass transfer ($k_{GL}a_{GL}$) depends on two terms, the mass transfer coefficient (k_{GL}) and the interfacial area between the two phases (a_{GL}). As was mentioned previously, the bubble size depends on the rotational rate. With a smaller bubbles size, a higher interfacial area

(a_{GL} = 6/d_b for spherical bubbles) is reached. k_{GL} depends on the rate of refreshment of the liquid film that is surrounding the bubble. A popular model to describe this, is the penetration model [115] and is based on the contact time (t_c) between the gas and liquid phases, see Equation 3.1.

$$k_{GL} = 2\sqrt{\frac{D}{\pi t_c}}$$
(3.1)

Literature also shows that k_{GL} depends on the turbulent intensity and can be estimated by the energy dissipation rate (ϵ in m^2 s^{-3}) [116, 117]. In order to estimate the energy dissipation, Kolmogorov's theory for isotropic turbulence offers a well accepted model [11]. Therefore, the contact time (t_c) can be estimated by the Kolmogorov time scale (Equation 3.2).

$$\tau_\eta = \left(\frac{\nu}{\epsilon}\right)^{0.5}$$
(3.2)

In combination with the prediction for Newtonian fluids of the mass transfer coefficient from Kawase and Moo-Young, Equation 3.3 was derived for the turbulent regime [118] by combining Equation 3.1 and 3.2.

$$k_{GL} = 2\sqrt{\frac{D}{\pi}}\left(\frac{\epsilon}{\nu}\right)^{0.25}$$
(3.3)

This equation was adapted by Haseidl et al. into an empirical correlation that was fitted to experimental results, see Equation 3.4 [16]. The constant were fitted to be K = 0.01, α = 0.45, β = 0.58, and γ = -0.72 and E_{dr} the energy dissipation rate in W m^{-3}. Haseidle et al. reached $k_{GL}a_{GL}$ values of 14 m^3_L/m^3_R/s and is approximately 10 times higher than reported by Meeuwse et al. [110]. These studies were all done for water. This study will aim to determine the mass transfer performance for more viscous liquids.

$$k_{GL}a_{GL} = KE_{dr}^\alpha \phi_G^\beta \phi_L^\gamma$$
(3.4)

3.3. Methods
3.3.1. Experimental Setup
The experimental set up for all experiments is the same and is depicted in Figure 3.2. The system contains a vessel, filled with demineralized water, that is constantly being bubbled with air to maintain an oxygen saturated liquid. From this vessel the saturated liquid flows, via a gear pump (Gather DS2X30) and a mass flow controller (Bronkhorst Cori-Flow) into the rs-SDR.

A Swagelok T-junction is placed $7.0 \cdot 10^{-2}$ m before the rotor stator cavity and it combines the nitrogen flow with the saturated liquid. The nitrogen is fed via a Bronkhorst EL-Flow controller. The rs-SDR consists out of a 316L stainless steel rotating disc, with a radius of $6.6 \cdot 10^{-2}$ m, and is enclosed by a 316L stainless steel cylindrical housing. Within the housing there are cooling channels to assure an isothermal operation. The cooling fluid is ethylene glycol and is cooled with a LAUDA ECO RE 620 heat exchanger, the reactor temperature is maintained at 293 ±2 K and controlled by a TC Direct Pt 100 thermocouple at the outlet of the rs-SDR. The gap between the housing and disc is $2.0 \cdot 10^{-2}$ m in both the radial and axial direction. This results in a total reactor volume (V_R) of $5.8 \cdot 10^{-5}$ m^3. The outlet stream can be switched towards the inlet vessel for recirculation or switched to a waste vessel for single pass experiments. The oxygen concentration in the liquid was measured by a dissolved oxygen (DO) sensor from Mettler Toledo (InPro 6860i) at the outlet of the reactor.
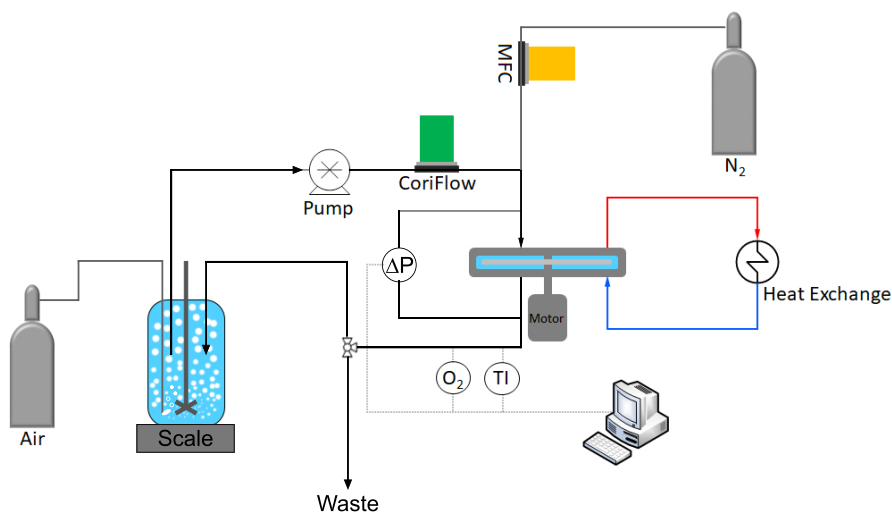

Figure 3.2: Schematic view of the experimental rs-SDR set up

To characterize the performance of the rs-SDR a number of parameters were varied during this study. One of those parameters was the rotational rate of the disc (ω) and was varied from 5 to 209 rad/s (Re = 0.2 to 9.1 x 10^5 for water). This results in a transition from laminar flow into turbulent flow for water [37]. Also, the volumetric gas flow rate was changed between three different values, $7 \cdot 10^{-6}$ m^{3}s^{-1}, $20 \cdot 10^{-6}$ m^{3}s^{-1}, and $60 \cdot 10^{-6}$ m^{3}s^{-1} and with a constant volumetric liquid flow rate the gas/liquid flow ratio was changed

(ψ = 1, 3 and 9 $m_G^3 m_L^{-3}$). Lastly, the viscosity of the liquid was varied. The viscosity was increased by mixing glycerol (>99%, Merck Life Science NV) with demineralized water, the tested viscosities were 5, 10 and 25 mPa*s.

Since the mass transfer rate is a function of energy dissipation [11], the energy dissipation rate (E_{dr}) should be determined, see Equation 3.5. To experimentally determine the E_{dr}, the power exerted on the rotor by the motor (M) was required and could be calculated by measuring the supplied current (I). The supplied current needed to be reevaluated by subtracting the internal current losses (I_0) and multiplying it by the motor characteristics, M_c = 6.47 N. I_0 was determined by measuring the current at different ω with the motor disconnected from the rotor [17].

$$E_{dr} = \omega M = \omega (I - I_0) M_c \tag{3.5}$$

3.3.2. Mass Transfer Measurements

The mass transfer measurements are taken by operating the set up (Figure 3.2) in single pass settings. The inlet vessel is saturated with air and will be stripped with nitrogen in the rs-SDR, at the outlet an oxygen sensor will measure the oxygen concentration and the stripped stream will go to the waste vessel. Desorption was used instead of absorption: in absorption mode the saturation concentration significantly varies due to pressure drop over the rs-SDR and the radial pressure variation, which overcomplicates the mass transfer analysis. Between the center of the disc and the rim, the pressure difference is up to $1.5 \cdot 10^4$ Pa [37, 39] and absorption is affected more by these pressure changes than desorption. All measurements were performed under steady state conditions and repeated at least twice. An example of two identical desorption experiments is shown in Figure 3.3. Before starting the nitrogen flow, the flow was recirculated through the rs-SDR until the system was >95% saturated (read from DO sensor). When this was reached, a nitrogen flow and a rotational rate were set. The velocity of the disc was increased when a steady O_2 concentration was obtained for at least 10 residence times. It can also be seen that for this case, almost no deviation between the two runs is present and that the liquid is almost fully desaturated (2-3% O_2 left). Note that the DO sensor is calibrated for air, therefore full saturation is with air, containing 21% O_2.

With the amount of O_2 present in the outlet stream, it is possible to calculate the mass transfer coefficient. For this calculation it was assumed that the nitrogen flow does not contain oxygen. The O_2 concentration in the gas outlet is then given by:
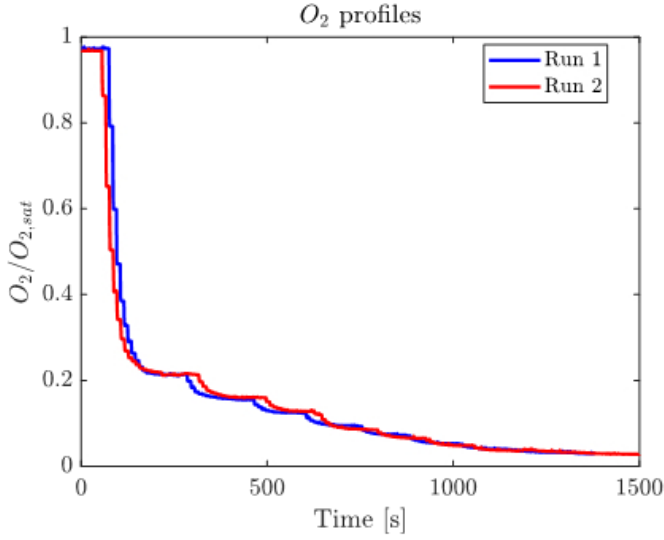
Figure 3.3: Example of two desorption experiments. Both experiments started with an O_2 saturation of >95% and every plateau is a steady state value for a specific disc velocity.

$$C_G^{out} = C_G^{in} + \psi(C_L^{in} - C_L^{out}) \qquad (3.6)$$

With C_G and C_L the O_2 concentration in the gas and liquid stream. For the gas bubbles plug flow behaviour and the liquid ideally mixed were assumed [37, 41, 107, 119] and the following equation for the gas liquid mass transfer coefficient ($k_{GL}a_{GL}$) was derived:

$$k_{GL}a_{GL} = \frac{\phi_G}{V_R} \frac{H}{RT} ln \left[\frac{\frac{RT}{H}C_G^{in} - C_L^{out}}{\frac{RT}{H}C_G^{out} - C_L^{out}} \right] \qquad (3.7)$$

With H Henry's constant and R the universal gas constant. Note that Henry's constant is reevaluated for every viscosity by recalibrating the DO probe. The film and disperse flow regions are determined by applying a dynamic operation. After a steady state was reached, the gas flow was set to zero and the O_2 saturation was measured for 2 more minutes. Thereafter, the gas flow was set to its original value and the rotational rate was changed. This procedure was repeated for all the tested rotational rates and an example of such experiment can be found in Appendix B.1.

3.4. Results and discussion

3.4.1. Mass transfer Water

Within this section, only co-current flow from the top of the rs-SDR to the bottom is discussed and the bottom to top flow configuration can be found in Supporting Information B.2. From literature it was known that the gas-liquid mass transfer coefficient increases with increasing flow ratio and this effect was also shown in Figure 3.4a [16, 106, 107, 110]. Only, in literature there was no limitation with respect to rotational rate ($\psi = 3$ and 9) and it might indicate that the gas outlet is saturated with O_2, hence limitations by the maximum O_2 that can be stripped.

Additionally, the thin film region mass transfer coefficient was also determiend by using the dynamic approach. During this operation, the static part (no gas flow) was assumed to be referring to the thin film mass transfer. The film region mass transfer coefficients are plotted in Figure 3.4b and showing the comparison between the different flow ratios and the different flow directions respectively. The first observation is, that the coefficient is around 20 times lower than the total $k_{GL}a_{GL}$ (Figure 3.4a). It also appears to have negligible effects by changing the gas-liquid ratios. The obtained mass transfer coefficients for the thin film region are also comparable with what was shown in literature for a rs-SDR [106].
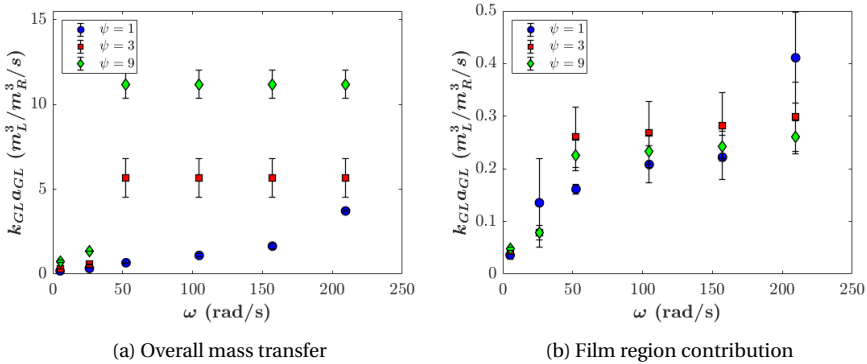

(a) Overall mass transfer   (b) Film region contribution

Figure 3.4: Volumetric mass transfer coefficient for water ($\mu = 1$ mPa*s) at the three different flow ratios with a) the total mass transfer coefficient and b) the film region mass transfer coefficient.

In order to support the statement about the physical limitations, the residence time was reduced by a factor two. These results are plotted in Figure 3.5. The graph follows the same trend as was observed in literature and gave comparable results with the work of Haseidl et al. [16]. The values

obtained are an average of two runs and seem to be consistent at every run. Only the 209 rad/s point at $\psi = 9$ has a bigger error bar and this is likely due to the amount of O_2 left, approximately 1.5%. In this lower range of saturation, small fluctuations already turn into big deviations.
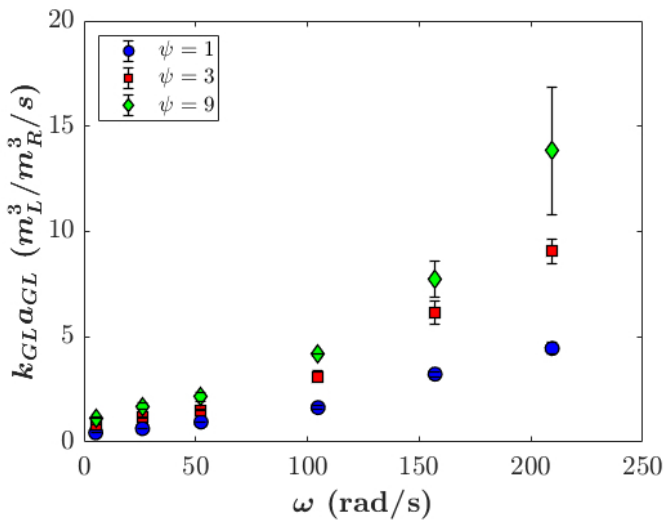

Figure 3.5: Mass transfer coefficient comparison between the three different gas ratios for top to bottom water flow, but with 0.5τ.

3.4.2. GLYCEROL

This section will only discuss the results of the total gas-liquid mass transfer rates and due to the unpredictability of the dynamic operation will not show the thin film region mass transfer coefficients, see Appendix B.1 for a more detailed explanation. The results of the total $k_{GL}a_{GL}$ are plotted in Figures 3.6a, 3.6b and 3.6c and are representing the results at $\mu = 5$, 10 and 25 mPa*s respectively. As was expected, the mass transfer coefficient decreases with increasing viscosity, because the turbulent intensity also decrease and with that the refreshment of the liquid film around the bubbles. An interesting observation is that the values of the 5 mPa*s viscosity do not follow the same behaviour as the other viscosities (including water) and that the error bars are bigger. The measurements for this viscosity were repeated six times for every gas flow, instead of the usual two to three times, and it did not change the outcome or decreased the error bar. The cause for this peculiar behaviour might be the transition from laminar into turbulent flow regimes. According to literature, the single

phase flow regime would change from laminar into turbulent regime [37, 38] at these rotational rates. The effect of gas bubbles on these boundaries is unknown, but it might be that the flow is alternating between turbulent and laminar flow. The 10 mPa*s fluid is fully laminar and water is fully turbulent (except for 5 rad/s), no such large spread in mass transfer is observed. Between Figures 3.6b and 3.6c, around 10% decrease in $k_{GL}a_{GL}$ was observed.

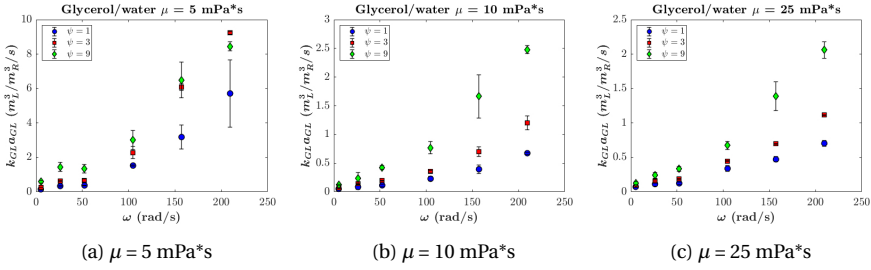(a) μ = 5 mPa*s   (b) μ = 10 mPa*s   (c) μ = 25 mPa*s

Figure 3.6: The gas-liquid mass transfer coefficient in the RS-SDR at increasing viscosity a) glycerol-water mixture with μ = 5 mPa*s, b) glycerol-water mixture with μ = 10 mPa*s and c) glycerol-water mixture with μ = 25 mPa*s

3.4.3. CORRELATIONS

In order to conclude and compare all the results directly, a common parameter is required. In this research the energy dissipation rate was used (E_{dr}), see Equation 3.5. As was discussed in the previous sections, the gas-liquid flow ratio had a large effect on the $k_{GL}a_{GL}$ and therefore the viscosities were plotted at the three different ratios in Figure 3.7. In this figure, the $k_{GL}a_{GL}$ was plotted as function of E_{dr} for the different viscosities and for the three different flow ratios (3.7a, 3.7b and 3.7c). The first observation is the distinction between two regions, μ = 1 and 5 mPa*s and μ = 10 and 25 mPa*s. It shows that 1 and 5 mPa*s follows a much steeper increase in $k_{GL}a_{GL}$ when compared with 10 and 25 mPa*s. As was mentioned before, the difference is likely due to being in the laminar or turbulent flow regime [37, 38]. Therefore, to determine a mass transfer correlation, a distinction between laminar and turbulent flows is necessary. Also, this correlation should be dependent on E_{dr}, μ and ψ.

Within literature a correlation was derived for gas liquid contacters and the mass transfer appeared to be a power law correlation based on a constant, gas flowrate and energy dissipation ($k_L = K\epsilon_d^\alpha u_g^\beta$) [120]. For this system, an adaptation was made. Since at zero energy input from the rs-SDR still O_2 transport takes place due to the gas liquid contact within

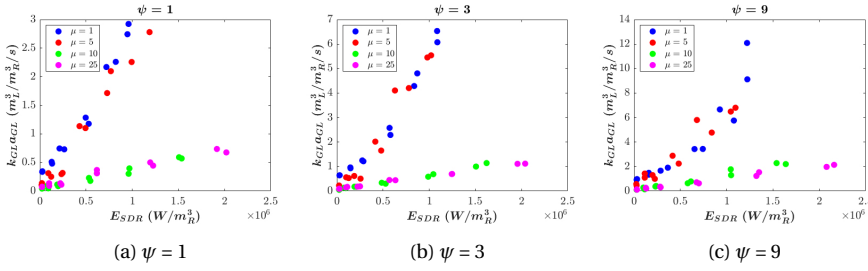(a) $\psi = 1$ (b) $\psi = 3$ (c) $\psi = 9$

Figure 3.7: The gas-liquid mass transfer coefficient as function of the energy dissipation rate (E_{dr}) in the RS-SDR with the viscosities plotted at different gas-liquid flow rate ratios a) $\psi = 1$, b) $\psi = 3$ and c) $\psi = 9$. Also, the repetition for every experiment is plotted with the usage of the same color code.

the flow, an addition of an initial mass transfer coefficient was introduced (k_0). Additionally, the effect of viscosity was added and the gas/liquid flow ratio was used instead of the gas flow. Since Figure 3.5 showed that a double flow rate and a constant ratio ($\psi = 1$), did not influence the mass transfer rates. The adapted equations are presented by Equations 3.8 and 3.9. With 3.8 being the equation for the laminar flow and the constants (K_L and α_L) were fitted to the experimental results for laminar flow ($\mu = 10$ and 25 mPa*s) by using the *lsqnonlin* function in Matlab. The averaged R^2 was 0.93 and the constants were fitted to be $K_L = 8.13 \times 10^{-8}$ and $\alpha_L = 0.35$, k_0 was determined by operating the system without a rotational rate. The same was done for the turbulent flows (Equation 3.9, $\mu = 1$ and 5 mPa*s), only there was a non-linear dependency with respect to E_{dr} and therefore a new constant (β) was introduced. The fit with *lsqnonlin* resulted in a R^2 of 0.95 and values for $K_T = 1.41 \times 10^{-9}$, $\alpha_T = 0.028$ and $\beta = 1.52$ were found. From these results it can be concluded that in the laminar regime, viscosity has the biggest contribution to the mass transfer rate, while the viscosity has significantly less impact in the turbulent regime. However, according to Equation 3.3 α and β should be 0.75 and 0.25 respectively, but Equation 3.3 does not take the interfacial area (a_{GL}) into account. Therefore, it can be assumed that the mismatch in exponent is due to the contribution of a_{GL}. Due to the contribution of the viscosity on the mass transfer coefficient, no comparison could be made between the coefficients of Haseidl et al. [16].

$$k_{GL}a_{GL} = k_0 + K_L\frac{E_{dr}\psi}{\mu^{\alpha_L}} \tag{3.8}$$

$$k_{GL}a_{GL} = k_0 + K_T\frac{E_{dr}^{\beta}\psi}{\mu^{\alpha_T}} \tag{3.9}$$

To visualise the goodness of the fit, a parity plot was created for both flow regimes, see Figure 3.8. These graphs show the fitted $k_{GL}a_{GL}$ on the y-axis and the experimental one on the x-axis, also dashed lines that represent the 20% deviations are included. It can be seen that the results fall almost completely within the confidence intervals for both the laminar (Figure 3.8a) and the turbulent case (Figure 3.8b). Thus, the correlation can be found to fit in good agreement with the experimental data.

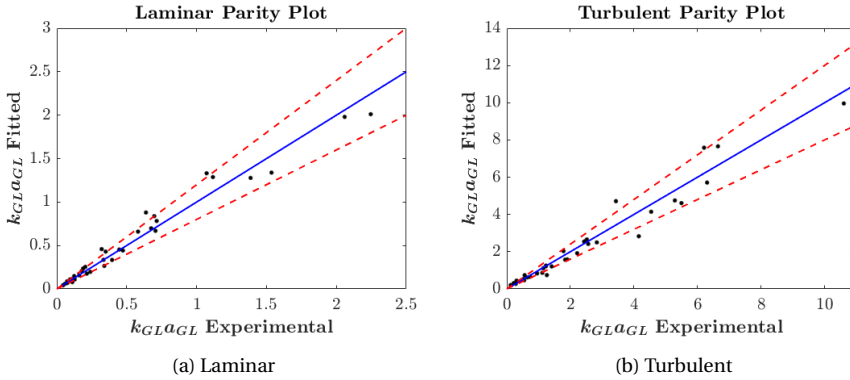(a) Laminar   (b) Turbulent

Figure 3.8: Parity plots of the fitted $k_{GL}a_{GL}$ on the y-axis and the experimental $k_{GL}a_{GL}$ on the x-axis, plus dashed lines for 20% deviation. In a) the laminar results and b) the turbulent results.

3.5. CONCLUSION

During this study it was shown that the gas-liquid mass transfer rates in the rotor stator spinning disc reactor is affected by the increase in viscosity. The experiments were conducted by increasing the viscosity (μ = 1, 5, 10 and 25 mPa*s), rotational rate (ω from 50 to 209 rad/s) and the gas-liquid flow ratio (ψ = 1, 3 and 9 m_G^3 m_L^{-3}). The obtained results for all water (μ = 1 mPa*s) experiments were comparable with literature [16] and an increase in gas-liquid mass transfer was observed with increasing gas-liquid ratio and rotational rate. With increasing viscosity a non-linear decrease in the transfer rate was observed together with a clear distinction between the laminar and turbulent flow regimes. Therefore, two correlations, based on the energy dissipation rate (E_{dr}), gas-liquid flow ratio (ψ) and the viscosity (μ), were proposed. Both correlations (Equations 3.8 and 3.9) were fitted to the experimental data by using the *lsqnonlin* function from Matlab and resulted in a R^2 of 0.93 and 0.95 for the laminar and turbulent correlations respectively. All fitted values were within 20% deviation (as was also

observed by Haseidl et al. [16]) from their experimental counterparts, as was plotted in Figure 3.8. The thin film region mass transfer coefficient is approximately 10 to 20 times lower than the dispersed region coefficient, as was also seen by Meeuwse et al. [106]. For future work, a more in detailed study can be performed by two phase hydrodynamic studies on the laminar and turbulent flow behaviours.
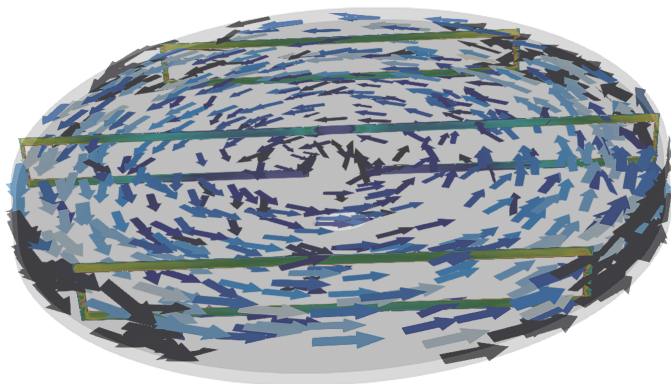
3

CHAPTER 4

LARGE EDDY SIMULATION OF THE ROTOR-STATOR SPINNING DISC REACTOR

4

Abstract

In this work, Computational Fluid Dynamics (CFD) are used to study the hydrodynamics in a complete rotor-stator spinning disc reactor (rs-SDR) with throughflow. Large Eddy Simulations (LES) of OpenFOAM 9 were used to capture the turbulent structures of the flow in combination with the wall-adapting local eddy viscosity sub-grid-scale model (WALE). The method was validated based on residence time distributions (RTD) for a range of rotational Reynolds numbers (Re = $\omega R_D^2 \nu^{-1}$ = 3.2 - 52 ·10^4), a dimensionless flowrate (C_w = $Q\nu^{-1}R_D^{-1}$) of 150 and G = 0.0303 (G = hR_D^{-1}). The experimental RTD were obtained from tracer experiments with UV/VIS flow cells. From the RTD, the plug flow (PFR) volume fraction, the Péclet number and the radial position (r_{trans}) where the flow changes from PFR into ideally mixed (CSTR) were determined by using an engineering model based on axial dispersion. For the turbulent cases, good agreement based on the RTD curve, PFR volume, Péclet number and r_{trans} were found. Furthermore, the boundary layer thickness on the rotor and stator and the entrainment coefficient were in good agreement with literature. Lastly, the turbulent intensity was analyzed illustrating a high intensity at the rim of the rotor and was 10% larger in centripetal flow compared to centrifugal flow.

4.1. INTRODUCTION

The hydrodynamic behavior in rotor-stator systems [121] has been researched extensively for a variety of applications such as hard disk drivers, centrifugal pumps [122, 123], high shear mixers [124] and reactor configurations [125]. Detailed measurements on the hydrodynamics in rotor-stator cavities have been performed by Daily and Nece [37] who observed four different flow regimes based on two parameters: the rotational Reynolds number ($Re = \omega R_D^2 \nu^{-1}$), based on the rotor radius (R_D) and the rotational rate (ω), and the rotor-stator gap ratio ($G = h R_D^{-1}$) with h the rotor-stator spacing. The four regimes are listed below.

- Regime I: laminar flow with merged boundaries

- Regime II: laminar flow with separated boundaries

- Regime III: turbulent flow with merged boundaries

- Regime IV: turbulent flow with separated boundaries

For high rotational Reynolds numbers, two turbulent boundary layers are formed, namely a Von Kármán boundary layer at the rotor, and a Bödewadt boundary layer at the stator [35, 36]. These boundary layers can be either separated or merged. This depends on the rotational Reynolds number and the gap ratio. Launder et al. [38] distinguished four hydrodynamic regimes based on Re and G in the flow map in Figure 4.1. When the Von Kármán and Bödewadt layers are separated by an inviscid core, this is often referred to as Batchelor flow [126]. When the inviscid core is not present, and the Von Kármán and Bödewadt layers are merged, the flow behaviour is commonly referred to as torsional Couette flow [40].

Describing the flow patterns in this rotor stator cavity has proven challenging despite work by multiple researchers on this topic [33, 37, 39, 127]. Their experimental and theoretical research provided knowledge about the hydrodynamics of the rotor stator cavity and this knowledge was later on used for computational fluid dynamics (CFD) studies; introducing a different method for studying the hydrodynamics in rotor stator systems [34, 38–42]. Various authors successfully described the flow in a rotor stator cavity by using CFD. Simulations were performed mostly with the Reynolds Stress Model (RSM) [39–41] and Large Eddy Simulations (LES) [42]. Their investigations were focused on: the validation of the axial velocity profiles and Reynolds stresses by using a laser-Doppler anemometer [34, 39], the effects of throughflow on the hydrodynamics, investigated by varying the
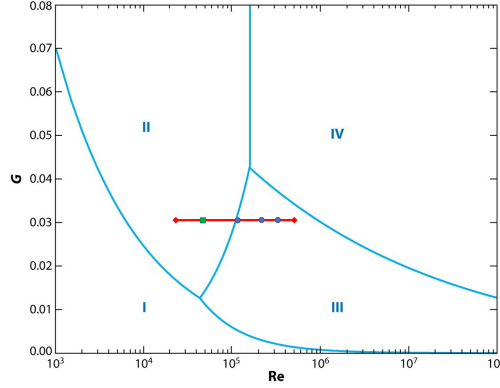
Figure 4.1: The flow regimes in the rotor-stator cavities according to Daily and Nece and Launder et al. [37, 38]. The red line indicates the experimental range. The green square is the laminar simulation and the blue dots are the turbulent simulation cases from this study. The simulation cases correspond with ω equal to 10, 25, 50 and 75 rad/s.

dimensionless flow rate ($C_w = Qv^{-1}R_D^{-1}$, with $C_w < 0$ as centripetal flow and $0 \geq C_w$ as centrifugal flow) [34, 40, 41], the Reynolds numbers and G. Another fundamental study was performed by Van Eeten et al. for describing the boundary layer thickness in a rotor-stator cavity [44, 45]. This study contains a numerical solution with the use of no-slip boundary conditions and a power series solution of the boundary layer thickness. Van Eeten et al. derived with these techniques a direct relationship between the Reynolds number ($Re_h = \omega h^2 v^{-1}$) and the thickness of the Von Kármán ($\delta_K \propto Re_h^{-1/2}$) and Bödewadt ($\delta_B \propto Re_h^{-1/2}$) layer. This relationship was however, only derived for the situation of $C_w = 0$. Recently, Bailey et al. successfully presented a fully predictive mathematical model to predict the swirl ratio (dimensionless local tangential velocity), pressure and torque in an enclosed rotor-stator cavity [46]. They tested the model for G = 0.05 to 0.5 and found that the swirl ratio decreased and torque increased at higher radial positions. Another recent study on rotor-stator systems was performed by Jiao et al., they investigated an enclosed rotor-stator annulus with LES and the dynamic Smagorinsky model [43]. This study reported that the instability in the Bödewadt layer was delayed and in the Ekman layer promoted at G = 0.027.

The rotor-stator application used during this research is the rotor-stator spinning disc reactor (rs-SDR) [14], with Figure 4.2 providing a schematic representation of this device. The rs-SDR consist of a rotating disc (rotor) surrounded by a stagnant casing (stator) with a spacing of only a few millimeters resulting in two coupled rotor-stator cavities. The small
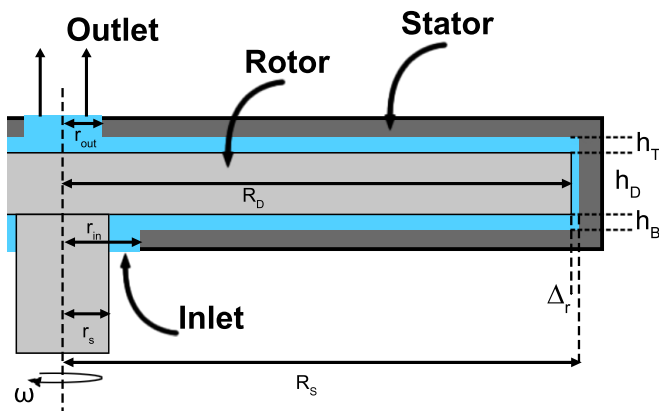
Figure 4.2: A schematic representation of the rotor-stator spinning disc reactor with, R_s the radius of the stator, R_D the radius of the rotor, r_s the radius of the shaft. The axial clearances are denoted as h_T and h_B, the thickness of the disc as h_D and the radial clearance by Δ_r. The inlet and outlet radii are shown as r_{in} and r_{out} respectively.

spacing, combined with the high rotational rates often used in the reactor, leads to very high shear forces in the rotor-stator gap. These shear forces invoke high levels of turbulence, and intensifies the heat and mass transfer rates [14, 15, 25, 26]. In multiphase flows for instance, the shear forces results in small bubbles/droplets and a high specific interfacial area [18, 106, 107]. In general the rs-SDR has great potential for gas-liquid [16, 31, 108], liquid-liquid [18–22, 30] and liquid-solid [22–24] systems. However, the performance of the rs-SDR tends to be difficult to predict due to the wide scale of turbulent eddies at which kinetic energy is distributed in turbulent flows [13]. Therefore, macroscopic flow behavior is especially important to characterize, as it largely determines the performance of the rs-SDR allowing this device to be used further to intensify chemical processes [128]. Such studies will help to improve the utilization of feedstocks and use energy more effectively [3], contributing to a more sustainable industry.

On a macroscopic level, the flow behaviour in the rs-SDR with a positive net throughflow ($C_w > 0$) is divided into two parts. At the lower radial positions (close to the inlet and outlet), a throughflow governed regime exists which behaves as plug flow (PFR). At higher radial positions (close to the rim of the disc) the hydrodynamic behaviour is rotation governed and can be assumed as ideally mixed (CSTR). In Figure 4.3, a schematic representation of the transition between PFR and CSTR is

depicted, note that Figure 4.3 holds for the torsional Couette case only. The transition point between the two varying regimes is referred to as the transition radius (r_{trans}) [32, 34], see Equation 4.1. Equation 4.1 also contains a proportionality constant c and it was found to be 0.219 based on previous work [32, 33]. This proportionality constant was confirmed by CFD simulations with the RSM [39, 40]. According to Owen et al., this value for c suggests that the transition occurs when the superimposed flow rate equals the entrainment rate of a turbulent free rotating disc system [33].

$$\frac{r_{trans}}{R_D} = \left(\frac{1}{c} \frac{C_w}{Re^{4/5}} \right)^{\frac{5}{13}}$$
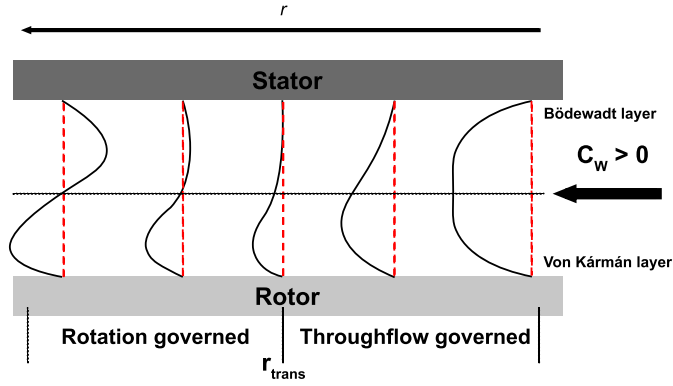
(4.1)

Figure 4.3: Flow development from throughflow dominated (PFR region) into rotational dominated (CSTR region) regimes for the torsional Couette case, with r_{trans} being the transition radius. Also, the Von Kármán and the Bödewadt layers are depicted.

While researchers have extensively studied a single rotor stator cavity by using RSM, LES or analytical approximations, this study aims to simulate the complete rs-SDR with throughflow, connecting the top (centripetal flow) and bottom (centrifugal flow) rotor-stator cavity of the rs-SDR, with CFD by making use of LES in OpenFOAM 9. The operation range is at G = 0.0303 and varying from $Re = 3.2 - 52 \cdot 10^4$ (red line in Figure 4.1). Within this range, transition from regime II to III takes place and the flow behaviour will shift from a laminar flow with separated boundaries into a turbulent flow with merged boundaries. The macromixing properties are validated by comparison of experimental residence time distributions (RTD) experiments along the red line in Figure 4.1 with the simulated results (blue dots and green square in Figure 4.1). Verifications based on the thickness of the Von Kármán and Bödewadt layers are also made

in combination with an analysis on the transition radius. Lastly, general analysis based on the turbulence and velocity profiles in the rs-SDR will be provided to gain more insight about the hydrodynamic behaviour.

4.2. Experimental Method

4.2.1. Experimental setup

To validate the rs-SDR simulation results, the macromixing behaviour in the rs-SDR was studied with tracer experiments. The rs-SDR used for the experiments (see Figure 4.2) consists of a transparent poly methyl methacrylate rotor and stator with a radius of respectively R_D = 0.066 m, R_S = 0.067 m and a axial distance between rotor and stator of $h_T = h_B = 2.0 \cdot 10^{-3}$ m, resulting in a radial clearance (Δ_r) of $1.0 \cdot 10^{-3}$ m and a G of 0.0303. A stainless steel shaft is mounted at the bottom of the disc and rotates with rotational rate (ω) up to 157 rad/s. The liquid enters the reactor via an annulus of thickness equal to $4.0 \cdot 10^{-3}$ m (r_{in} = 0.010 m and $r_s = 6.0 \cdot 10^{-3}$ m) between the shaft and the stator, and leaves the rs-SDR through the middle of the top stator, in an annulus with a radius of $5.0 \cdot 10^{-3}$ m (r_{out}). This results in a total volume of $59.6 \cdot 10^{-6}$ m^3. The experiments were conducted in the set up as depicted in Figure 4.4. Demineralized water was pumped through the reactor via a VerderGear VG1000 gear pump with a volumetric flow rate Q of $9.85 \cdot 10^{-6}$ m^3 s^{-1}. At a distance of 0.13 m from the inlet (0.05 m of tubing and an internal channel inside the stator of 0.08 m) and 0.05 m from the outlet, UV/VIS flow cells (Avantes) were used to measure the absorption (1/4 inch). The flow cells were connected to a AvaLight-DHS lightsource with a wavelength ranging from 191 nm to 750 nm and a AvaSpec-DUAL spectrometer. Avasoft 8 was used as the software to log the measured counts from the spectrometer with an integration time of 1.1 ms. The tracer was injected by using a KD Scientific syringe pump into the feed stream via a T-junction placed 0.03 m before the inlet flow cell. A flow rate, Q_t, of $1.39 \cdot 10^{-7}$ m^3 s^{-1} was used with an aqueous methylene blue solution ($4.69 \cdot 10^{-2}$ M) as the tracer. All experiments were performed three times and the outlet signal was observed for at least 10 times the residence time ($\tau = V_R/Q$). The rotational Reynolds number was varied from $3.2 \cdot 10^4$ to $5.2 \cdot 10^5$ and C_ω was fixed at 150 for all experiments.

When the tracer passes through the flow cell, the light will partially be absorbed and result in a lower intensity which is measured by the spectrometer. The number of counts is measured at a wavelength of 613 nm. By using Equation 4.2, the counts were converted into an

absorbance, with N the number of measured counts, N_0 referring to the dark measurement and N_{ref} to the reference of demineralized water.
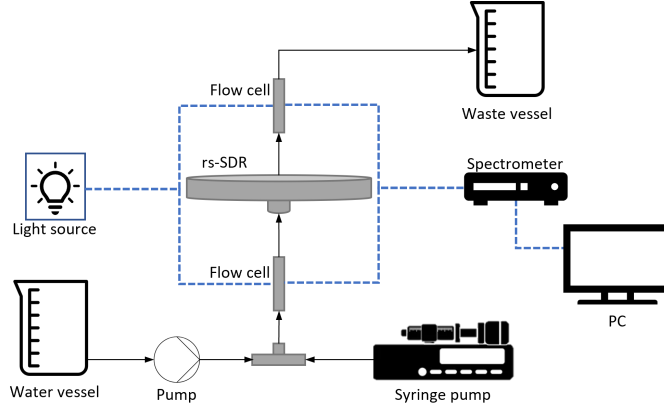

Figure 4.4: A schematic representation of the setup used for the macro mixing characterisation of the rs-SDR.

$$A = -\frac{log(N - N_0)}{log(N_{ref} - N_0)} \tag{4.2}$$

Together with the Beer-Lambert's law and a calibration curve, the absorbance was converted into a tracer molarity. The concentration was logged over time and converted into the E-curve, see Equation 4.3, with C(t) being the concentration at time t. The integral in the denominator was determined by using the trapezoidal method.

$$E_{RTD}(t) = \frac{C(t)}{\int_0^\infty C(t)dt} \tag{4.3}$$

The distribution of the obtained concentration curve is called the residence time distribution (RTD) and it is a probability distribution function which describes the time spent by a single particle (or tracer molecule) in a reactor [129]. This method is used to describe the ideality of a reactor, either as plug flow (PFR), ideally mixed (CSTR) or a combination of both.

To take into account the relatively long injection time with respect to the residence time, a time domain deconvolution was used to increase accuracy and reduce the signal noise [130, 131]. For this, the outlet signal, Y_{UV}(t), was described as a convolution between the inlet signal, X_{UV}(t) and the reactor model E_{RTD}(t), as described in Equation 4.4. For the rs-SDR

a reactor model has already been described extensively and is shown in Equation 4.5 [27, 28]. Here, the τ_{PFR} represents the residence time of the plug flow volume, τ the mean residence time and n the number of tanks in series. By using nonlinear least-squares optimization, the model parameters were fitted. With this method, R^2 values $\geq$ 0.99 were obtained. An example result from an experiment at Re = $2.4 \cdot 10^5$ and C_w = 150 is shown in Figure 4.5. For the analyses, PFR behaviour was assumed for the distance between the tracer injection and the inlet of the reactor and was subtracted from the modelled PFR volume.

$$Y_{UV}(t) = \int_0^t E_{RTD}(t) X_{UV}(t - \tau) dt \qquad (4.4)$$

$$E_{RTD}(t) = \begin{cases} 0 & \tau < \tau_{PFR} \\ \dfrac{t^{n-1}}{(n-1)!(\frac{\tau - \tau_{PFR}}{n})^n} e^{-t/(\frac{\tau - \tau_{PFR}}{n})} & \tau \geq \tau_{PFR} \end{cases} \qquad (4.5)$$
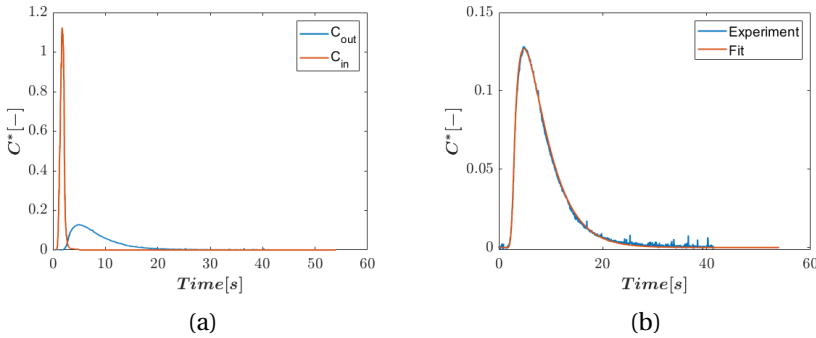

Figure 4.5: (a) Normalised inlet and outlet concentrations of a typical tracer experiment at Re = $2.4 \cdot 10^5$ and C_w = 150. (b) Normalised outlet concentration compared with a typical fitted outlet concentration by means of a deconvolution approach at Re = $2.4 \cdot 10^5$ and C_w = 150.

4.3. Numerical Modeling

The computational fluid dynamics simulation of flow in the rotor-stator spinning disc reactor were performed in OpenFOAM 9 [132]. OpenFOAM is an acronym for Open Source Field Operation and Manipulation, which is an open source code that solves the Navier-Stokes equations numerically and is generally used to perform CFD simulations.

4.3.1. LARGE EDDY SIMULATION

The turbulence was modeled using Large Eddy Simulation (LES) [133]. The underlying principle of Large Eddy Simulation is spatially averaging the Navier-Stokes equations using a filtering function. Using this approach, the Navier-Stokes equations can be solved up to a certain spatial resolution for the filtered velocity and pressure. An important parameter in LES simulation is the filter size. The filter size should be selected such that largest eddies are resolved. Resolving these are important as the large eddies contribute the most to the total turbulent kinetic energy [50]. On the other hand, the small-scale structures are not resolved and their effect on the mean flow is modeled. Hence, the computational costs are lower compared to direct numerical simulations (DNS), while the turbulent nature is modeled more accurately than in Reynolds Averaged Navier-Stokes (RANS) simulations. Since turbulent energy is dissipated from the large eddies towards the smaller eddies via the energy cascade, the approach of modeling the smaller eddies with closure models is justified. However, it should be noted that the influence of the small-scale eddies on the large-scale eddies is not accounted for correctly in LES. Therefore, uncertainty contained in the small-scale eddies can propagate to the large-scale eddies, leading to a mathematical ill-posed problem [54]. Even though this uncertainty in the small-scale eddies might lead to inaccurate flow behavior, the overall statistical properties resemble the modeled case in many cases [50].

4.3.2. NUMERICAL METHOD

The complete geometry was equal to the experimental rs-SDR and first the internal field based on the stator was constructed with the *blockMesh* utility from OpenFOAM and consists of $4.2 \cdot 10^6$ grid cells (150 x 200 x 140; r, θ, z). In order capture the wall effects, refinement was included such that grid cell sizes near the walls were decreased. The disc from the experimental setup was recreated using a CAD drawing with SolidWorks and was subtracted from the total mesh created with the *snappyHexMesh* utility. This resulted in a mesh consisting of $1.5 \cdot 10^6$ cells with a maximum non-orthogonality of 0.14°. The complete rs-SDR case was solved using OpenFOAMs standard solvers. Using a grid dependency study, an adequate resolution was determined. It was verified there is no effect of the grid size on the accuracy when a mesh was used with twice the number of grid cells. Also, according to Pope, a good method to evaluate whether the grid size is suitable for LES, is to determine the amount of resolved turbulent kinetic energy (TKE) [134]. When the resolved TKE is above 70%, the grid

size is said to be sufficiently accurate to properly perform LES. According to our analysis, the averaged resolved TKE is 96.4%. A more detailed description of this analysis can be found in the Supporting Information D.2. When comparing the average grid size with the Kolmogorov length scale (Equation 4.6, with ϵ being the energy dissipation rate (EDR)), the averaged deviation from the Kolmogorov length is 10% (1 - η $\Delta_{r,\theta,z}^{-1}$) [11]. This means that the grid size is close to the DNS length scale.

$$\eta = \left(\frac{\nu^3}{\epsilon}\right)^{1/4} \tag{4.6}$$

Mathematical term	Interpolation scheme
Gradient	Gauss cubic
Divergence	Gauss cubic
Laplacian	Gauss cubic corrected
Interpolation	Cubic
Surface-normal gradient	Cubic corrected

Table 4.1: Interpolation schemes which were used in the rotor-stator spinning disc reactor simulations.

In order to reduce numerical diffusion and to capture the turbulence more accurately, higher-order cubic interpolation schemes were employed. These interpolation schemes are displayed in Table 4.1. Along with the numerical schemes, solvers have to be selected to solve the discretised system of algebraic equations. For the pressure field, the *GAMG* (Geometric agglomerated Algebraic MultiGrid) solver was selected and for the additional fields, the solver *smoothSolver* was used. In such algorithms, preconditioners and smoothers should be used to enhance the rate of convergence by smoothening the residuals. For *GAMG*, *GaussSeidel* and *FDIC* were selected to be the smoother and preconditioner, respectively. The tolerances for the residuals were not changed from OpenFOAM's original values: pressure is $1 \cdot 10^{-6}$ and is $1 \cdot 10^{-5}$ for the additional quantities [132].

The wall-adapting local eddy viscosity (WALE) turbulence LES model was selected [135]. The main benefit of the use of WALE is that the rotational aspects of the turbulent flow are captured adequately with the WALE turbulence model [135], which is essential for rotor-stator flows. The cutoff width was selected to be the cube root of the grid cell volume, since it is a good representation for hexahedral meshes [132].

The flow solver *pimpleFoam* was used on 256 cores on the Dutch supercomputer Snellius. The PIMPLE algorithm is a combination of an Semi-Implicit Method for Pressure Linked Equations (SIMPLE) and the Pressure Implicit Splitting Operator (PISO). It solves first the velocity equations by using the fields from the previous time step and is generally known as the momentum predictor. The velocity and pressure are corrected several times to satisfy mass conservation [136, 137]. The PIMPLE algorithm in this study contains one inner corrector as well as five outer correctors selected for the evaluation of the turbulence model. The mesh was decomposed using the Scotch method. Adaptive time-stepping was implemented to ensure a stable simulation with a Courant Friedrichs Lewy number (CFL) of 0.2. A steady state was confirmed when the temporal gradient of the relative difference of the average velocity field starts to oscillate around 0. For all simulations, a steady state was reached after approximately half a residence time. These runs took about $5 \cdot 10^5$ time steps of $\sim 5 \cdot 10^{-6}$ seconds.

After a steady-state velocity field was obtained, the residence time distribution was estimated based on the convection and diffusion of a passive scalar (f) in a velocity field according to Equation 4.7. In this simulation, the velocity field and the turbulent diffusion coefficient (D_t) were obtained from the simulated velocity field and local turbulent viscosity (ν_t), using a turbulent Schmidt number (Sc$_t$ of 0.9) [138]. For the molecular diffusion coefficient (D_m) of the passive scalar, it was assumed that the mixture behaves like water (aqueous solution) and therefore a value of $1 \cdot 10^{-9}$ m^2 s^{-1} was used. At the outlet, the mixing cup concentration is computed in each time step. Since the inlet concentration of the passive scalar is set to unity as a step input, the time derivative of the mixing cup outlet concentration represents the residence time distribution function [129].

$$\frac{\partial f}{\partial t} + \nabla \cdot f \boldsymbol{u} = \nabla \cdot (D_m + D_t) \nabla f \qquad (4.7)$$

4.3.3. INITIAL AND BOUNDARY CONDITIONS
The velocity field was initialised on basis of the inlet flow rate and the rotational rate of the disc. The tangential velocity field was initialised using a core velocity of 40% of the local rotor velocity. This value was based on previous research of similar systems with throughflow where an entrainment coefficient K is introduced (ratio between tangential velocity in the core of the fluid and the disc velocity at the same radius), see

Equation 4.8 and 4.9 with r being the radial position in the system. [39, 41]. For similar systems without throughflow, the core velocity was 31.3% of the local rotor velocity [44, 119].

$$C_{q_r} = \frac{Q(\omega r^2/v)^{1/5}}{2\pi\omega r^3} \tag{4.8}$$

$$K = 2(-5.9C_{q_r} + 0.63)^{5/7} - 1 \tag{4.9}$$

On the basis of continuity, the radial velocity was computed at each radial position. Thereafter, the radial and tangential velocity were decomposed into Cartesian coordinates to enable implementation in OpenFOAM. The pressure field was initialised to be uniform at the reference pressure and the turbulent viscosity was uniformly initialised using the kinematic viscosity. The velocity on the stator walls was set to zero by applying a no-slip boundary condition and a zero-gradient boundary condition for the pressure. The *rotatingWallVelocity* was imposed to the rotor and the shaft to describe the no-slip boundary condition for a rotating patch. For the turbulent viscosity, *nutUSpaldingWallFunction* was applied at all walls, to lessen the importance of the constraints on y^+ and r^+, especially. At the inlet, a fixed boundary condition was forced for the velocity, which ensures a constant inlet flow rate of $1.0 \cdot 10^{-5}$ m^3 s^{-1}. The pressure boundary condition was zero-gradient at this location. At the outlet, the pressure was fixed at the reference pressure (1 atm) and the velocity was modeled using an *inletOutlet* boundary condition. This boundary condition computes the velocity using a zero-gradient boundary condition, but sets the velocity to zero in case of an inward velocity. For the turbulent viscosity, OpenFOAMs *calculated* boundary condition was used.

4.4. VALIDATION

Validation of CFD studies is vital to critically assess the quality of simulation results. During this study, two experimental validation strategies were employed. For this, experimentally obtained transition radii and residence time distributions were used. The entrainment coefficient is used as an additional validation and can be found in Supporting Information C.4.

4.4.1. RESIDENCE TIME DISTRIBUTION

In literature a reactor model is proposed for the rs-SDR, see Equation 4.5. This model assumes a combination of an ideal PFR followed by *n* ideally stirred tanks in series (De Beers model) [27]. One disadvantage of this

approach is the non-differentiable outlet concentration, since in reality a less abrupt change in hydrodynamic behaviour is expected. Therefore, a new approach is introduced for the determination of the macromixing behaviour. The proposed model uses a non-ideal PFR and one CSTR in series. The nonideality of the PFR takes axial dispersion into account and will be referred to as the dispersion model from this point on. The dispersion will give a more physical representation of the turbulence and remove the dependency on the amount of tanks in series needed to describe the rs-SDR, which is typically a number between 1 and 3 [27, 139] where only an integer value would have physical meaning.

The derivation of the dispersion model is represented by the intermediate steps for the non-ideal PFR and are given in Equations 4.10-4.12 [129].

$$\frac{\partial C}{\partial t} + u\frac{\partial C}{\partial z} = D_{ax}\frac{\partial^2 C}{\partial z^2} \tag{4.10}$$

$$\Theta = \frac{tu}{L} = \frac{t}{\tau_{PFR}} \qquad Z = \frac{z}{L} \qquad Pe = \frac{uL}{D_{ax}} \tag{4.11}$$

$$\frac{\partial C}{\partial \Theta} + \frac{\partial C}{\partial Z} = \frac{1}{Pe}\frac{\partial^2 C}{\partial Z^2} \tag{4.12}$$

By assuming that the impulse of the tracer takes place at $z = 0$ and $t = 0$ and that there is no variation in the dispersion coefficient (D_{ax}) for all values of Z, the dispersion model will result in the concentration at the outlet, c_{out}, in Equation 4.13. Where τ_{PFR} and Pe represent the PFR residence time and the Péclet number respectively. This outlet concentration was numerically used as inlet condition for the CSTR for the overall description of the rs-SDR reactor model.

$$C_{out}(t) = \left(Pe\frac{\tau_{PFR}}{4\pi t}\right)^{0.5}\exp\left(-Pe\frac{(1 - t/\tau_{PFR})^2}{4t/\tau_{PFR}}\right) \tag{4.13}$$

An example of the goodness of fit obtained for the dispersion model is shown in Figure 4.6 along with the experimentally obtained concentration profile and the ideal PFR with n tanks in series model. The R^2 values for the dispersion model is for all cases above 0.99, which is also the case for De Beer's model [27]. Based on the high R^2 the new model was found adequate to be the RTD model for this paper. A more detailed comparison between the two models can be found in the Supporting Information C.2.

The RTD curves were also determined for the simulations and can be compared with the experimental averages of three experiments, Figure
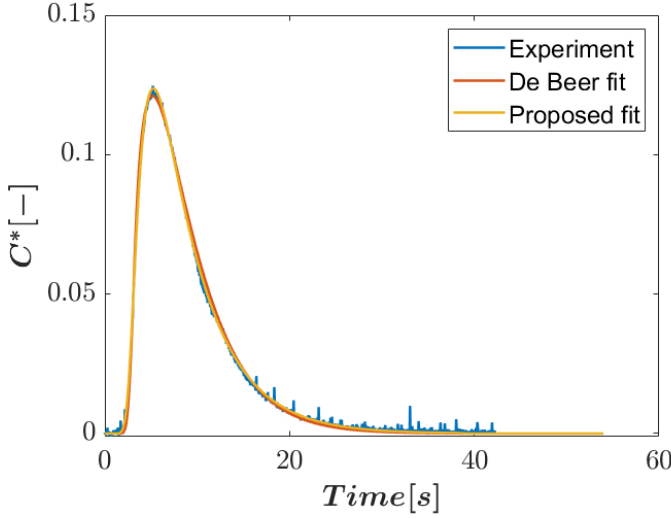
Figure 4.6: Normalised outlet concentration compared with a the fitted outlet from De Beers model [27] and the dispersion model [129] concentration by means of a deconvolution approach at Re = $2.4 \cdot 10^5$ and C_w = 150.

4.7. Within this figure the graphs are shown for the tested rotational rates, (10, 25, 50 and 75 rad/s). From Figure 4.7, it can be concluded that the laminar case does not match, the transition case has a slight mismatch and the two turbulent simulations are in agreement with the obtained experimental results. This mismatch with experiments for both the dispersion model and the simulation is probably due to the system being laminar. In the simulations the LES induces unwanted turbulence on the flow field and as a result, the diffusivity is overestimated, the RTD graph for the experiment suggests a significant shortcut in the flow pattern, this is described in more detail by Supporting Information C.3. On the other hand, the dispersion model and simulation are in better agreement with the experimental results for the 25 rad/s situation (Figure 4.7b). This is despite the rotational Reynolds being in transition between the laminar and turbulent regime. Of course, the transition between the two regimes is never a hard transition, but rather a transition range, and within Supporting Information C.6 it can also be seen that there is still an inviscid core present (Batchelor flow) [126]. Consequently, this results also in a system which would induce unwanted turbulence. However, this case is much closer to the experimental results, since turbulent structures are already developed in this case. The simulations in the fully turbulent
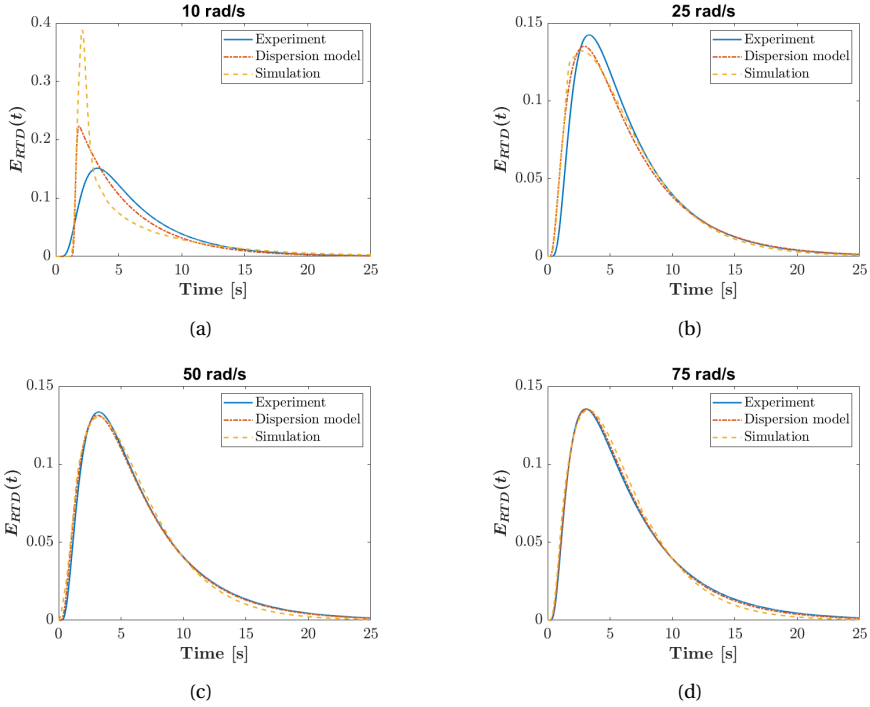
Figure 4.7: A comparison between the experimentally obtained E-curve, the curve from the dispersion model (Equation 4.13) and the simulated results obtained from OpenFOAM are plotted for, (a) 10 rad/s, (b) 25 rad/s, (c) 50 rad/s and (d) 75 rad/s.

regime, Figures 4.7c and 4.7d, show an almost perfect agreement with the experimental and dispersion model results. Therefore, it is concluded that the simulations match in the turbulent flow conditions, while larger deviations are obtained in more laminar cases.

To validate the LES simulation, there can be a quantitative comparison of the experimentally obtained PFR volume present in the rs-SDR, the Péclet number and the transition radius between throughflow and rotational governed flow. In Figure 4.8, a comparison is made between the simulated results (asterisks) and the experimental results fitted by the dispersion model (error bars). The dashed line represents the transition point between laminar and turbulent flow. Based upon the results from Figure 4.7 and Supporting Information C.3, it seemed prudent to only include the 50 and 75 rad/s simulations in the comparison. Figure 4.8a shows the PFR volume fraction as function of the Reynolds number. According to the dispersion model, the PFR zone should increase with decreasing Reynolds numbers. From $Re = 0.8 - 1.0 \cdot 10^5$ the flow will enter

the turbulent regime (see Figure 4.1) and a linear decrease in the PFR volume fraction is observed. This is a logical observation since the increase in turbulence results in a stronger radial outflow/inflow in the Von Kármán and Bödewadt layers respectively, as also observed in literature [27, 139]. In the same graphs the LES results are also plotted, and these results are within the experimental error and the relative deviation from the mean experimental point is 6.5 and 5.4% for 50 and 75 rad/s respectively. It can be concluded that the simulations describe the PFR zone well. However, the Péclet numbers (Figure 4.8b) are slightly underestimated by the LES simulations, relative deviation from the mean is 23.3 and 16.2% for 50 and 75 rad/s respectively. This could be related to the additional numerical diffusion ($\sim 10^{-9}$ m^2/s) that is imposed by the simulations, especially with the turbulent diffusion being $\sim 10^{-8}$ m^2/s.
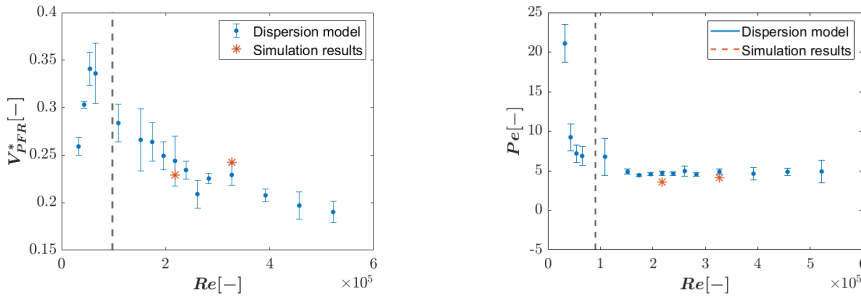

Figure 4.8: (a) The results of the PFR volume fraction for LES and the dispersion model as function of Reynolds are shown and (b) shows the Péclet number as function of Reynolds. The dashed line is the transition point from laminar into turbulent flow.

4.4.2. TRANSITION RADIUS

Another important aspect to investigate is the transition radius. As was mentioned previously, the transition radius (r_{trans}) is the boundary between throughflow and rotational governed flow, closely related to the boundary between PFR and CSTR behaviour. In Figure 4.9 the development of the different flows for two of the simulated rotational rates is visualized. The graphs show the dimensionless radial velocity in between the rotor ($Z = 0$) and the stator ($Z = 1$) at 0.15, 0.53 and 0.91 times R_D. In laminar flow (Figure 4.9a) there is almost no radial inward flow, which is indicative for a lack of CSTR behaviour. Hence, the majority of the flow field behaves as PFR and the rotational rate is not high enough to impose dominant CSTR flow behaviour. For a velocity of 75 rad/s, a more clear distinction is visible between the radial positions, hence two flow regimes exists inside
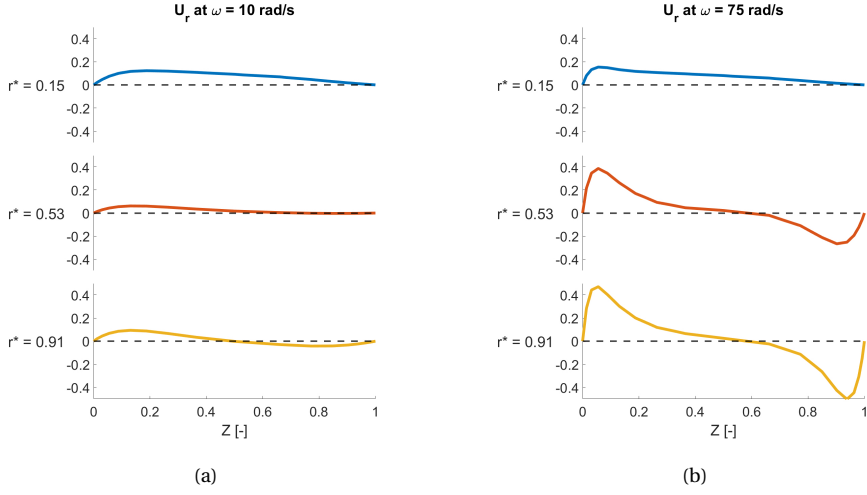
the rs-SDR.

Figure 4.9: Mean radial velocity profiles for three different radial positions ($r^* = r/R_D$) between the rotor ($Z = 0$) and the stator ($Z = 1$) with $Z = z/h_T$. The subplots denote two different simulation cases, laminar flow and the most turbulent case to highlight the differences the most. (a) 10 rad/s and (b) 75 rad/s.
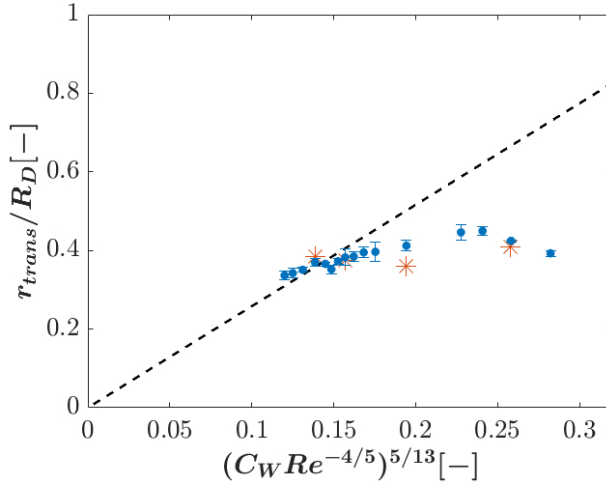

Figure 4.10: The transition radius prediction in the black dashed line plotted against the computationally and experimentally determined r_{trans} by using Equation 4.1.

The radial position where the transition will take place can be estimated from the PFR volume using Equation 4.14 [27]. This equation is based on

the assumption that there will be no axial and tangential velocity gradients. This assumption is justified by the flow being turbulent (for most cases). The next assumption is based on the similarity of both the centrifugal and centripetal flow and therefore it is possible to assume that r_{trans} is equal in both rotor stator cavities [40]. Also, the extra volume added by external and internal tubing towards and after the rotor stator cavities (V_{extra}) is removed from the total PFR volume, since it is assumed to behave as PFR and does not contribute to the rs-SDR PFR volume. Note that this only holds for the experimentally determined r_{trans}, since LES simulations only include the interior of the rs-SDR and not the inlet and outlet tubing.

$$\frac{r_{trans}}{R_D} = \sqrt{\frac{V_{PFR} - V_{extra}}{2\pi R_D^2 h} + \left(\frac{r_s}{R_D}\right)^2} \tag{4.14}$$

In Figure 4.10, the results from the experiments and LES simulations are plotted as function of Equation 4.1 (y-axis). As mentioned previously, Equation 4.1 contains a proportionality constant and was found to be 0.219, but De Beer et al. showed that this value strongly depends on the gap ratio G [27]. The black dashed line in the graph represents the fit for the experimental data (blue error bars) in the turbulent torsional Couette regime and results in a proportionality factor of $c = 0.08$. Figure 4.10 also shows that with the transition from turbulent Couette into laminar Batchelor, the experiments do not follow the prediction by Equation 4.1 anymore. This is likely due to the dominance of the throughflow region and the absence of r_{trans}. The figure also shows the results from LES simulations (orange asterisks) and it can be seen that the turbulent cases (50 and 75 rad/s) fall within the experimental error and the relative deviation from the experimental mean is 1.8 (50 rad/s) and 4.2% (75 rad/s). Additionally, the case in the transition regime (25 rad/s) does not fall within the experimental error and also deviates 14.9% from the experimental mean. The laminar case (10 rad/s) is slightly off the experimental mean (3.9% relative) and falls just outside the experimental error by 1.1%.

4.5. FLOW CHARACTERISATION

From the Validation (section 4.4) it can be concluded that the simulation is able to predict the experimental results. This section will discuss the behaviour inside the rs-SDR based on the LES simulation results and contains information about the mean flow fields, boundary layer thickness and turbulent characteristics. The results from the Validation (section 4.4) illustrated that the 10 and 25 rad/s simulations are not validated, but

their flow characterizations are shown in Supporting Information C.6 as complementary information.

4.5.1. MEAN FIELDS

Previous studies only investigated a rotor stator configuration with a single cavity (only the top side of the disc) [33, 38, 39, 41, 127]. From our simulations it is possible to describe the characteristics for a complete rs-SDR. In Figure 4.11, the tangential velocity is shown at different radial positions and for the two rotor-stator cavities. The velocity profiles for the top rotor stator cavity are represented in Figure 4.11a. The graphs show a clear throughflow governed velocity profile in the vicinity of the outlet ($0.01R_D$). This behaviour is due to the throughflow dominated regime ($R_D < r_{trans}$) and seems to decrease with increasing rotational rates, because of the increase in CSTR volume (torsional Couette flow). Furthermore, there are small differences between the profiles of $0.4R_D$ and $0.99R_D$ and that is due to the radial position being larger than r_{trans} (see Figure 4.14). This means that the flow is rotation governed and almost no effect of superimposed throughflow is present. Another observation is the difference between the top and bottom cavity profiles, Figure 4.11a and b respectively. It seems that the bottom cavity forms a Stewartson-like profile at higher rotational rates. In this case the bulk of the fluid is at rest and only a Von Kármán layer is formed [36].

The local flows have been identified and the higher turbulent flows have proven to be in agreement with literature, but the overall flow patterns are yet to be analysed. In Figure 4.12 a slice ranging from $0.6R_D$ to R_S of the rs-SDR is represented. The slice depicts the instantaneous velocity streamlines (created in ParaView) after 0.5τ. The streamlines in the centrifugal flow regime show the increase in CSTR behaviour with increasing radial position, as the flow shows more local recirculation. This is also depicted in Figure 4.12, where the eddies start to form at the lower radial positions and become fully developed at the higher radial positions. This indicates a more ideally mixed system, hence more CSTR behaviour. Also, the statement made about the r_{trans} being different for the centripetal and centrifugal flow regimes is supported by comparing the size and number of vortices for both cavities. This clearly shows the centripetal flow as being more turbulent and hence a having larger CSTR volume. Another interesting observation is the amount of eddies present at the rim of the rotor, indicating that the turbulent intensity is the highest in this region, likely due to a smaller rotor stator distance ($1 \cdot 10^{-3}$ m) in combination with the high local rotor velocity (ωr).

Top cavity

(a) Top Cavity, rotor at $Z = 0$ and stator at $Z = 1$

Bottom cavity

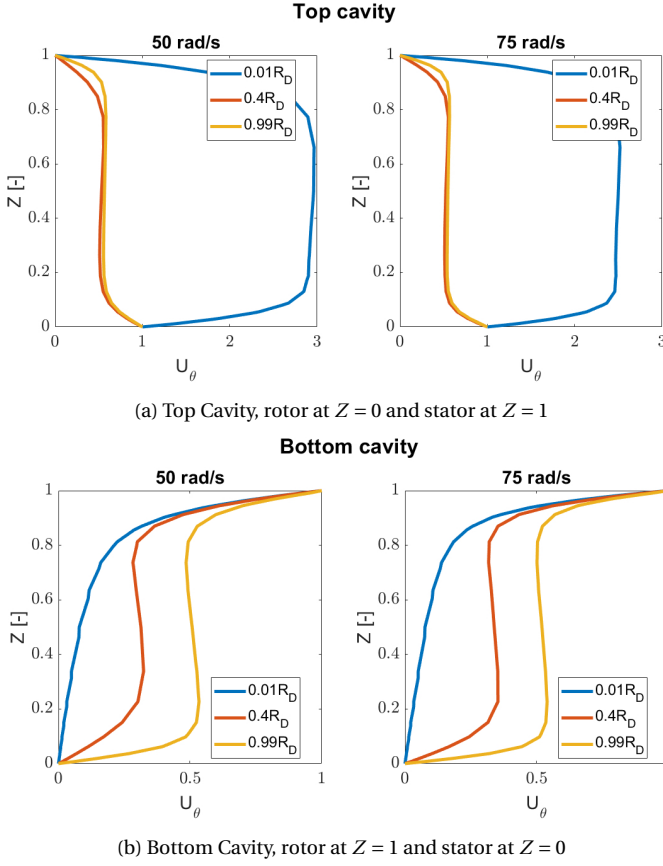(b) Bottom Cavity, rotor at $Z = 1$ and stator at $Z = 0$

Figure 4.11: Shows the velocity profiles of 50 and 75 rad/s at three different radial positions, with the rotor at $Z = 0$ and the stator at $Z = 1$, for figure (a). Note that for (b), the rotor ($Z = 1$) and the stator ($Z = 0$) locations are inverted. (a) Shows the dimensionless tangential velocity in the top cavity, (b) the dimensionless tangential velocity for the bottom cavity.

4.5.2. BOUNDARY LAYER THICKNESS

As was mentioned by Haddadi et al., centripetal and centrifugal flow have similar behaviour [40], but this is clearly not the case for a system with superimposed throughflow going from bottom to top. The system described by Haddadi had only one cavity and used either $C_w > 0$ or $C_w < 0$ to create centrifugal and centripetal flow. With the addition of the bottom rotor stator cavity (complete rs-SDR), the centrifugal and centripetal flow are not similar. This has a direct influence on r_{trans}, since the profiles suggest that $r_{trans,B} > r_{trans,T}$. The r_{trans} proposed by literature on the other hand (Equation 4.14) seems to be a good estimation of the average
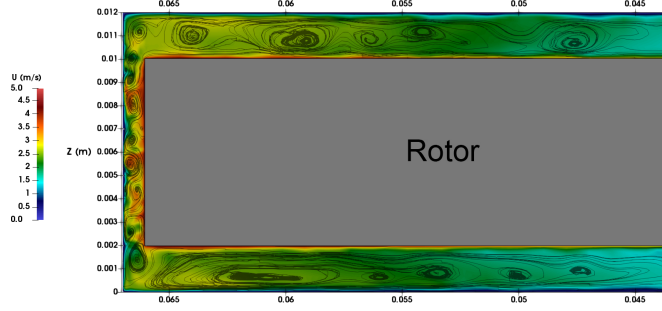
Figure 4.12: Instantaneous velocity streamlines in the vicinity at the rim of the rs-SDR at $\omega = 75$ rad/s and after $t = 0.5\tau$. The color gradient represents the instantaneous velocity magnitude.

r_{trans}. The same behaviour also holds for the radial velocity and the profiles are shown in the Supporting Information C.5.

The next interesting aspect to investigate was the thickness of the Von Kármán and Bödewadt layers. According to Van Eeten et al. the thickness of these layers should scale with $Re_h^{-1/2}$ and the layers should disappear when $Re_h \to \infty$ [44]. Since there is no common definition of the layer thickness, the approach proposed by Van Eeten et al. was used. Van Eeten et al. defines the Bödewadt layer thickness as the distance from the stator where the axial derivative of the rotational rate equals 0 (Equation 4.15), with u_θ being the tangential velocity in m/s at location r.

$$\left(\frac{\partial u_\theta(z)}{\partial z}\right)_{z=1-\delta_B} = 0 \tag{4.15}$$

The Von Kármán layer is predicted using the 99% boundary layer thickness approach. This assumes that the thickness of the Von Kármán layer is equal to the axial position at which the rotational rate equals 99% of the rotor velocity (Equation 4.16), with $U_{\theta,core} = U_\theta$ (Z=0.5) [44, 119].

$$U_\theta(\delta_K) = 1 - 0.99(1 - U_{\theta,core}) \tag{4.16}$$

When calculating the layer thickness, only the top rotor stator cavity was used at a radial position of $0.5R_D$. This to reduce the effects of the superimposed throughflow and the inlet, as Van Eeten et al. had determined this relationship for the thickness at $C_w = 0$. In Figure 4.13a, an example is shown on how to determine the thickness of the Bödewadt

(δ_B) and the Von Kármán (δ_K) layers from the LES simulation results by using Equation 4.15 and 4.16. Note that this is a schematic representation and that the values are calculated by using the *gradient* function in ParaView and the implementation of Equation 4.16. Figure 4.13b depicts the boundary layer thickness from the simulations (dots). It can be seen that the results from the LES simulation follow exactly (fitted $R^2 > 98\%$) the trend of $\delta_{B,K} \propto Re_h^{-1/2}$. One deviation from the literature is that δ_B does not go to zero at an infinite Re_h. One possible reason for this is the presence of a superimposed throughflow ($C_w > 0$), since the thickness was determined at $C_w = 0$ in literature. This leads to a net momentum transport that is imposed and it could lead to a change in boundary layer thickness to conserve momentum transport. To test this hypothesis, C_w was changed to 75 (half the original C_w) and 303 (double the original C_w) for the 50 rad/s case. These results are plotted in Figure 4.13 and it can be concluded that little change in boundary thickness was observed, relative difference for the Von Kármán layer was smaller than 2.3% and for the Bödewadt layer smaller than 1.5%. However, the difference in momentum transport was captured with a velocity change in both the Von Kármán and Bödewadt layer, hence change in momentum transport occurs via a change in the velocity in the boundary layer instead of the boundary layer thickness.
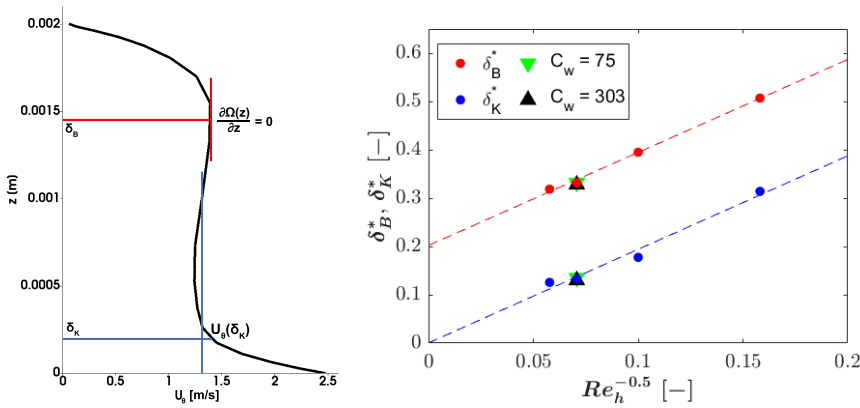

Figure 4.13: (a) Shows how to determine the thickness of both boundary layers from the LES simulation profiles. (b) Shows the thickness of the Von Kármán and the Bödewadt boundary layers at $r = 0.5 * R_D$. A trendline was included to show the scaling relationship with $Re_h^{-1/2}$ as was mentioned in the Introduction. This graph also contains the thickness at 50 rad/s with the $C_w = 75$ (upside down triangles) and $C_w = 303$ (triangles).

4.5.3. TURBULENT STATISTICS

This section will focus only on the turbulent characteristics of the rs-SDR at ω = 75 rad s^{-1} since the results for all the rotational rates are similar. The remaining results can be found in the Supporting Information C.7. From Figure 4.12 it can be concluded that the turbulence is more intense in the centripetal flow and is the highest at the rim of the rotor. Since the turbulent intensity is correlated with the total turbulent kinetic energy (TKE) (calculated as mentioned in the Supporting Information D.2), this value was quantified by plotting the turbulent kinetic energy for both rotor stator cavities at two different radial positions in Figure 4.14 [134]. The left graph shows the TKE at $0.4R_D$ and it can be seen that especially at the stator ($Z = 1$) the TKE in the centripetal flow is 2.5 times higher than in the centrifugal flow. Also, due to the larger effects of the superimposed throughflow, the TKE in the core is two times higher for the centrifugal flow. This indicates again that there is a difference in r_{trans} between both cavities. As can be seen in Figure 4.14, right, TKE at $0.99R_D$, there are only small differences between the cavities and that this difference is mainly in the core region. This graph also shows that the TKE is 4 to 6 times higher in the vicinity of the rim in comparison with $0.4R_D$. When the average TKE in the centripetal and centrifugal flow is determined, it results in a 10% higher turbulent intensity (I = $(2/3k)^{1/2}U^{-1}$) in the centripetal from compared to the centrifugal flow.
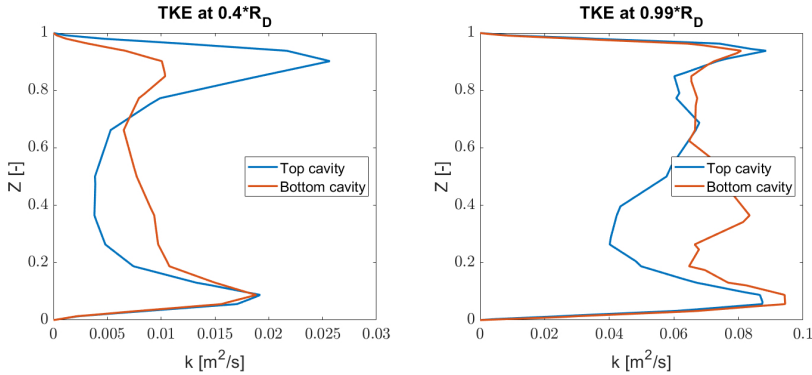

Figure 4.14: Time averaged turbulent kinetic energy at 75 rad/s, with Z = 0 denoting the rotor and Z = 1 the stator. The blue line represents the rotor stator cavity above the rotor and the orange line under the rotor.

Figures 4.15 and 4.16 contain the TKE colour plots made in ParaView for a slice at the inlet and at the rim of the rotor, respectively. Figure 4.15 visualizes the TKE from a radial position of 0 to $0.45R_D$ and it seems that

most of the energy is present in the top cavity, as was also shown in Figure 4.14. Furthermore, there are more turbulent structures present at the inlet than the outlet (see red lines) and this indicates the presence of the inflow being more dominant than the rotation of the disc in this region.
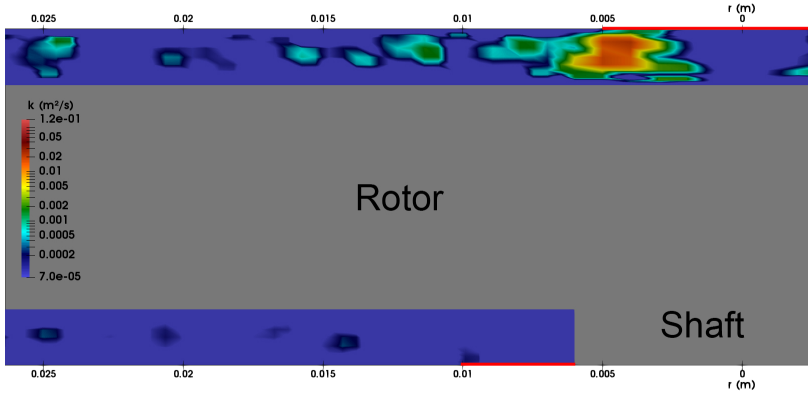

Figure 4.15: Colour plot of the turbulent kinetic energy after $t = 0.5\tau$ near the inlet (bottom) and the outlet (top) of the rs-SDR for $\omega = 75$ rad/s. The red lines denote the inlet (bottom) and the outlet (top). Note, the gradient range is a log scale and it was cut-off at $7.0 \cdot 10^{-5}$ m^2/s.

As was depicted in Figure 4.14, the turbulence near the rim of the rotor has the highest intensity. This is clarified in Figure 4.16 with the representation of TKE ranging from a radial position of $0.6R_D$ to R_S. The TKE distribution is shown to be most disordered in between the radial rotor and stator cavity, as was also shown in Figure 4.12.

The size of the smallest eddies in a turbulent flow is correlated to the Kolmorgorov size (Equation 4.6) since this is the scale where viscosity dominates and the turbulent kinetic energy is dissipated into heat [11]. It is then possible to estimate the smallest eddy size from the energy dissipation rate and to locate the positions where the bulk of the heat is dissipated. The total energy dissipation rate (ϵ_{tot}) was calculated by combining the sub grid scale (ϵ_{SGS}, directly from OpenFOAM) and the resolved (ϵ) energy dissipation rates with the use of Equations 4.17-4.19 [135], with ν_{eff} being the effective kinematic viscosity and $\mathbf{S_{ij}}$ the strain rate tensor.

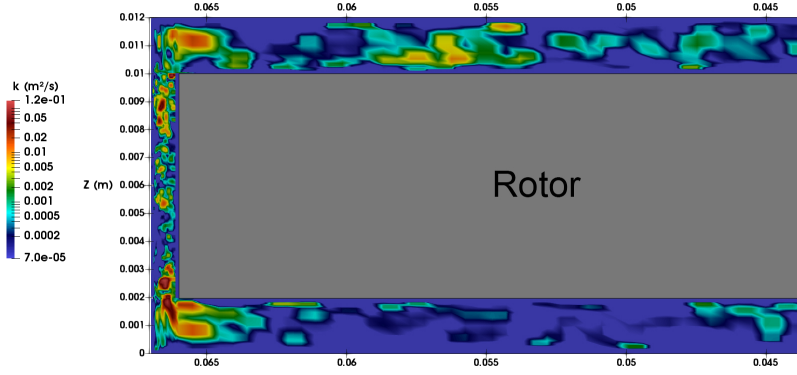$$\epsilon_{tot} = \epsilon_{SGS} + \epsilon \tag{4.17}$$

Figure 4.16: Colour plot of the turbulent kinetic energy after $t = 0.5\tau$ at the rim of disc for $\omega = 75$ rad/s. Note, the gradient range is a log scale and it was cut-off at $7.0 \cdot 10^{-5}$ m^2/s

$$\epsilon = 2\nu_{eff}\overline{\mathbf{S_{ij}S_{ij}}} \tag{4.18}$$

$$\mathbf{S_{ij}} = \frac{1}{2}\left(\frac{\partial u'_i}{\partial j} + \frac{\partial u'_j}{\partial i}\right) \tag{4.19}$$

The total dissipation rate is plotted in Figure 4.17 and the left graph visualizes the energy dissipation rate at $0.4R_D$ and the right graph at $0.99R_D$. The rotor is positioned at $Z = 0$ and according to simulation results, contains five to six times more energy than the Bödewadt layer ($Z = 1$). It also shows that there is more energy present in the centripetal flow and is likely due to the inlet effects, since these increase the throughflow dominated region. This could reduce the turbulence at the vicinity of the inlet. Hence, a decrease in turbulent kinetic energy that will be dissipated into heat is observed in this region, which is also seen by a similar ϵ in both cavities in the vicinity of the rotor rim. This is also the region where rotation is dominating and the effects of superimposed throughflow can be neglected. Another interesting observation is that the dissipation rate is approximately eight to nine times higher near the rotor rim compared to a radial position of $0.4R_D$. The estimated eddy sizes in the Von Kármán layer are: 3.34 and 5.62μm at $0.4R_D$ and $1.94-2.02\mu m$ at $0.99R_D$ and in the Bödewadt layer: $5.95-6.69\mu m$ at $0.4R_D$ and $2.66-2.73\mu m$ at $0.99R_D$. It can be expected that the eddies would be smaller at the Von Kármán layer

since this layer is formed at the rotor and consists of the most energy dense section.
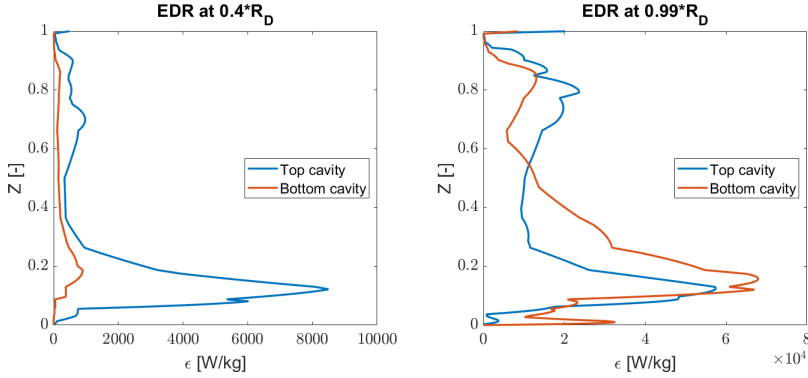

Figure 4.17: Time averaged energy dissipation rate at 75 rad/s, with Z = 0 denoting the rotor and Z = 1 the stator. The blue line represents the rotor stator cavity above the disc and the orange line under the disc.

4.6. CONCLUSION

This research successfully simulated a complete rotor stator spinning disc reactor with CFD, connecting the top and bottom rotor stator cavity along with superposed throughflow, using LES with WALE as the turbulence model in OpenFOAM 9. The LES simulation was validated at especially the higher rotational Reynolds numbers, or more particularly in the turbulent torsional Couette regime. New insights were obtained on the flow behaviour inside the rs-SDR. The literature assumes similarity between the top and bottom rotor stator cavities, but simulations show that this is not the case. In fact, the transition radius was found to be higher for centrifugal flow (bottom cavity), indicating a larger PFR dominated regime in comparison to centripetal flow (top cavity). The proposed transition radius in literature could be seen as an average radius between both cavities. This method was also validated on basis of the thickness of the Von Kármán and Bödewadt layers. The LES simulations follow the proposed trend ($\delta_{B,K} \propto Re_h^{-1/2}$) from literature. Finally, the method is validated by the entrainment coefficient, which shows to be in good agreement with the literature correlation. However, the correlations are only valid the turbulent cases. After validation, the simulations were used to determine the local turbulent intensity. The highest turbulence intensity is observed at the vicinity of the rotor rim and in the Von Kármán layer. Therefore the WALE model was the most suitable as it describes

the turbulence more accurately near the wall, and in the rs-SDR the Von Kármán and Bödewadt layers. The centripetal flow contains more turbulent kinetic energy, resulting in a 10% higher turbulent intensity compared to the centrifugal flow. This was due to the inlet effects being more present in the centrifugal flow and resulted in a higher transition radius for the bottom cavity. Overall, these results gave better insight in the hydrodynamic behaviour of a complete rs-SDR, by connecting the top and bottom rotor-stator cavities into one simulation and in combination with the developed dispersion model this work could be used to create more realistic and accurate reactor models. This leads to a reduction in the utilisation of resources/energy and a more intensified process. For future work, the results can be used to determine optimal operation of rs-SDRs. For instance, for the photochemical spinning disc reactors, a particular focus can be on matching areas of high light irradiation with high mixing zones. Furthermore, simulations studies can be carried out to study more complex fluids in the rs-SDR, for example, non-Newtonian fluids, which are prevalent in industrial processes.
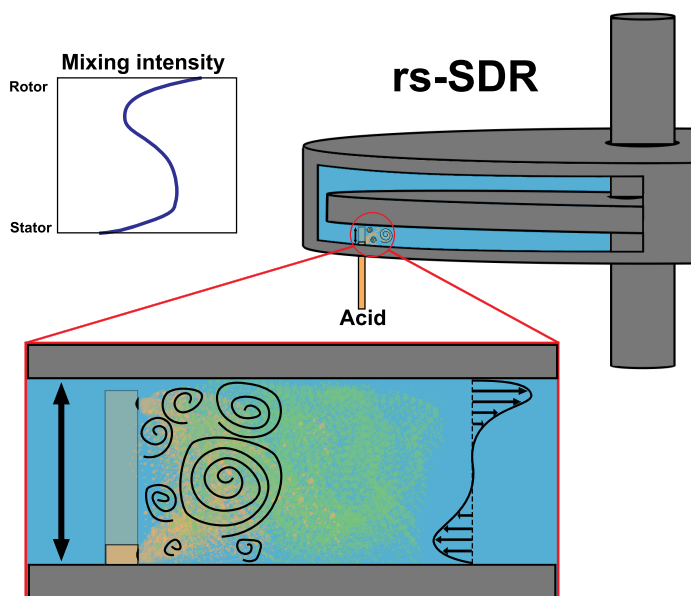
CHAPTER 5

MICROMIXING EFFICIENCY IN THE TURBULENT BOUNDARY LAYERS IN A ROTOR-STATOR SPINNING DISC REACTOR

5

Abstract

The effect of turbulent boundary layers on the micromixing efficiency is experimentally and numerically investigated for a rotor-stator Spinning Disc Reactor (rs-SDR). The experimental work uses the Villermaux-Dushman reaction in order to determine the micromixing time (t_{mix}). During the experiments a probe was used to inject $HClO_4$ at different axial locations between the rotor and the stator and showed that the mixing intensity was the highest in the Von Kármán layer and lowest in the Bödewadt layer, however t_{mix} shifted towards a single value with increasing rotational rate. t_{mix} did not follow the engulfment model (~ 10 times higher) as the probe caused a disturbance in the flow field. As for the numerical work, a rotor-stator cavity flowfield was developed in OpenFOAM 9 with Large Eddy Simulations (LES) and the Wall-Adapting Local Eddy viscosity sub-grid-scale model (WALE) and was validated with velocity profiles found in literature. Lastly, t_{mix} from the simulations agreed with the experimental t_{mix} in the core region. However, there was a discrepancy in the boundary layers, which was likely due to the difference in rotor-stator gap as this results in different velocity gradients, hence different turbulent intensity and t_{mix}.

5.1. INTRODUCTION

The chemical industry is moving towards a more environmentally friendly and intensified operation to reduce the carbon footprint and greenhouse gasses [140]. An example to reduce the negative aspects of the chemical industry is by optimisation of the processes, e.g. development of novel equipment, optimising operation regimes or catalyst development. The rotor-stator spinning disc reactor (rs-SDR) is a novel device that has promising features for the chemical industry [14, 15]. This reactor exists out of a rotating disc (rotor) that is enclosed by a casing (stator) and are generally separated by a few millimeters, a schematic view is depicted in Figure 5.1. Due to this small separation high velocity gradients arise, which result in high levels of turbulence and this would: decrease the diffusion path length and for multiphase systems increase the mixing (macro-, meso- and micromixing) properties of the system in combination with the interfacial area [12]. Next to the high turbulent flow, also high shear rates are formed and in multiphase flows for instance, the shear forces result in a reduction of bubble/droplet size, this enhances the specific interfacial area [18, 106, 107]. This reactor has also proven to increase the heat transfer by manufacturing cooling/heating channels in the stator [25, 26]. The rs-SDR has showed to enhance gas-liquid [16, 31, 108], liquid-liquid [18–22, 30, 141] and liquid-solid [22, 23] mass transfer rates. Additionally, the reactor has also shown to enhance mixing application, such as micromixing, viscous mixing and mesomixing [29–31, 128, 142].
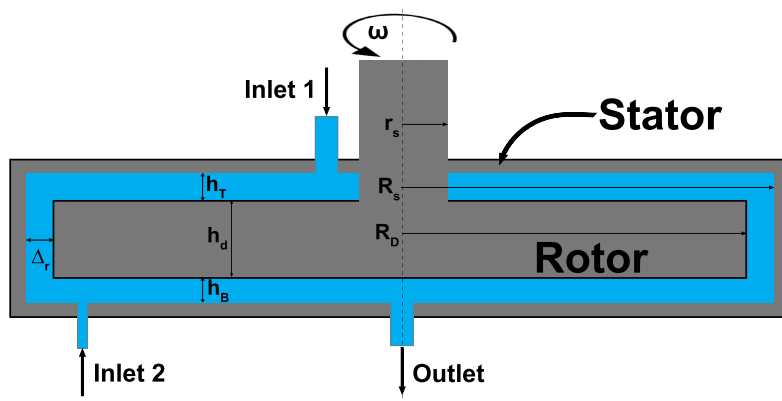

Figure 5.1: A schematic representation of the rotor-stator spinning disc reactor with, R_s the radius of the stator, R_D the radius of the rotor, r_s the radius of the shaft. The axial clearances are denoted as h_T and h_B, the thickness of the disc as h_D and the radial clearance by Δ_r. The bulk inlet (Inlet 1), injection inlet (Inlet 2) and outlet are also depicted in this figure.

In order to understand and improve the rs-SDR, studies on the hydrodynamic behavior have extensively been performed. In the turbulent regime, high rotational Reynolds numbers ($Re = \omega R_D v^{-1}$), two turbulent boundary layers are formed, namely a Von Kármán boundary layers at the rotor, and a Bödewadt boundary layer at the stator [35, 36]. Daily and Nece [37] found that the boundary layer can be either separated or merged, depending on the Reynolds number and gap width ($G = h_T R_D^{-1}$). These differences were later on described in a flow map and divided into four different hydrodynamic regimes based on Re and G [38], see Figure 5.2 and the four regimes are denoted below:

- Regime I: laminar flow with merged boundaries

- Regime II: laminar flow with separated boundaries

- Regime III: turbulent flow with merged boundaries

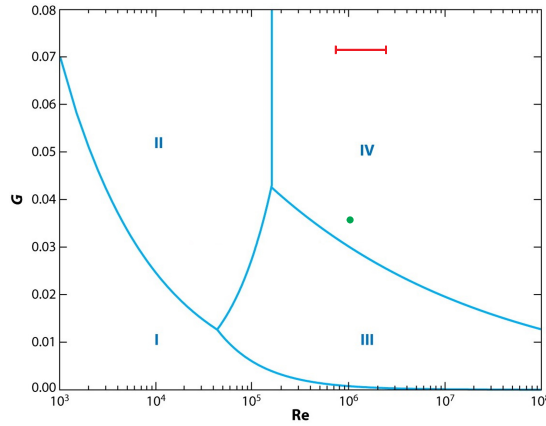- Regime IV: turbulent flow with separated boundaries

Figure 5.2: The flow regimes in the rs-SDR according to Daily and Nece and Launder et al. [37, 38]. The red line indicates the experimental range. The green dot is validation of the turbulent simulation case from Poncet et al. [41].

When the Von Kármán and Bödewadt layers are separated by an inviscid core, it is often referred to as Batchelor flow [126]. In the situation without an inviscid core, the Von Kármán and Bödewadt layers are merged and the flow is known as torsional Couette flow [40]. Additionally, a net positive throughflow in the rs-SDR ($C_w > 0$ with $C_w = Q v^{-1} R_D^{-1}$) could divide the hydrodynamic regime into two parts, throughflow dominated

and rotational dominated regimes. At the lower radial positions the flow is throughflow dominated, flow behaves as plug flow and at the higher radial positions the flow will be rotational dominated. In the rotationally dominated regime, the flow is assumed to behave as ideally mixed on a macroscopic level and this regime contains the highest turbulent intensity [143]. Therefore it is expected to also have the highest micromixing efficiency, since experimentally determined micromixing times in the rs-SDR tend to follow $\epsilon^{-0.5}$ [30, 142, 144]. The experiments were performed with the Villermaux-Dushman method [145] in combination with UV/VIS to determine the conversion in the rs-SDR. The experimentally determined t_{mix} also corresponds with the relationship based on the engulfment model, Equation 5.1 which is derived from Equations 5.2 to 5.4 since t_{mix} can be viewed as the inverse of the engulfment rate (E) [10].

$$t_{mix} = 17.24 \left(\frac{\nu}{\epsilon}\right)^{1/2} \tag{5.1}$$

$$\frac{dV_m}{dt} = EV_m \tag{5.2}$$

$$\int_{V_0}^{2V_0} \frac{1}{V_m} = E \int_r^{\tau} dt \tag{5.3}$$

$$E = \frac{ln2}{\tau} = 0.058 \left(\frac{\epsilon}{\nu}\right)^{1/2} \tag{5.4}$$

Next to the experimental work in the rs-SDR, also fundamental work was performed. Computational fluid dynamics (CFD) studies were done for studying the hydrodynamics in rotor stator systems [38–42] and successfully described different aspects of a rotor stator cavity. During this work most of the simulations were done with the Reynolds Stress Model (RSM) and Large Eddy Simulations (LES) and the focus was mainly on the axial velocity profiles (used as a validation in this study), the Reynolds stresses and pressure distributions for different Reynolds number, C_w ($0 < C_w \geq 0$) and G. Additionally, fundamental studies were executed by Van Eeten et al. to describe the thickness of the Von Kármán and Bödewadt layers in a rotor-stator cavity [44, 45]. This study derived a direct relationship between the Reynolds number ($Re_h = \omega h_T^2 \nu^{-1}$) and the thickness of the Von Kármán ($\delta_K \propto Re_h^{-1/2}$) and Bödewadt ($\delta_B \propto Re_h^{-1/2}$) layer. The proposed relationship by Van Eeten et al. is presented in Equation 5.5. All this work was done for a single rotor-stator cavity. A CFD study with LES in OpenFOAM was performed in Chapter 4 and combines

both rotor-stator cavities of the rs-SDR with a net positive throughflow [143]. This allowed the visualisation of the entire flow field and capture the most intense turbulent zones in the rs-SDR. Also, the macromixing behavior was visualised.

$$\delta_B = \frac{4.9025}{\sqrt{Re_h}}, \qquad \delta_K = \frac{2.7203}{\sqrt{Re_h}} \qquad (5.5)$$

Since no studies were done in the rs-SDR focusing on the dependency of the turbulent boundary layers on the micromixing, this study will focus on axial dependency on the micromixing times in rotational governed Batchelor flow in a rs-SDR. The mixing times will be determined by performing experiments with the Villermaux-Dushman method [145] in a rs-SDR and as an addition, simulations will be performed in a single rotor-stator cavity with LES in OpenFOAM 9 to determine the mixing time as function of the gap width. During the experimental work, the flow rate is minimised (C_w = 2.32) to ensure a rotation dominated flow and the simulation will be performed at C_w = 0. As a practicality, the experiments were performed with Re = 0.63 - 1.49 · 10 [6] and G = 0.072 (red line Figure 5.2) to determine t_{mix} at different axial positions, since smaller G would make injections at different heights more difficult. LES was performed at Re = 1.00 · 10 [6] with G = 0.036 (green dot Figure 5.2) since the validation results were also performed in this geometry [41]. This work will contain the micromixing times determined at different axial positions to distinguish the turbulent boundary layers, a LES validation based on the work of Poncet et al. [41] and a comparison between the experimentally and computationally (with LES) determined t_{mix} in the rs-SDR.

5.2. EXPERIMENTAL METHOD
This section will explain the procedure for the micromixing characterisation and the experimental procedure. During the experiments an acid will be injected in a circulating buffer solution (semi-batch) and monitored at the in- and outlet of the rs-SDR via an UV/VIS spectrometer. The tested variables are, the rotational Reynolds number and the axial injection position of the acid.

5.2.1. MICROMIXING CHARACTERIZATION
The extent of micromixing in a rs-SDR is assessed using the Villermaux-Dushman parallel competitive reaction scheme [145]. It entails the addition of an acid to a buffer solution containing another reactant which

can undergo a competitive reaction. The following two reactions are considered:

$$B(OH)_4^- + H^+ \longrightarrow B(OH)_3 + H_2O \tag{5.6}$$

$$IO_3^- + 5I^- + 6H^+ \longrightarrow 3I_2 + 3H_2O \tag{5.7}$$
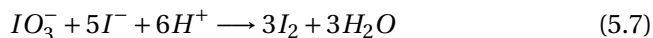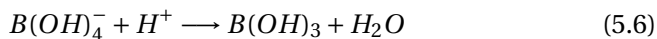
The neutralization reaction of the acid by the buffer, Reaction 5.6, is assumed to be instantaneous, while the competing reaction 5.7 is a fast reaction with a characteristic time in the same order of magnitude as the micromixing time [30]. Adding a small amount of acid to an excess of buffer solution will cause the acid to be the limiting reactant. In a perfectly mixed situation, all acid will be consumed in the faster neutralization reaction. However, when the system is not perfectly mixed, some acid will also be consumed in the second reaction. Due to high local acid concentrations in a poor mixed system. Here, all $B(OH)_4^-$ will be consumed and the remaining acid will react with the iodine. The extent of the second reaction taking place is thus an indicator of the unmixedness of the system. The higher the concentration of product I_2 of reaction 5.7, the worse the mixing. The formed iodine reacts further in a quasi instantaneous equilibrium reaction with iodide anions to form triiodide:

$$I_2 + I^- \longleftrightarrow I_3^- \tag{5.8}$$

With the associated equilibrium constant as a function of temperature (T) [30]:

$$log_{10}K_B = \frac{555}{T} + 7.355 - 2.575 log_{10}T \tag{5.9}$$

Conveniently, triiodide is UV active and its concentration can be experimentally determined. This in combination with the known equilibrium of I_2 and the ratio between I_2 and I^- from Reaction 5.8 allows us to calculate the amount of product formed in Reaction 5.7. The selectivity towards Reaction 5.7, denoting the extent of unmixedness, is given as follows:

$$Y = \frac{2(n_{I_2} + n_{I_3^-})}{n_{0,H^+}} = \frac{2V_{total}([I_2][I_3^-])}{V_{injection}[H^+]_0} \tag{5.10}$$

Subsequently, the experimentally accessible selectivity has to be translated to a mixing time. The limiting step in micromixing is engulfment, characterizing the mixing time (t_{mix}). The acid engulfs part of the bulk

solution, increasing the volume of the acid, which is regarded as the mixing volume. When micromixing (rate of engulfment) is very fast, the mixing volume has increased to such extent that enough buffer is available to neutralize the acid, before the second reaction (Dushman reaction) can occur (slower). However, when micromixing is not that fast, the incorporation of buffer solution is not sufficient to neutralize all the acid, Reaction 5.7 will take place. In Equation 5.11, the mole balance for a species in the mixing volume (V_m) is given [145].

$$\frac{dn_i}{dt} = \frac{dC_i V_m}{dt} = E V_m t_{mix} C_{bulk} + R_i V_m \tag{5.11}$$

The change in the number of moles of i is thus a function of the number of moles that are engulfed and that react. Equation 5.11 can be rewritten by using the product rule and Equation 5.2 and leads to Equation 5.12. Note that the engulfment rate is the inverse of the micromixing time.

$$\frac{dC_i}{dt} = \frac{C_{bulk} - C_i}{t_{mix}} + R_i \tag{5.12}$$

The balance above is formulated for all relevant species in the Villermaux-Dushman system. In order to solve the mole balances, a description of the reaction kinetics is needed. As aforementioned, Reaction 5.6 is assumed instantaneous. This leads to the equation as stated in Equation 5.13, representing the observation that all $B(OH)_4^-$ that enters the mixing volume will immediately react away if there is still H^+ left.

$$R_1 = \begin{cases} \frac{C_{bulk,B(OH)_4^-}}{t_{mix}} & \text{for } C_{H^+} > 0 \\ 0 & \text{for } C_{H^+} = 0 \end{cases} \tag{5.13}$$

The kinetics of Reaction 5.7 for monoprotic acids is given as follows [142]:

$$R_2 = k_2 C_{IO_3^-} C_{I^-}^2 C_{H^+}^2 \tag{5.14}$$

The rate constant k_2 is a lumped variable that also includes the effects of the non-ideality of the solution. Using a uniform activity coefficient (γ) for all species, with $k_{2,0}$ the reaction rate coefficient at infinite dilution, k_2 is given as follows:

$$k_2 = k_{2,0} \gamma^4 \tag{5.15}$$

The fourth power arises from the activity coefficient of the reagents (5 species), divided by the activity of the activated complex [30]. The activity coefficient for the electrolyte solution is given in Equation 5.16.

$$log_{10}\gamma = -0.51\frac{\sqrt{I_s}}{1+\sqrt{I_s}} + \frac{(0.06+0.6B_m)I_s}{(1+1.5I_s)^2} + B_m I_s \qquad (5.16)$$

With I_s the ionic strength of the solution and B_m and $k_{2,0}$ are fitted parameters:

$$I_s = 0.5\sum_i C_i z_i^2 \qquad (5.17)$$

$$B_m = 0.01347M^{-1} \qquad (5.18)$$

$$k_{2,0} = 1.12\cdot 10^9 M^{-4} \qquad (5.19)$$

The iodine-triiodide equilibrium (Equation 5.8), is modeled with a finite forward ($k_{5.8} = 5.6\cdot 10^9$) and backward ($k_{-5.8} = 7.5\cdot 10^6$) reaction rate [146]. Using a given micromixing time, the mole balances for the species in the mixing zone now can be solved. As initial condition a concentration of zero for all species was given, except for H^+. Conversely, the mole balances can also be used to find a specific mixing time corresponding to the experimentally obtained concentration set by fitting. The mole balances are solved by using Matlabs *ODE15s* function.

5.2.2. Experimental Setup

The experimental setup for the micromixing determination is schematically depicted in Figure 5.3. Within the system the rs-SDR is depicted and the rotor had a diameter of 0.143 m, while the stator had a radius of 0.145 m, yielding a radial clearance of $2\cdot 10^{-3}$ m. The axial clearance for the bottom part was $1.025\cdot 10^{-2}$ m and $1.038\cdot 10^{-2}$ m for the top part. This was the maximum gap height achievable in this setup and was used to have a large(r) variation of the axial coordinate. Note that usually in spinning discs the axial clearance is much smaller [19, 30]. The total reactor volume was $1.13\cdot 10^{-4}$ m^3. The bulk solution was fed into the rs-SDR at the top using a gear pump with a constant flowrate of $7.5\cdot 10^{-6}$ m^3 s^{-1}, regulated with a Bronkhorst Cori-Flow mass flow controller. In Table 5.1 are the reagents for the bulk and acid solutions.

The acid was injected at the bottom. By altering the length of the inlet tube (inner diameter $0.5\cdot 10^{-3}$ m), the injection point was varied over the axial clearance of the bottom part of the reactor, see a schematic
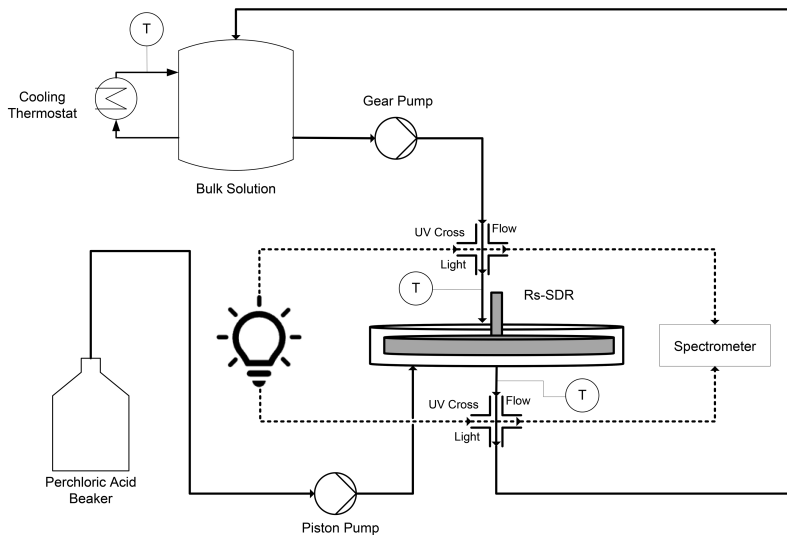
Figure 5.3: A schematic representation of the setup used for the micromixing characterisation in the rs-SDR.

Solution	Reactant	Concentration [M]
	H_3BO_3	0.1818
Bulk	NaOH	0.0909
Solution	KIO_3	0.00240
	KI	0.0121
Acid	$HClO_4$	1.04

Table 5.1: Set of concentrations used for the experiments.

side view in Figure 5.4. Accordingly, the injection direction can be varied between four different directions, with the flow (Con), against the flow (Anti) or perpendicular to the flow in either the radial inward (Centripetal) or outward (Centrifugal) direction. The different directions are presented in the top view from Figure 5.4 and the majority of the experiments are conducted with a centripetal injection.

The acid was injected with a flow rate of $3.33 \cdot 10^{-7}$ m^3 s^{-1} to ensure being in the micromixing regime, using a KNAUER Smartline Pump 1050. The injection point was located at a radial position of 0.130 m. A Lauda ECO RE 630 was used to cool the buffer tank and remove any dissipated heat that was caused by the rs-SDR [30]. Inline UV/VIS measurements for the in- and outlet were performed using a Dual channel Avaspec-2048-2-USB2
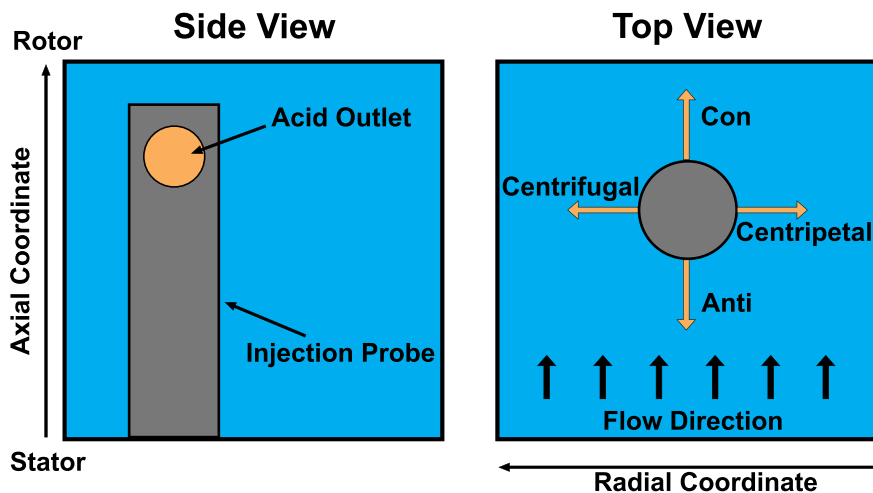
Figure 5.4: A schematic representation of the injection probe, with a side view and a top view. The top view contains the different injection directions with respect to the flow.

spectrometer. The flow cells at the in- and outlet had a pathlength of 5 mm and 10 mm respectively. An Avalight DH-S light source was used, and the intensity at a wavelength of 353 nm was recorded every 0.1 s to obtain the concentrations of I_3^-. The recorded intensity (N) was linked to the absorbance using the intensity of the original bulk solution (N_{ref}) and the intensity in the absence of a light source, i.e. dark reference (N_0), as follows:

$$A = -\frac{log(N - N_0)}{log(N_{ref} - N_0)} \tag{5.20}$$

The absorbance can be linked to the triiodide concentration at low concentrations ($< 1 \cdot 10^{-4}$ M [30]) using the Lambert-Beer law 5.21. During the experiments it was made sure that the concentrations never exceeded $0.8 \cdot 10^{-4}$ to remain in the linear regime of the Lambert-Beer law.

$$A = \epsilon_M l C_i \tag{5.21}$$

The linear relationship between the absorbance and triiode concentration was verified by a calibration of triiodide at 353 nm for the specific UV/VIS flow cells used at the in- and outlet of the reactor. At the inlet, a molar absorption coefficient of 2133.5 m^2 mol^{-1} was found and 284.7 m^2 mol^{-1} at the outlet.

5.2.3. DATA PROCESSING

The UV/VIS signal at 353 nm was recorded at the inlet and outlet of the reactor. Additionally, the data of the rotor-stator Spinning Disc Reactor itself was logged, being, among others, the rotational rate, torque, and reactor temperature. In Matlab, the UV/VIS data was averaged over a time span and the rs-SDR was linked using the recorded date times in both files. After every injection it was made sure that the UV/VIS signal was stabilized, indicating that the triiodide concentration was homogeneous throughout the experimental system, including the bulk tank.

Using the UV/VIS transmission of the inlet UV/VIS cell the I_3^- concentration was calculated and the amount of triiodide formed due to the acid injection was determined. With the obtained I_3^- concentration the extent of the iodide equilibrium (Reaction 5.8) could be calculated, with the equilibrium constant evaluated at the temperature at the inlet of the reactor (Equation 5.9). Combining the extent of the equilibrium with the known ratio between the consumed iodide and produced iodine, the extent of the Dushman reaction (Reaction 5.7) was calculated. From this, the selectivity towards the Dushman reaction could be determined knowing the amount of acid injected and the difference in the extent of the Dushman reaction before and after the acid injection.

Using a set of dimensionless mole balances for the various reactants and products in the mixing zone [145], based on Equation 5.11, the micromixing times could be determined. The mole balances were solved using the Matlab solver *ode15s* for stiff ordinary differential equations. The initial (dimensionless) concentration of the acid in the mixing value was unity, while for the other species the initial value was zero. The bulk concentration of the reactants (outside of mixing volume) was the initial concentration of the experimental solution (see Table 5.1). The integration time of the mole balances was set to the time for the mixing volume to become equal to the total volume of the system [145]. The initial volume of the mixing volume was equal to total volume of injected acid. The mole balances were solved with a set micromixing time. Using the Matlab function *lsqnonlin*, the error between the selectivity predicted by the mole balances and the experimentally obtained selectivity was minimized by varying the micromixing time. To compare the experimentally obtained micromixing times with the engulfment theory of micromixing [10], the local energy dissipation rate was estimated. The total power exerted by the rotor on the fluid can be obtained from the current supplied to the motor [17]:

$$E_{dr} = \omega M = \omega(I - I_0)M_C \qquad (5.22)$$

I_0 and M_C (6.47 N) are motor characteristics, with I_0 the idle current, which is determined by disconnecting the motor from the rs-SDR and denote the current at different rotational rates. The dependency of the local energy dissipation rate on the radius (r) is assumed to be as follows:

$$\epsilon_{loc} \propto r^{5/2} \qquad (5.23)$$

Based on the radial dependency and the motor current the local energy dissipation at the injection location was estimated. The derivation of the radial dependency and the final expression of the local energy dissipation rate based on the measured current can be found in Supporting Information D.1. Subsequently, the local energy dissipation was used to estimate the theoretical expected micromixing time using Equation 5.4.

5.3. NUMERICAL MODELING
The computational fluid dynamics simulation of flow in the rotor-stator spinning disc reactor were performed in OpenFOAM 9 [132]. OpenFOAM is an acronym for Open Source Field Operation and Manipulation. Generally OpenFOAM solves the Navier-Stokes equations numerically using the Volume of Fluid method.

5.3.1. LARGE EDDY SIMULATION
In Large Eddy Simulations (LES), not only the mean flow is solved, but also a part of the turbulence characteristics. The instantaneous velocity is filtered, resulting in a filtered/smoothed velocity in which only the large fluctuations persist. These large fluctuations are caused by the larger eddies, as they contain most of the turbulent energy and are more likely to be anisotropic and inhomogeneous compared to the small eddies. The small scale eddies, or Sub-Grid Scale (SGS), are modeled in LES. This method has an increased accuracy compared to Reynolds Averaged Navier-Stokes (RANS), but on the other hand it is less accurate compared to Direct Numerical Simulations DNS [51]. The velocity filtering can be done explicitly or implicitly. Explicit filters apply a spatial filter to the Navier-Stokes equations and an implicit filter is applied to the discretization schemes [147]. Using the finite volume method, the Navier-Stokes equations are integrated over control volumes. The size is equal to the grid size and everything larger is explicitly modeled, while the smaller effects are averaged out. A drawback of this approach is, that it is

impossible to distinguish between numerical (discretization) errors and modeling errors, and a fully grid-independent solution cannot be obtained as with the refinement of the mesh also smaller-scale motions are resolved [51]. Therefore a good method to evaluate the accuracy of the grid was introduced by Pope [134]. He showed that when 70% of the turbulent kinetic energy (TKE) is resolved, the grid is accurate enough to perform a proper LES. The simulations in this work solved 99.9% of all the the kinetic energy, more details can be found in the Supporting Information D.2. Also, the average grid size over the entire domain is only 0.2% bigger than the average Kolmogorov length (DNS scale) determined from the flow field, Equation 5.24 [11].

$$\eta = \left(\frac{\nu^3}{\epsilon}\right)^{1/4} \tag{5.24}$$

The LES was combined with the Wall-Adapting Local Eddy viscosity (WALE) sub-grid scale model (SGS) [135]. This model was chosen due to its capability in capturing the rotational aspects of the turbulent flow adequately [135]. Additionally, the Von Kármán layer contains the most turbulence and therefore WALE is also more suitable as it describes the turbulence more accurate near the walls [143]. Regarding the LES filter width, denoting the cutoff between the resolved and unresolved turbulence scales, the setting *cubeRootVol* was selected. This implies that the filter width is calculated by the cubic root of the cell volume. This is a common choice in OpenFOAM, and means that filtering is a direct function of the grid size (implicit filtering) [132].

5.3.2. NUMERICAL METHOD

The geometry was recreated from the experimental set-up from the study of Poncet et al. in OpenFOAM 9 using *blockMeshDisct* [41]. The mesh consisted out of $21 \cdot 10^6$ grid cells (300 x 500 x 140; r, θ, z). When the z^+ value is around or below 1, it is reasonable to assume that the near-wall region is resolved, this is important due to multiple cells being located in the viscous sublayer [42]. The z^+ value was checked *posteriori* using the OpenFOAM *yplus* utility and it resulted in an average value below 1 with a maximum of 1.5. Next to the percentage of resolved TKE and the z^+ value, also a grid study was performed and it was verified that there is no effect of the grid size on the accuracy when a mesh was used with twice the number of grid cells.

Since Hop et al. performed similar simulations [143], it was assumed that their interpolation schemes would also work for this simulation. Only

the divergence scheme was changed from *Gauss cubic* into *Gauss vanLeer*, our experience showed that changing this, a more stable simulation was obtained. The implemented interpolation schemes are depicted in Table 5.2.

Mathematical term	Interpolation scheme
Gradient	Gauss cubic
Divergence	Gauss vanLeer
Laplacian	Gauss cubic corrected
Interpolation	Cubic
Surface-normal gradient	Cubic corrected

Table 5.2: Interpolation schemes that were used in the rotor-stator cavity simulation.

In OpenFoam, the temporal discretization is performed separately from the spatial discretization, and is referred to as the method of lines [132]. This allows for the flexibility of having different schemes and hence accuracy in the temporal and spatial discretization. Here, a blended Crank-Nicholson discretization scheme was used to minimise the unstable and oscillatory behavior for the temporal discretization. The blended scheme consists out of Crank-Nicholson together with a backward Euler scheme and is unconditionally stable. An off-centering coefficient of 0.9 was used (1 corresponding to full Crank-Nicholson and 0 to full backward Euler). This value is generally used and allows for a stabilized scheme while maintaining high accuracy [132]. For the pressure, the Geometric agglomerated Algebraic MultiGrid (GAMG) solver was used and for other quantities such as the velocity the smoothSolver solver was used. Additionally, a preconditioner and smoother were used with both solvers, respectively the Diagonal-based Incomplete Cholesky (DIC) and GaussSeidel method. The residual tolerance was set to $1 \cdot 10^{-6}$.

The flow solver *pisoFoam* was used on 256 cores on the Dutch supercomputer Snellius and it couples the pressure and velocity equations. This poses numerical difficulties as small pressure gradients can yield large velocity changes, making a sequential approach very unstable. This is resolved by making use of a pressure correction method. The pressure velocity coupling was performed using the Pressure Implicit Splitting Operator (PISO) algorithm [136], which uses two predictor-corrector steps. In the first step, an intermediate velocity is calculated after which a pressure correction is computed using a Poisson equation to satisfy the continuity equation. The corrected pressure is used to recalculate

the velocity. The solver iterates till convergence is reached, i.e. till the difference between subsequently predicted velocities is smaller than a threshold [148]. The time step size was initially set to $1 \cdot 10^{-7}$ s because at the start the temporal changes are relatively large and possibly causing numerical instabilities. When the Courant Friedrichs Lewy number (CFL or Co = $u_{r,\theta,z} \, \Delta t \, \Delta^{-1}_{r,\theta,z}$) decreased to 0.05, the time step size was increased with one order of magnitude. This was repeated until a stable CFL number was obtained. Adaptive time-stepping, which is available in OpenFoam, was not used as it changed the time step size too aggressively which leads to stability issues. A steady state was obtained when the differences in average velocity did not change between the time steps and was typically reached after approximately 0.6 rotations. These runs took about $7 \cdot 10^{4}$ time steps with 29 s of simulation time per time step.

5.3.3. INITIAL AND BOUNDARY CONDITIONS

For the velocity, pressure, and turbulent viscosity boundary conditions were specified. The velocity was set to zero at the stator and the function *rotatingWallVelocity* was applied to the rotor with a set velocity of 16 rad s^{-1}. This corresponds to a rotational Reynolds number of $1 \cdot 10^{6}$ and is equal to the experimental system of Poncet et al. [41]. At the inlet and outlet, the tangential component of the velocity was set to vary linearly from ωr at the rotating wall to zero at the stationary wall. All boundaries for the pressure and the turbulent viscosity were given a *zeroGradient* boundary condition.

The bulk fluid was initialized with a rotational rate of K · ωr saving computational costs to bring the bulk fluid into motion. K is referred to as the entrainment coefficient and it is the ratio between the tangential velocity of the inviscid core compared to the local rotational rate of the rotor and was set to 0.4 [41]. This corresponds to the steady-state value obtained for the entrainment coefficient in a rotor-stator system with similar dimensions and Re number [41]. In other systems this values tends to be 0.31, however these systems have smaller dimensions and the entrainment coefficient was numerically determined [44, 119]. The initial profile did not account for differences in profile in the boundary layers and it remains constant in the axial direction. The pressure was initialized at zero (reference value), while the turbulent viscosity was initialized at the value of the kinematic viscosity of the fluid ($1 \cdot 10^{-6}$ m^2 s^{-1}).

5.4. RESULTS

This section will discuss the experimental micromixing results and the results obtained by employing the CFD model. The CFD results will consist out of a validation and a characterisation for micromixing times and shear rates. During this section $Z = 0$ ($Z = 1 - z/h_B$) will represent the rotor.

5.4.1. MICROMIXING EXPERIMENTS

The outlet of the injection tube is located at the side of the inlet tube. This has as a benefit that the acid can be injected perpendicular to the flow (directed inwards or outwards), with the rotation direction of the flow, or against the direction of the flow. However, this could lead to a disturbance in the flow field and significantly influence the micromixing results, therefore the influence of the injection direction was investigated first.
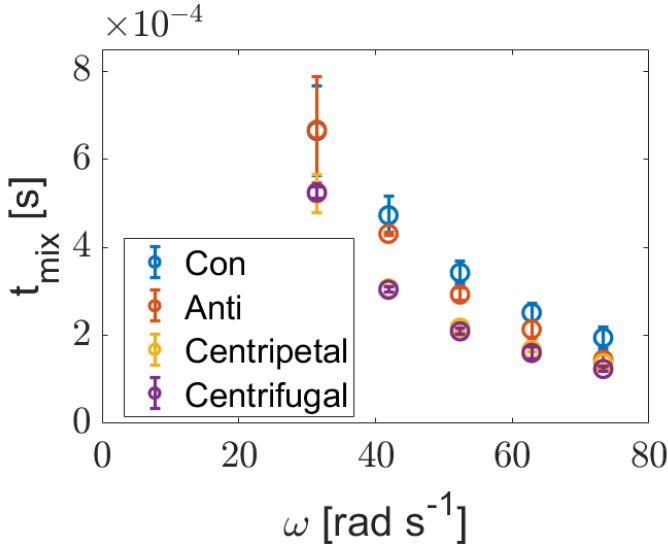

Figure 5.5: Micromixing time as function of rotational rates for different injection directions at $Z = 0.8$. The error bars denote the standard deviation between two experiments and the flow directions are as follows: con is directed with the flow, anti is directed against the flow, Centripetal is directed inwards and Centrifugal is directed outwards.

In Figure 5.5 the micromixing time as a function of the rotational rate is depicted at a dimensionless axial position of $Z = 0.8$. Since the fluid flows with a spiraling motion in the centripetal direction [18, 19, 106], four possible injection directions could be created with this configuration, with the flow direction (con), against the flow direction (anti), perpendicular

to the flow in the centripetal direction and perpendicular to the flow in the centrifugal direction (see Figure 5.4). As can be seen in the figure, the injection directions of centrifugal and centripetal resulted in lower micromixing times, and the smallest standard deviation (error bars). The injections parallel to the flow (anti and con) resulted in higher micromixing times (worse mixing). From Figure 5.5 it could also be seen that with increasing rotational rate, the micromixing times of the injection against the flow becomes similar to the perpendicular injection. In the remainder of the micromixing experiments, the acid was injected in the centripetal direction.

By injecting the acid in the centripetal direction at different axial positions between the rotor and stator, the axial dependency on the micromixing times was investigated. The results for three different rotational rates are depicted in Figure 5.6. It can be concluded that with increasing rotational rate the micromixing time decreases. Another observation is that the mixing intensity is generally the highest at the rotor (Z = 0.02) and the lowest near the stator (Z = 0.90). Additionally, there is a local peak in mixing time after the Von Kármán layer (0 < Z < 0.05) and a local dip before the Bödewadt layer (1 < Z < 0.91), these values were determined by Equation 5.5. However, due to the size of the rs-SDR and a highly dilutes system, the accuracy of the measurements decreases. This is also observed by the error bars (ranging from 5.5 to 20 %).
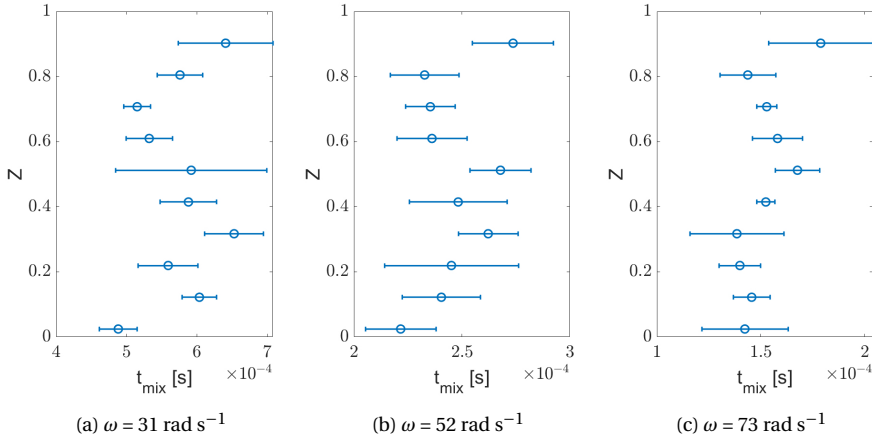

Figure 5.6: Micromixing times (t_{mix}) as function of the dimensionless axial distance (Z) for 31, 52 and 73 rad s^{-1}. The error bars denote the standard deviation between at least two experiments.

Another interesting observation is difference between the maximum

and minimum mixing times per rotational rate. When comparing the lowest and highest mixing times, in Figure 5.6a the difference is approximately 26% and this reduces gradually with increasing rotational rate to 18% in Figure 5.6c. This means that the axial dependency is diminishing with increasing rotational rate, which is also shown in literature by Van Eeten et al. [44]. They showed that with Re_h approaching infinity, the thickness of the Von Kármán and Bödewadt layers approaches zero and only a uniform core is present, thus suggesting there would be no axial dependency on the micromixing times.

As shown earlier, the micromixing times are directly correlated to the local energy dissipation rate (Equation 5.1). Figure 5.7 depicts the micromixing time as function of the local energy dissipation rate, which was calculated with Supporting Information D.1. This figure contains the mixing time for every tested rotational rate at three different axial positions, $Z = 0.02$ (Von Kármán layer), 0.51 (inviscid core) and 0.90 (Bödewadt layer). Additionally, the figures also contains a least-squares fit made with the *fit* function in Matlab between ϵ_{loc} and t_{mix} ($t_{mix} \propto (v/\epsilon_{loc})^{1/2}$). The fit resulted in a $R^2 > 0.90$ and show that the experiments follow the trend proposed by Baldyga and Bourne [10].
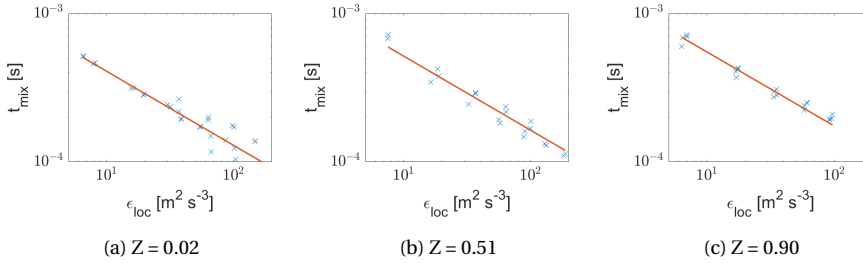

(a) Z = 0.02   (b) Z = 0.51   (c) Z = 0.90

Figure 5.7: Loglog plot of the micromixing times (t_{mix}) as function of the local energy dissipation rate (ϵ_{loc}) for Z = 0.02, 0.51 and 0.90. The plot contains all the tested rotational rates and the red line denotes the proportionality between t_{mix} and ϵ_{loc}: $t_{mix} \propto (v/\epsilon_{loc})^{1/2}$.

The values for the micromixing times are one order of magnitude smaller than suggested by the engulfment model (Equation 5.1) and therefore the equation is adapted by adding a proportionality factor (ϕ), see Equation 5.25. This results in a new constant, 1.53 ± 0.20.

$$t_{mix} = \frac{17.24}{\phi}\left(\frac{v}{\epsilon_{loc}}\right)^{1/2} = 1.53\left(\frac{v}{\epsilon_{loc}}\right)^{1/2} \tag{5.25}$$

The factor ϕ was determined during the fitting of the experimentally obtained micromixing times. The proportionality factor appeared to

depend on the axial position and not on the rotational rate. The values at the different axial positions are depicted in Figure 5.8 and the error bars are determined by the standard deviation based on the tested rotational rates with at least two repetitions. The results show that t_{mix} obtained with the experiments is approximately one order of magnitude lower than the engulfment model would predict [10]. However, Manzano et al. showed that the micromixing times in the rs-SDR, by injecting the acid directly in the Bödewadt layer (no injection probe), follow the engulfment model [30, 128, 142]. A reason for the deviation could therefore be the disturbance in the flow field due to the injection probe, especially with the influence of the injection direction (Figure 5.5). It is expected that the intensity in the turbulent wake of the probe enhances the local energy dissipation rate and as a consequence reducing the mixing time, this phenomena is also explained in literature [149] and in Supporting Information D.3 qualitative simulations were performed in *Solidworks* to verify this. The *Solidworks* simulations showed that the protrusion of the needle enhances turbulence around the injection point and therefore a reduction in the mixing time could be observed. Another interesting observation is when comparing the results with Figure 5.6, that ϕ follows the same trend and becomes larger at lower mixing times and vice versa.
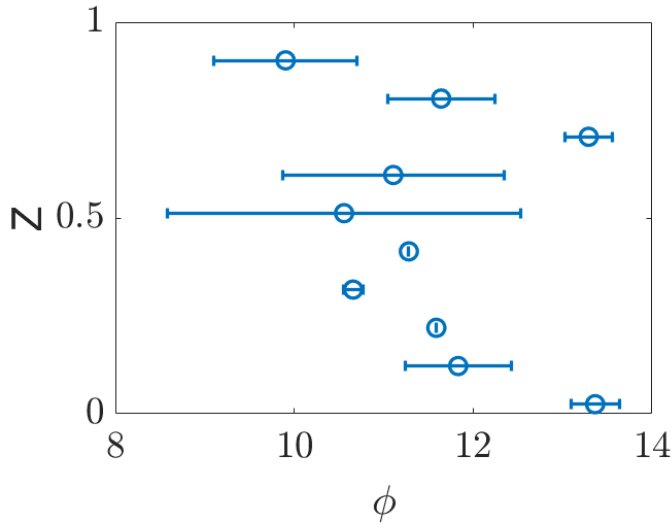

Figure 5.8: Proportionality constant as function of Z, the error bars denote the standard deviation based on the different rotational rates with at least two repetitions per experiment.

5.4.2. SIMULATION OF ROTOR-STATOR FLOW

During the computational work, the focus was on the comparison with the results obtained by Poncet et al. [41]. The work of Poncet contains both experimental and numerical (with RSM) results of a rotor-stator cavity and primarily consist out of the validation of the velocity profiles in combination with the Reynolds stress tensors. The dimensionless velocities $(U = u\,(r\omega)^{-1})$ are plotted at different dimensionless axial positions in Figure 5.9 and a comparison can be made between the LES with a WALE SGS model from OpenFOAM (this study) and the results from Poncet et al. [41]. The velocity profiles from LES were averaged over 0.5 revolutions and it is shown that the qualitative agreement is good, but quantitatively the results, especially at higher radial positions, deviate from the literate. One possible reason for this could be the entrainment coefficient, which is defined as the ratio between the tangential velocity in the core and the tangential velocity at the disc. In this study it was found that the entrainment coefficient at midradial positions is slightly underestimated, 0.39 in this study compared to 0.43 by Poncet et al. [41], and even more underestimated at 0.8 R_D. However, this coefficient matches at lower radial positions and therefore this coefficient could be a reason why the LES profiles deviate more at higher radial positions compared to the lower radial coordinates. Another possibility is the conservation of momentum, in this situation no flow rate is set, which means that the integral of the radial velocity over every axial position should be zero. The solution of the integral is determined via Matlabs *trapz* function. The LES resulted in a deviation lower than 0.01% and the results from Poncet et al. had a deviation smaller than 0.5% (both experimental and RSM). However, the experimental deviation at 0.8R_D from the conservation of momentum was 1.1% and this could therefore also be a possibility for the bigger deviation between LES and the experimental results.

Another characteristic that could be validated was the Reynolds stress, Poncet et al. was able to calculate these by using the time averaged velocity fluctuations and normalise them by dividing by the square of the local disc velocity [41]. The Reynolds stresses from the simulations in this study contains both the resolved and unresolved part of the Reynolds stresses. These were time-averaged and summed to obtain the total Reynolds stress tensor. From Figure 5.10, it can be seen that the results match qualitatively, but are quantitatively slightly off. Additionally, LES estimates the experimentally obtained values better than RSM at 0.44 R_D, equal at 0.56 R_D and worse at 0.8 R_D. This was also observed in Figure 5.9 and the possibility for the deviation remains the same, namely an under prediction
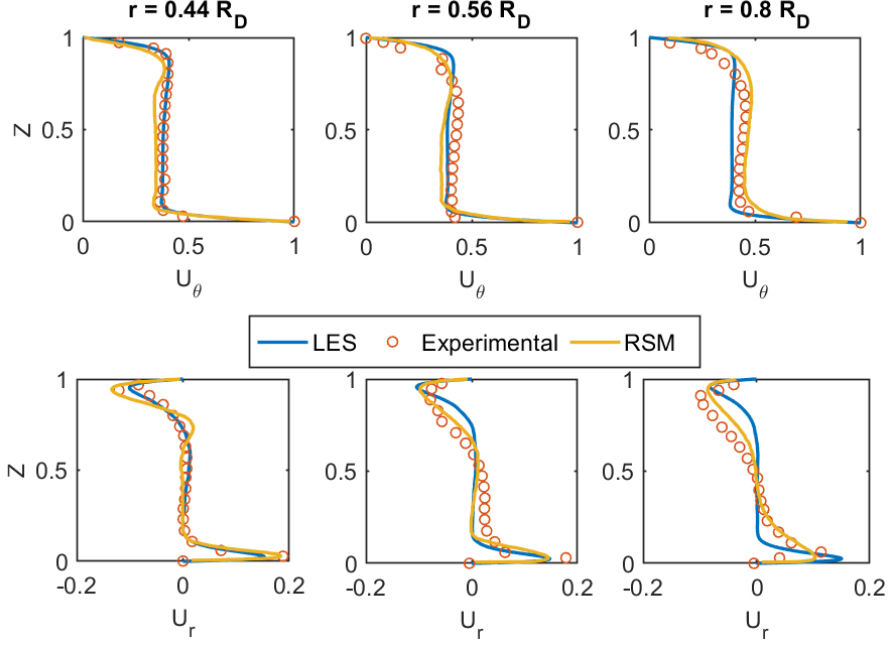
Figure 5.9: Comparison between the tangential/radial velocity as function of the dimensionless height (Z = z/h) obtained by LES (this study, blue line), the experimental results (red circles) generated by Poncet et al. [41] and the results generated by RSM (yellow line) [41]. The velocity is made dimensionless: $U = u (r\omega)^{-1}$.

by LES of the entrainment coefficient (K), see Supporting Information C.4 for the meaning of K, at higher radial positions and an experimental error from the momentum conservation at 0.8 R_D.

The micromixing time could be estimated with the engulfment model [10] and the energy dissipation rate. Since OpenFOAM does not directly calculate ϵ, the total energy dissipation rate (ϵ_{tot}) was calculated by combining the sub grid scale (ϵ_{SGS}) and the resolved (ϵ) energy dissipation rates. See Equations 5.26-5.28 [135], with ν_{eff} being the effective kinematic viscosity and $\mathbf{S_{ij}}$ the strain rate tensor.

$$\epsilon_{tot} = \epsilon_{SGS} + \epsilon \tag{5.26}$$

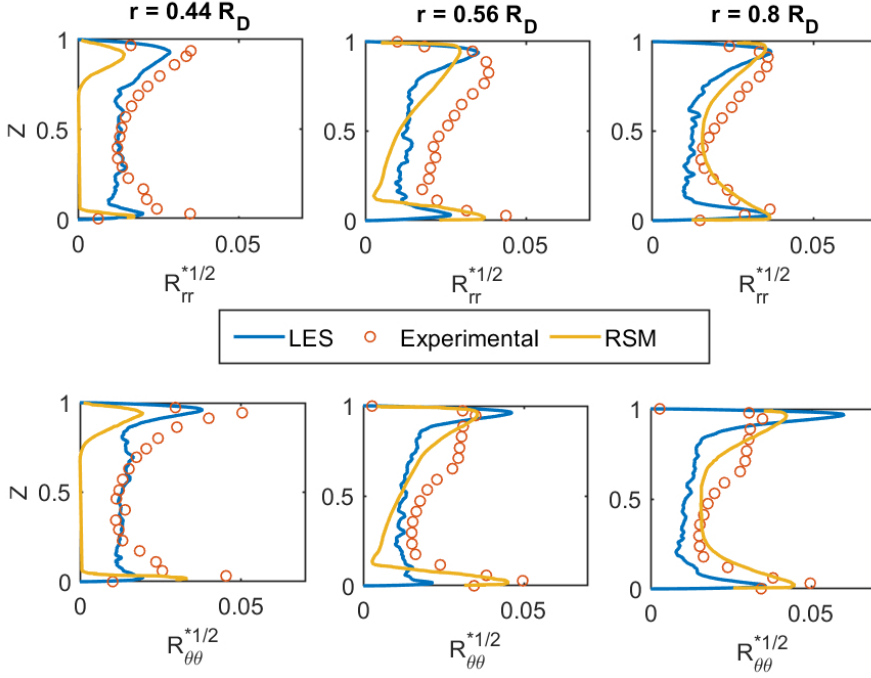$$\epsilon = 2\nu_{eff}\overline{\mathbf{S_{ij}S_{ij}}} \tag{5.27}$$

Figure 5.10: Comparison between the Reynolds stresses as function of the dimensionless height (Z = z/h) obtained by LES (this study, blue line), the experimental results (red circles) generated by Poncet et al. [41] and the results generated by RSM (yellow line) [41]. The Reynolds stresses were normalised by: $Re_{ii} = \overline{u_i'^2} \, (\omega \, r)^{-2}$.

$$S_{ij} = \frac{1}{2} \left(\frac{\partial u_i'}{\partial j} + \frac{\partial u_j'}{\partial i} \right) \tag{5.28}$$

The estimated micromixing times from OpenFOAM are determined with Equations 5.26 to 5.28 and could be compared with the experimentally obtained values. However, since the experimental results needed the proportionality factor to agree with the engulfment model, the experimental mixing times are multiplied with ϕ (see Equation 5.25). The comparison between the results from OpenFOAM and the experimental mixing time multiplied with ϕ is plotted in Figure 5.11, the experimental results are from the $\omega = 73$ rad s^{-1} experiment. Both mixing times are determined at the same radial position (0.9 R$_D$) and the Reynolds numbers are $1.0 \cdot 10^6$ for LES and $1.1 \cdot 10^6$ during the experimental results. The experimental error bars denote the maxima and minima when multiplying

the experimental t_{mix} with ϕ. From the figure it can be concluded that, even though the geometries are different, the majority of the results are within the experimental error for similar Reynolds numbers. The only deviation between the two results is in the boundary layers and is likely due to the differences in gap width, as this would lead to larger velocity gradients, hence larger fluctuations and as a consequence bigger differences in energy dissipation rate.
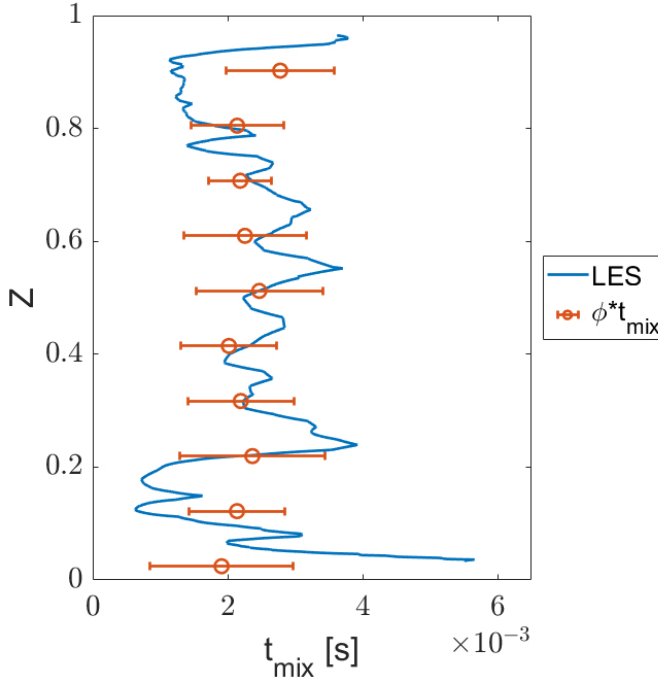

Figure 5.11: Micromixing times (t_{mix}) as function of the dimensionless axial distance (Z) for the experimental (Re = $1.1 \cdot 10^6$) and LES results (Re = $1.0 \cdot 10^6$), also the radial position (0.9 R_D) is equal for both results. The error bars denote the maxima and minima when multiplying the experimental t_{mix} with ϕ.

5.5. CONCLUSION

This work has investigated the effect of the turbulent boundary layers on the micromixing efficiency in a rs-SDR. The research was conducted by a combination of experimental work and numerical simulations in the form of LES with WALE in OpenFOAM 9. During the experimental work an axial dependency on the micromixing times was found by using the

Villermaux-Dushman reaction. The system was operated in the turbulent regime with separated boundary layers (Batchelor flow). It was concluded that the mixing intensity was the highest in the Von Kármán layer (at the rotor) and the lowest in the Bödewadt layer (at the stator). Additionally, it was observed that the injection probe influenced the micromixing time and that it could lead to the deviation from the micromixing times from the engulfment model. Also, the difference between the mixing intensity in the Von Kármán and Bödewadt layers decreases with increasing rotational Reynolds numbers and is in alignment with literature, when Re $\to \infty$ the turbulent boundary layers disappear. The numerical investigations on the mixing times were performed in the system from Poncet et al. [41] as they reported experimentally obtained velocity profiles along the rotor-stator distance. These results were used as a validation for the LES with WALE. This system was operated at similar Reynolds numbers, but had a gap width of 0.036 instead of 0.072. The obtained results in OpenFOAM were in agreement with the literature values for lower and mid radial positions, but were deviating at a radial position of $0.8 \cdot R_D$. The deviation could occur due to an underestimation of the entrainment coefficient or to the experimental deviation from the momentum conservation. The same conclusion holds for the Reynolds stresses that were compared. Lastly, the simulated micromixing times were compared with the experimental times and it was found that the inviscid core was within the experimental error, but in the boundary layers t_{mix} was slightly off. This mismatch is likely due to the difference in gap width, since this could lead to a change in velocity gradients and therefore also in dissipation rates. Overall, these results show the effect of the turbulent boundary layers and with this knowledge the selectivity of a competitive and/or parallel reaction could be improved in the rs-SDR. Additionally, the results of the simulations could be used to evaluate velocity gradients, shear effects and turbulent intensity. These properties are generally hard to measure, but determine for many competitive and/or parallel reactions the yield and eventually could increase the sustainability of a process.

CHAPTER 6

FERMENTATION IN A ROTOR-STATOR SPINNING DISC
REACTOR
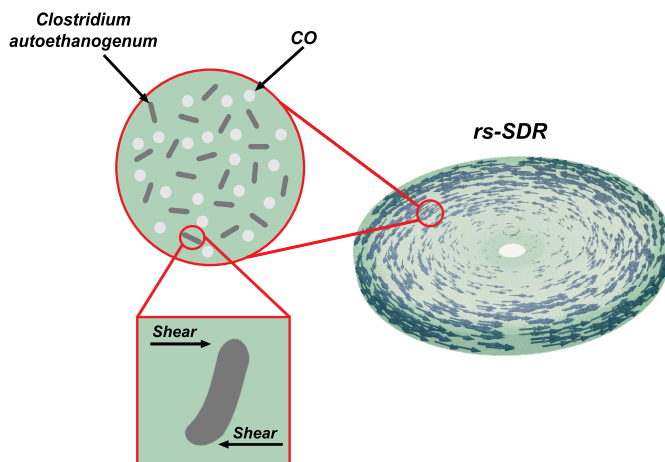
Abstract

During this study, an intensified reactor, the rotor-stator Spinning Disc Reactor (rs-SDR), with high mass transfer rates was tested for fermentation applications. This reactor applies high velocity gradients between a small rotor-stator gap and as a result, high shear forces arise that enhances turbulence and mass transfer rates. This study focuses on the shear effects on Clostridium autoethanogenum to improve CO fermentation. The experiments were conducted at 100, 500, 1000 and 1500 rpm and product formation, cell density and cell size were monitored. It was found that the rs-SDR had a negative influence on the fermentation, since no product formation or cell growth was observed. However, no changes in cell morphology and size were observed after analysing microscopic images. Additionally, numerical simulations were performed in OpenFOAM 8. A Couette flow that mimics the turbulent field of the rs-SDR was constructed and a single cell was inserted and exposed to the shear forces. From these results, there should be no cell damage and therefore it is most likely that the cells become inactive due to a combination of shear stress and CO poisoning. To implement the rs-SDR, increasing the cell density could work, as it would decrease the amount of CO per cell and reduce the turbulence intensity.

6.1. INTRODUCTION

Currently, the focus of many researches is to find techniques that optimise processes, reduces emissions, reduces resource utilisation or increase the efficiency of energy utilisation in order to reduce the emission of greenhouse gases to net-zero by 2050 [81]. An upcoming sustainable process is the gasification of biomass into syngas (mixture of CO_2, CO and H_2). The syngas can then converted towards fuels or feedstock for multiple industries such as, chemical, food, pharmacy, etc. [55]. Currently, the conversion into valuable products often happens with metal-based catalytic processes and these typically require high temperatures and pressures to perform the process, such as the production of propylene glycol or the hydrogenation towards methanol [58]. However, these processes are sensitive to catalyst poisoning by molecules that contain elements such as, sulfur or phosphor [84].

Therefore, over the past years, alternatives for syngas conversion are investigated, amongst others microbial syngas fermentation. The benefit of fermentation is that, multiple bacterial strains are suitable for the conversion of syngas into valuable products. Also, fermentation processes are generally performed at lower temperature (30-40 °C), lower pressures and with higher selectivities compared to metal-based processes [63, 64]. An example of such organism is *Clostridium autoethanogenum* and it is able to convert syngas into acetic acid, ethanol and butane-2,3-diol via the Wood-Ljungdahl pathway [61, 62].

Common reactors in which fermentation takes place are stirred tank reactors and bubble columns [86]. However, these reactor systems tend to be mass transfer limited and as a consequence, cell growth and productivity are limited by the amount of dissolved gas. To obtain large scale productivity, high reactor volumes are required [68, 80]. In order to increase the productivity of these processes, the gas to liquid mass transfer rate needs to be enhanced.

Previously, research has been conducted on increasing the mass transfer rates for *C. autoethanogenum* by changing the agitation speed in a stirred vessel [80], by adding an internal liquid recycling loop to a bubble column [77] or by increasing the pressure to increase the driving forces between the gas an liquid phase, see Chapter 2. Additionally, different pH environments were tested to activate different enzymes in the metabolism [62, 76] and with that increasing the ethanol concentration.

Another potential concept is the rotor-stator spinning disc reactor (rs-SDR) [14], see Figure 6.1 for schematic representation of this rs-SDR. This novel reactor contains a rotating disc (rotor) that is surrounded

6

by a stagnant casing (stator) and the distance between the rotor and stator is generally a few mm. Due to this small spacing and the high rotational rates of the rotor, a highly turbulent field arises and this leads to high shear forces. The shear forces then result in high mass transfer rates in multiphase systems, such as gas-liquid flows [16, 107, 108], liquid-liquid [18–20, 24] and liquid-solid [22, 23] systems. As an addition, this system has also shown potential based on heat transfer [25, 26] and mixing applications [29, 30, 143]. However, the high shear rates and high gas-liquid mass transfer rates could be too much for the organisms, since cell damage. Moreover, CO poisoning could occur [75, 94], as was also shown in Chapter 2.
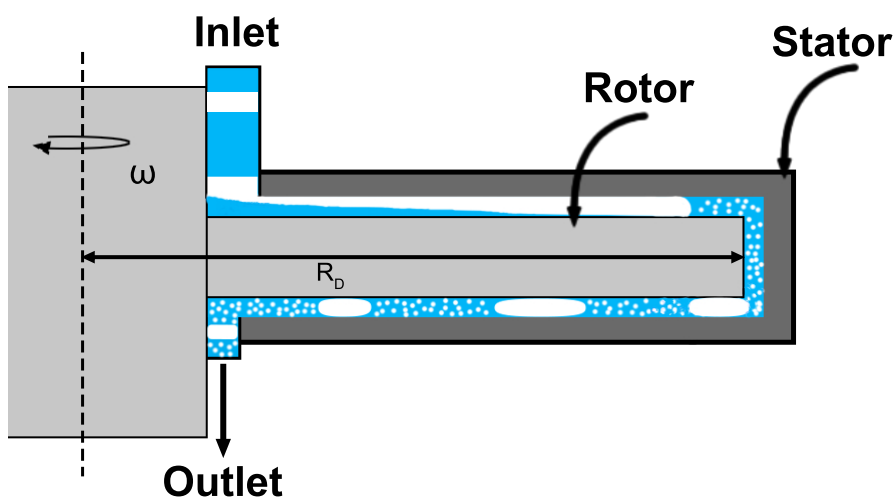

Figure 6.1: Schematic representation of the rs-SDR with gas-liquid flow.

Therefore it is important to investigate multiple aspects of the rs-SDR and find the optimal operation range for syngas fermentation with *C. autoethanogenum*. First, determine in which operational regime the reactor will be operated since the rs-SDR has four distinguished hydrodynamic regimes: [37]

- Regime I: laminar flow with merged boundaries

- Regime II: laminar flow with separated boundaries

- Regime III: turbulent flow with merged boundaries

- Regime IV: turbulent flow with separated boundaries

These regimes are dependent on two dimensionless numbers, the rotational Reynolds number ($Re = \omega R_D^2 \nu^{-1}$), which depends on the rotor radius (R_D) and the rotational rate (ω), and the dimensionless rotor-stator gap ratio ($G = hR_D^{-1}$) with h the rotor-stator spacing. These regimes were later on mapped in a graph (Figure 6.2) by Launder et al. [38]. During this study, the Reynolds number will be varied and the experimental operations are depicted with the green dots and numerical studies with the yellow dots.
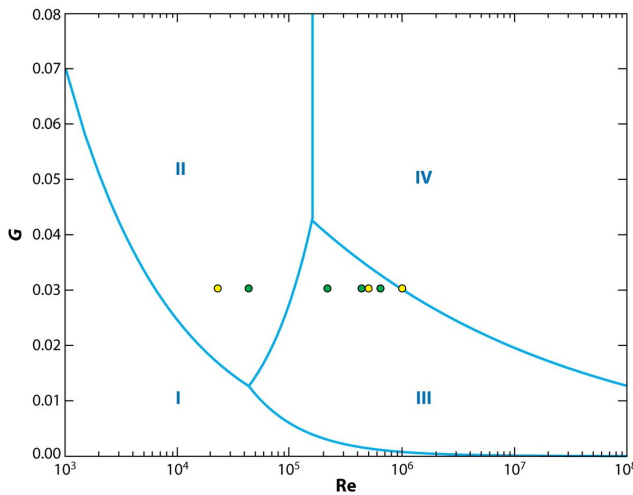

Figure 6.2: The flow regimes in the rs-SDR according to Daily and Nece and Launder et al. [37, 38]. The green dots denote the experimentally tested rotations and the yellow dots are the simulated Couette flows.

Previously it was shown that the rs-SDR can be simulated completely in OpenFOAM by using Large Eddy Simulations (LES) [143], however for multiphase flow this would be too computationally expensive. Also, simulations were also performed with a single rotor-stator cavity and it appeared less computationally expensive [39, 42]. However, to perform detailed analyses on a microbial cell is still too expensive with the current computational power. Nevertheless, Couette flows show similar hydrodynamic behaviour as the rs-SDR and have a much smaller computational domain, hence less computational time needed.

This study will focus on the implementation of the rs-SDR for COfermentation. The high mass transfer rates could overcome the current limitations and increase the cell growth and productivity of

C. autoethanogenum with CO as a substrate. Additionally, the size distribution and morphology will be studied to verify if the shear affects the cells physically. Lastly, a numerical study on the cell deformation was performed in OpenFOAM 8 in a turbulent Couette flow. Overall, the work will discuss the performance of *C. autoethanogenum* in the rs-SDR.

6.2. METHOD SECTION

To perform CO fermentation with *C. autoethanogenum* in the rs-SDR, the microbes were first cultivated in cultivation bottles. When a certain cell density was reached the culture was transferred via syringes into the rs-SDR set-up for the CO fermentation. In order to investigate the shear effects on the cells, a Couette flow that mimics the turbulent structures of the rs-SDR was developed in OpenFOAM 8. In this steady state field, a single bacterial cell was initialised and the drag forces, torque, rotation and deformation were determined.

6.2.1. BACTERIAL STRAIN AND CULTIVATION

The organism used for this study was *Clostridium autoethanogenum* DSM 10061 and it was obtained from the DSMZ strain collection (Braunschweig, Germany). The cultivation happened at 37°C in cultivation bottles (575 mL) with 20 vol% liquid and the liquid medium contains (per liter): 0.4 g KH_2PO_4, 0.53 g $Na_2HPO_4 \cdot 2 H_2O$, 0.3 g NH_4Cl, 0.3 g NaCl, 0.1 g $MgCl_2 \cdot 6 H_2O$, 0.01 g $CaCl_2 \cdot 2 H_2O$ and 0.5 mg resazurin. Trace-elements were added to the medium (per liter of medium): 1.8 mg HCl, 0.062 mg H_3BO_3, 0.061 mg $MnCl_2$, 0.944 mg $FeCl_2$, 0.065 mg $CoCl_2$, 0.013 $NiCl_2$, 0.067 $ZnCl_2$, 0.013 mg$CuCl_2$, 0.4 mg NaOH, 0.0173 mg Na_2SeO_3, 0.0294 mg Na_2WO_4, 0.0205 mg Na_2MoO_4. The autoclaving procedure was done in a pressure cooker that could reach a total pressure of 2 bar(a) and 133 °C, this procedure took 1.5 hours. After the bottles had cooled down, 0.09 vol% of a vitamin mixture was added, containing per liter: 20 mg biotin, 200 mg nicotinamid, 100 mg p-aminobenzoic acid, 200 mg thiamin, 100 mg panthotenic acid, 500 mg pyridoxamine, 100 mg cyanocobalamine and 100 mg riboflavine. Additionally, 1 g yeast extract and 1 g tryptone per liter was added and as a buffer 3.88 g/L $NaHCO_3$ was added. Lastly, 0.5 mg L-cysteine HCl and 0.235 mg $Na_2S \cdot 9H_2O$ were added as O_2 reducing agents. In the background, 20 mM of acetate was added to speed up the initial growing process with CO headspace. The pH was set to 5.75 using NaOH or HCl and the O_2 was removed from the headspace by using a vacuumpump. When a vacuum was reached (± 0.2 bar(a)), CO was added up to 1.8 bar(a) and this procedure was repeated 5 times to ensure an O_2 free environment. The

bottles were placed in a shaker at slow speed and constant temperature of 37 °C. The culture was maintained by refreshing the gas in the headspace, adding NaOH or HCl to keep the pH close to 5.75 and refreshing a part of the liquid (5-10%) with clean cultivation medium once in two weeks.

6.2.2. EXPERIMENTAL SET-UP

The experimental set-up consists out of a buffer vessel of 600 mL (V_B) and a rs-SDR with a radius of $6.6 \cdot 10^{-2}$ m (R_D) and G = 0.0303, see Figure 6.3. The buffer vessel is submerged in a waterbath and the water is heated by an IKA RCT Basic heating/stirring plate to maintain a temperature of ±36.5 °C. Within the buffer vessel a magnetic stirring rod is placed and rotates with 100 rpm. Before operation, the set-up is cleaned by circulating 20 vol% of H_2O_2 through the rs-SDR back into the buffer vessel for 10 minutes. After this, the H_2O_2 is removed and the system is rinsed three times with dH_2O to remove the remaining H_2O_2. All liquid is completely removed and the system is flushed overnight with N_2 to create an O_2 free environment. Lastly, the CO is added to the system and the N_2 is removed. The pressure of the system is set to 1.2 bar(a) and 230-250 mL of culture was transferred from the cultivation bottles into the buffer vessel.
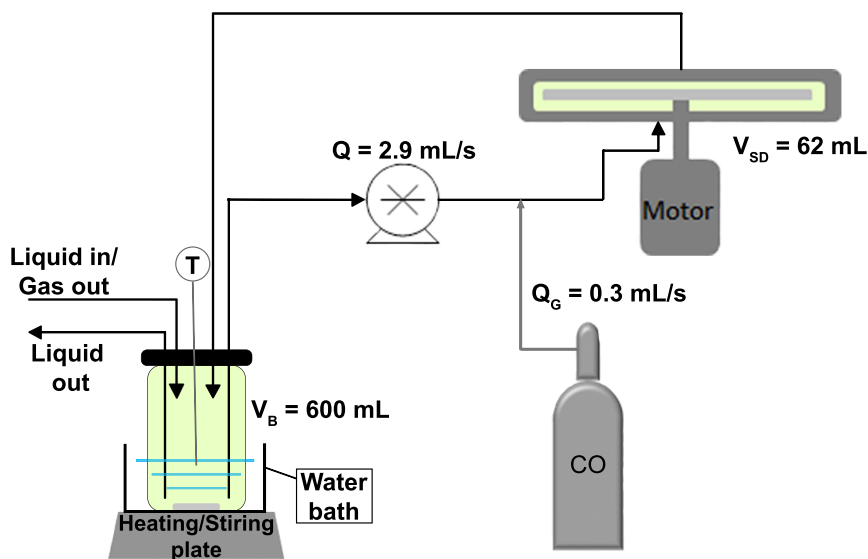

Figure 6.3: Schematic representation of the rs-SDR fermentation set-up.

During the experiment the liquid is pumped out of the buffer vessel via

a Cole Parmer Masterflex L/S peristaltic pump with an flow rate of 2.9 mL s^{-1} and 0.25 m before entering the rs-SDR the CO gas flow is fed with 0.3 mL s^{-1} via a T-junction into the liquid stream. The gas/liquid mixtures enters the rs-SDR via the bottom and flows through the rs-SDR back into the buffer vessel. Via a syringe and a hand valve, liquid samples can be taken for pH, product and bacterial analyses. This line is also used to inject 1 M HCl and 3 M NaOH to adjust the pH (5.2-5.8). The experiments were performed at 100, 500, 1000 and 1500 rpm, representing rotational Reynolds numbers of 4.6·10^4, 2.3·10^5, 4.6·10^5 and 6.8·10^5 respectively (Figure 6.2).

6.2.3. EXPERIMENTAL ANALYSIS

The concentration of acetic acid and ethanol was analysed in a high pressure liquid chromatography (HPLC) by Shimadzu of the type UFLC XR containing a LC-20AD pump, SIL-20A sampler and CTO-20AC oven, equipped with a Shimadzu Shim-pack GIST C:18 column. The measurements were performed using a Waters 2414 refractive index detector. The flow of the eluent (0.01 M H_3PO_4) was 0.5 mL min^{-1} and the column was operated at a temperature of 60 °C and 5 μL of sample was injected during every measurement. Butane-2,3-diol was analysed on a Gas Chromatography Mass Spectrometry (GCMS) by Shimadzu (GCMS QP2010) equipped with an Agilent J&W DB-200 column (length: 30m, diameter: 0.25mm, film thickness: 0.50 μm). The column was operated at 50 °C at 65.7 kPa and He was used as a carrier gas.

The cell density was obtained from a UV-2501PC UV-VIS, the optical density (OD) was measured at 600 nm. The cuvettes had a path length of 10 mm and the conversion from OD to cell dry weight was assumed to be equal to the correlation from Supporting Information A.2, see Equation 6.1.

$$X = 0.0145 + \frac{OD}{3.9346} \tag{6.1}$$

To investigate possible morphology the cells were visually analysed under a Zeiss observer.D1m microscope. The magnification of the lens was 100 times and the camera 0.67, resulting in a total image magnification of 67 times. The samples were prepared by placing one droplet in between two glass slides and the focus was manually adjusted. The image analysis was performed in Matlab, where a contrast was applied with the *imbinarize* function. All cells that were cut by the image boundary (*imclearborder*) and with less pixels than a given treshold (*bwareaopen*) were removed. Additionally, the cells were identified with the *bwboundaries* function and the area of each cell was determined with the *regionprops* function and

converted into a histogram.

6.2.4. NUMERICAL APPROACH

To study the shear and turbulent effects of the rs-SDR on the organisms, a single bacterial cell is placed in a Couette flow. Simulating a single cell in the complete rs-SDR flow field would require too much computational power and therefore a Couette flow with similar hydrodynamic behaviour was chosen [37]. The Couette flow was simulated with a stationary bottom wall (stator) and with the top wall moving in the x-direction (rotor) to resemble the flow in the rs-SDR. Due to limited literature, the modeling techniques for deformation on the organisms was adapted from red blood cells [150–152]. The simulations were performed with the Volume of Fluids (VoF) methods in OpenFOAM 8 [153] and the validation of the flowfield with a similar implementation is presented in Supporting Information E.3. The simulated Reynolds numbers are, 21333, $5 \cdot 10^5$ and $1 \cdot 10^6$.

The numerical schemes that were used are presented in Table 6.1 and are the standard schemes for most cases. However, for the discretisation of the divergence term, different schemes were used per term to increase the numerical stability *Gauss limitedLinearV 1* and accuracy at the interface with the velocity-weighted Multicut Piecewise Linear Interface Calculation (*MPLICU*). The latter is especially more accurate at high shear flows, since it uses the velocities at the interface to compute the face flux [153]. Also, this scheme is more precise for meshes with refinement regions. The time discretisation was a complete Crank-Nicolson scheme and the Smagorinsky-Lilly sub-grid-scale turbulence model [154, 155] was selected.

Mathematical term	Interpolation scheme
Gradient	Gauss linear
Divergence (default)	Gauss linear
div($\rho \cdot \phi, \boldsymbol{U}$)	Gauss limitedLinearV 1
div(ϕ, α)	MPLICU
Laplacian	Gauss linear corrected
Interpolation	Linear
Surface-normal gradient	Corrected

Table 6.1: Discretisation schemes that were used in the simulations of a bacterial cell.

The pressure solvers were selected to be a Preconditioned Conjugate Gradient (PCG) with a Diagonal-based Incomplete Cholesky (DIC) smoother. The hydrostatic pressure was solved with a Geometric

Aglomerated Algebraic Multigrid (GAMG) solver in combination with the DIC smoother. The remaining fields were solved with a *smoothSolver* and a *symmGaussSeidel* smoother. The volume fraction was solved with an interface compression coefficient of 1. The pressure-velocity coupling was done with the PIMPLE algorithm, which is a combination of a Semi-Implicit Method for Pressure Linked Equations (SIMPLE) and the Pressure Implicit Splitting Operator (PISO). This algorthm first solves the velocity equations by using the fields obtained from the previous time step, also known as the momentum predictor. The velocity and pressure are corrected several times to satisfy mass conservation [136]. The PIMPLE algorithm in this study contains two correctors and four non-orthogonal corrector steps.

The mesh was generated with the *blockMesh* utility and was $2 \cdot 10^{-4}$, $1 \cdot 10^{-3}$ and $1 \cdot 10^{-3}$ m in the x, y and z direction respectively. The base mesh was generated with 20x100x100 (x, y, z) gridpoints and was equal for all tested Reynolds numbers. Within the domain, a moving mesh was introduced to reduce the maximum Courant Friedrichs Lewy (CFL) number and it moves with half the wall velocity. To model the flow on a bacterial scale, a box with a decreasing cell size around the cell location was introduced. The box was refined in 10 steps, with every step bisection the cells in each direction and resulting in a total of $1.3 \cdot 10^{6}$ cells in the Couette flow domain. The mesh quality was checked with the *checkMesh* utility and it resulted in an avarage non-orthogonality of 6°, with a maximum of 68°and a maximum aspect ratio of 38. The boundary conditions and initialisation were equal to the Pirozoli et al. (Supporting Information E.3) [156]. As an addition, the bacterial cell was initialised with the *funkySetFields* utility and the volume fraction of the organism was set to unity, more information about the cell initialisation can be found in Supporting Information E.4.

6.2.5. CELL INITIALISATION

In literature, the organism *Clostridium autoethanogenum* is identified as a gram-positive rod-shaped cell (confirmed by the microscopic images in Supporting Information E.2) that metabolises C1 components [62, 157]. It was found that the cell diameter distribution ranges from 0.5 to 0.6 μm, with an average of 0.5 μm. The buoyant density was found to be between 1.09 and 1.13 g cm^{-3} [158]. The contact angle and the bacterial surface tension was investigated of filtered cells of *Clostridium carboxidivorans* [159]. The surface tension was 56 mJ m^{-2}, with a contact angle of 33°. Since *C. autoethanogenum* has a similar morphology and

cell structure, it was assumed that the *C. carboxidivorans* values could also be applied for *C. autoethanogenum*. The cells are gram-positive and therefore peptidoglycan was assumed to be the main component in the cell wall [160]. The mechanical properties of peptidoglycan is studied by stress-strain experiments to determine the viscoelastic properties, which can be translated into the viscoelastic properties of the cell wall. It was found that the yield stress was highly dependent on the relative humidity and when completely wetted it results in a tensile strength of 3 MPa [161, 162]. The stress-strain curves resembles also other viscoelastic polymers and when a according to literature the viscosity was 20 MPa·h [163].

In order to capture this viscoelastic behaviour, the Herschel-Bulkey model [164] was implemented in OpenFOAM. This model describes fluids that behave as rigid solids with high viscosity at shear stresses that are lower than the yield stress, but starts to behave as a non-linear viscous fluid when the shear stress exceeds the yield stress [165]. The implementation in OpenFOAM is given by Equation 6.2, with ν_0 the kinematic viscosity at low shear rates, τ_0 the density normalised yield stress and k_{HB} the consistency coefficient. To represent Newtonian behavior the order of the equation (n_{HB}) was set to unity.

$$\nu = \min(\nu_0, \frac{\tau_0}{\dot{\gamma}} + k_{HB}\dot{\gamma}^{n_{HB}-1}) \qquad (6.2)$$

Since two phases are present in this simulation, the *multiphaseInter-Foam* solver from OpenFOAM was used. The surface tension between the two phases was set to 0.0056 N m^{-1}. The drag force can be described by Equation 6.3, where subscripts *c* and *d* denote the continuous and dispersed phase. C_D is the drag coefficient and comes from the Schiller-Neumann correlation [166]. The force related to the surface tension can be expressed using the continuum surface force model [167]. However, this correlation is only valid for spheres and therefore the results should be studied with this in mind. The virtual mass is taken into account with the *constantCoefficient* model in OpenFOAM. Also, the gravity is included in the simulation.

$$\boldsymbol{F}_{D,k} = \frac{3}{4}\rho_c\alpha_c\alpha_d C_D \frac{|\boldsymbol{u}_d - \boldsymbol{u}_c|(\boldsymbol{u}_d - \boldsymbol{u}_c)}{d_d} \qquad (6.3)$$

During the simulation, the solver was executed in parallel using *mpirun* on 4 cores with the *scotch* method. The time step was manually adjusted to maintain the CFL number between 0.2 and 0.3. It was observed that the CFL number for the interface compression was not limiting in all cases and the total simulation time was 0.2 eddy turnover times ($t_{eddy} = $ h u_{wall}^{-1}).

6.3. RESULTS AND DISCUSSION

This section will discuss the results of CO fermentation with *C. autoethano-genum* in the rs-SDR and how the high shear forces affect the cell morphology (size and shape). Additionally, a single cell is simulated in a Couette flow that mimics the hydrodynamics of the rs-SDR in OpenFOAM 8. The simulations were used to determine whether the cell wall would theoretically break.

6.3.1. PERFORMANCE IN RS-SDR

The experiments were performed at 100, 500, 1000 and 1500 rpm in the rs-SDR with a constant CO gas throughflow and when a sample was taken, the same amount was refilled to maintain a constant liquid volume (D = 0.032 day^{-1}). Only the results of the 100 rpm experiment were presented in this section (Figure 6.4) and the remaining rotational rates are shown in Supporting Information E.1. Figure 6.4 depicts the 100 rpm experiment in the rs-SDR and both the biomass and product concentrations are presented. From this figure it can be seen that the biomass concentration is decaying at a low rate and this could indicate that the microbes are experiencing unwanted shear forces that are resulting in an increased death rate. Especially since the same microbes were growing from 0.01 g$_{CDW}$/L to 0.18 g$_{CDW}$/L in cultivation bottles within 100 hours. The same behavior was also observed for the higher rotational rates, 500 rpm: 10% decrease, 1000 rpm: 65% decrease and 1500 rpm: 20% decrease in less than half of the time. Therefore it can be concluded that the rs-SDR has a negative effect on the growth. Additionally, the product concentration remains constant during the fermentation and this also validates that no activity is taking place by the cells. The same observations also hold for the higher rotational rates in Supporting Information E.1.

6.3.2. CELL CHARACTERISATION

The cells were visually inspected with a microscope and analysed in Matlab to determine the area of a single cell, the images can be found in Supporting Information E.2. Histograms were made in order to create an area size distribution of the cells, see Figure 6.5. Every distribution is made out of two images and the images were taken at t = 0 hours and at the end of an experiment. All histograms are normalised with the amount of cells present at that specific image and all cells with an area smaller than 5 pixels were neglected. It can be observed that the cell surface remains constant during an experiment. This holds for all the tested rotational rates. Also, no difference is observed in size distributions between the different rotational
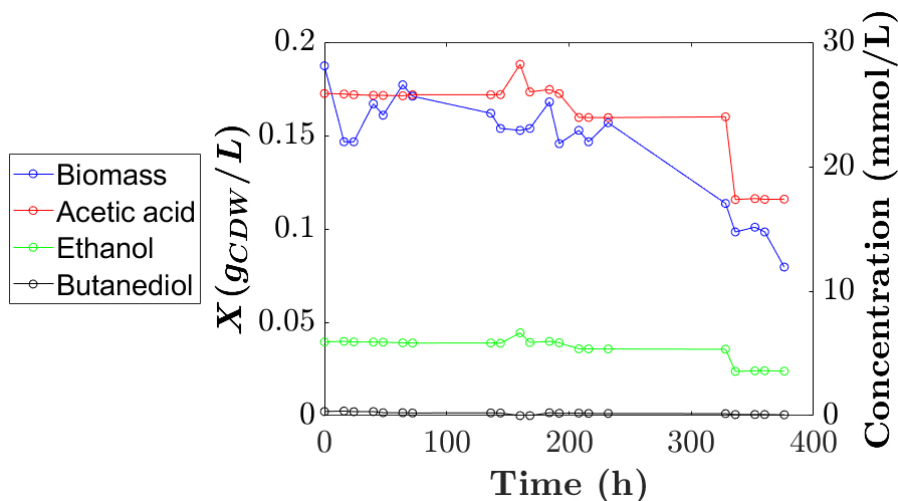
Figure 6.4: 100 rpm experiment, with the biomass concentration on the left y-axis and the product concentrations on the right y-axis and the time in hours on the x-axis.

rates. Overall, little change in cell morphology and area size have been observed under the microscope.

6.3.3. NUMERICAL ANALYSES

This section will discuss the Couette flowfield and the hydrodynamic effects on a single cell. During the remainder of this section, the x direction will be noted as streamwise, y the wall-normal and z the spanwise direction.

The results of the Couette flowfield are presented in Figure 6.6. It can be seen that at the higher Reynolds simulations, larger oscillatory behaviour in the spanwise direction was observed, compared to the low Reynolds number simulation. This could be related to large-scale motions that form in the channel core. Pirozolli et al. [156] studied a two-point correlation function of the streamwise velocity in the spanwise direction and found results demonstrating the sinusoidal behaviour, as was also observed in Figure 6.6.

During the simulations, the cells were initialised in three different orientations, spanwise, streamwise and wall-normal to study the effects of the different bacterium dynamics. It was observed that the drag force was the dominating force at every orientation and Reynolds number. Therefore, the drag forces are presented in Figure 6.7a and it can be concluded that the forces in the wall-normal direction are the largest. The lowest forces are in the streamwise direction. These results were expected since the
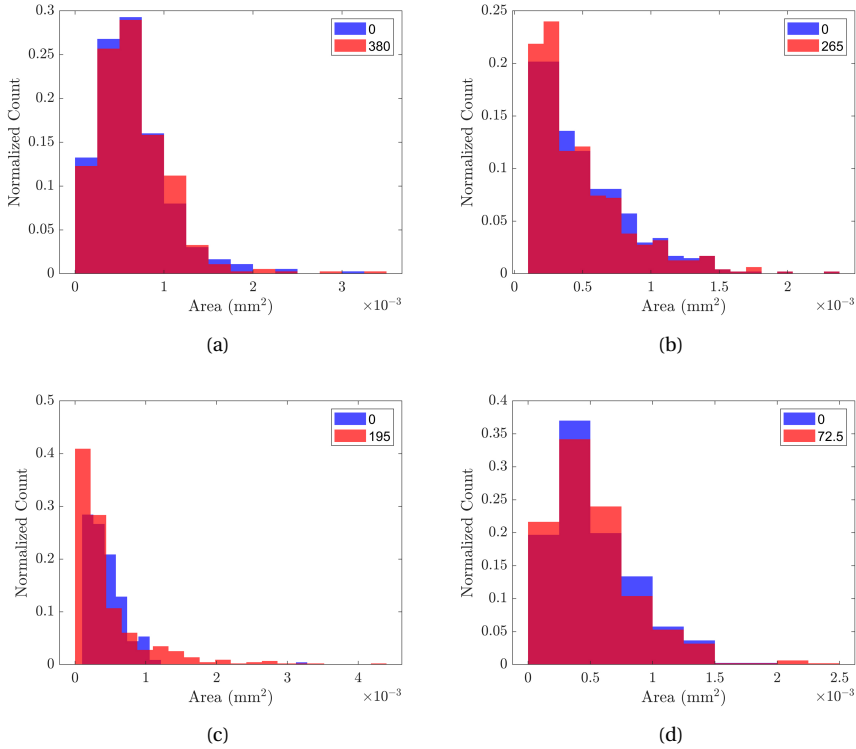
Figure 6.5: The cell area distribution at the start (blue) and the end (red) of an experiment in the rs-SDR with, (a) 100 rpm, (b) 500 rpm, (c) 1000 rpm and (d) 1500 rpm. The legend denotes the time in hours.

area parallel to the flow experiences the biggest drag force. Also, the forces increase with increasing Reynolds numbers and the increase in the streamwise direction is especially big between Re = 21333 and $5 \cdot 10^5$. This is most likely due to the transition from laminar to turbulent flow (Figure 6.2), as the chaotic nature of turbulent flows result in 3-D velocity fluctuations. Therefore, not only the tip of the cell observes a velocity, but also the sides. Visualisations made of the cells in *Paraview* are presented in Supporting Information E.4 and it was observed that rotation of the organism in 0.2 eddy turnover time only occurred in the wall-normal direction.

The rotation caused by the forces was calculated by the torque and depicted in Figure 6.7b. The first interesting observation that could be made is that the spanwise torque is the largest for laminar flow, especially since the drag force was the highest for the wall-normal orientation. This is most likely due to the moment of inertia, since the radius of rotation is
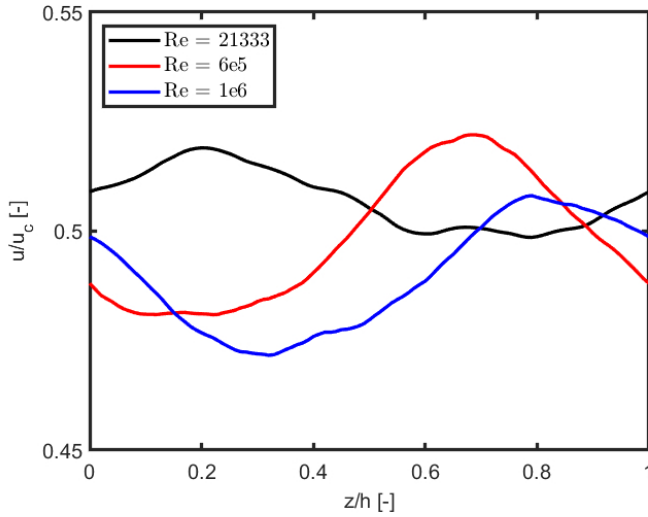
Figure 6.6: Spanwise velocity profiles of the streamwise velocity for the three tested Reynolds numbers at the center of the domain, showing large scale fluctuations that the cell theoretically would encounter during the simulations.
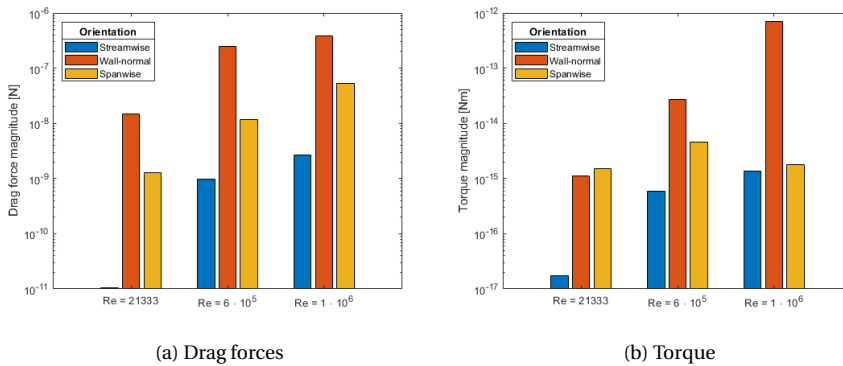

(a) Drag forces

(b) Torque

Figure 6.7: The magnitude of the drag force and torque on a single organism for the different orientations and different Reynolds numbers. The blue bars denote the streamwise direction, red the wall-normal and yellow the spanwise direction.

the smallest for the spanwise orientation and therefore a higher angular acceleration is observed. Also, the small changes in torque at different Reynolds numbers confirm this. Additionally, the torque follows the same trend as the drag force, increase with increasing Reynolds numbers and the highest values for the wall-normal orientation. When the torque surpasses the viscous torque due to the drag force, the cell would start

rotating. The rotation occurs towards the wall-normal orientation, since the torque applied on the bacterial cell is much greater in this orientation. Simulations with intermediate orientations between the streamwise and wall-normal orientation confirmed this trend. Since the torque is much greater in this orientation, a large angular acceleration is imposed, causing the cell to reorient into the streamwise direction (lowest resistance of drag). This phenomena is referred to as tumbling motion [168] and will cause a probability distribution of cell orientations with a maximum in the streamwise orientation. This was also experimentally observed for elongated cylinders in shear flows [169].

Lastly, the stresses on the organisms could be determined from the forces and to study the possibility of plastic yielding, the Tresca criterion was applied [170]. This criterion predicts the failure of materials due to shear effects, which are present in the Couette flow (and rs-SDR). The Tresca criterion gives the relation between the shear yield strength and the tensile yield and it was found that the shear yield strength is half of the tensile strength [170]. When this criterion is applied, it appeared that only for Re = $1 \cdot 1^6$ the yield limit was surpassed by 25%, the lower Reynolds numbers remained below the yielding limit. Another criterion that was applied is the Von Mises criteria, which presumes that the yielding is observed when the total strain energy density surpasses a certain critical value [170]. For the Von Mises criterion, the same was observed as for the Tresca criterion. However, it was seen that the rs-SDR has lower shear rates than the Couette flow. The 50 rad s^{-1} situation from Chapter 4 has similar shear rates of a Couette flow with Re = 825. Therefore, a tumbling motion was simulated in a Couette flow of Re = 825 and it was found that the yield stress in the cell was not surpassed. But, according to Croughan et al. the cell death rate is dependent on the eddy size, which was not accounted for during the simulations [171]. Later it was shown that cells start decaying when the eddy size is 10 times lower than the cell size [172], however these are mammalian cells and not bacterial. Since the rs-SDR exerts a power input between 0.1 and 1.2 kW/kg, the cells should start decaying when their length is smaller than 50 to 100 μm. Since the average size is 3.2 μm, the cells could be inactive due to the effect of the eddies.

6.4. CONCLUSION

During this study CO fermentation was performed with *C. autoethano-genum* in a rotor-stator spinning disc reactor at 100, 500, 1000 and 1500 rpm. Additionally, a visual study to identify changes in cell morphology and cell size has been performed with a microscope in combination with

image analyses in Matlab. Lastly, CFD simulations of a single bacterial cell in a turbulent Couette flow were done to investigate the effects of shear on the cells.

From the experiments it appeared that the rs-SDR has a negative influence on the CO fermentation. During the experiments no growth was observed and the cell density decreased during all tested rotational rate. Additionally, there were no products formed, indicating that the microbes were inactive. Only, it is not clear if the microbes became inactive due to the high shear rates or to sudden exposure of large CO quantities (CO poisoning).

To further investigate the inactivity of the microbes, microscopic images were analysed in Matlab. The analyses was done to determine if there were changes in cell morphology and size during exposure to the rs-SDR. After exposure of multiple days where the cells were recirculating at least once every 1.5 minutes, no change in cell size distribution was observed for every tested rotational rate. Additionally, the microbes kept the same rod-shaped body after the exposure to the shear in the rs-SDR.

Lastly, a shear field was created in OpenFOAM by using a Couette flow in order to mimic the flow field in the rs-SDR. This simulation case was validated with results from literature and changed into an rs-SDR representative domain. The flow field was developed for Re = 21333, $5 \cdot 10^5$ and $1 \cdot 10^6$ and within these flow fields, a single bacterial cell with similar physical properties as *C. autoethanogenum* was initialised. The cell was exposed to intense shear forces and according to the Tresca and Von Mises critia, the cell would break at the highest tested Reynolds number. However, the shear forces in the Couette flow are higher than in the rs-SDR (Chapter 3 to 5) and when a rs-SDR representative shear field was introduced, theoretically the cell does not break. However, according to the eddy size analyses, the cells should start decaying.

When taking all the observations into account, it is likely that the cells are inactive/decaying due to the shear forces in combination with CO poisoning. Therefore, the rs-SDR seems to be not applicable for the conditions tested in this work. However, increasing the cell density or reducing the rs-SDR exposure time might be beneficial. If the rs-SDR could be used, it would overcome the gas to liquid mass transfer limitations and increase the productivity of the fermentation process. This would lead to a more sustainable production of bio-fuels and reduce the utilisation of fossil based resources.

CHAPTER 7

<div style="text-align: right">

CONCLUSION

</div>

7.1. CONCLUSIONS

The focus of this thesis was to intensify syngas fermentation by reducing the mass transfer limitations and close the gap with the current industrial ethanol production. Two potential applications were investigated, increasing the mass transfer rates by increasing the driving force (elevated pressures) and applying/characterizing an intensified reactor, the rotor-stator spinning disc reactor (rs-SDR). This section summarizes the obtained results during this research.

The increase in CO pressure was investigated in Chapter 2 for a fermentation process with *Clostridium autoethanogenum* in a continuous system. The system was operated at 2, 5 and 10 bar(a) CO pressure and 5, 10 and 20 mL/min of CO inflow. During this experiment successful fermentation took place for 3800 h and in total six different steady state operations were obtained. It was observed that the ethanol productivity increased proportional with increasing CO inflow, indicating a clear mass transfer limited system. This effect was also observed when the pressure increased from 2 to 5 bar(a). However, increasing the pressure from 5 to 10 bar(a), resulted in a decrease in productivity. Overall, the highest ethanol productivities were obtained at 20 mL/min in combination with 5 (0.27 g/L/h) and 10 (0.24 g/L/h) bar(a) of CO head space pressure. Therefore, it can be concluded that increasing the pressure improves the productivity, but that too much dissolved CO has a negative influence.

In order to enhance the ethanol productivity further, an intensified reactor was evaluated, namely the rs-SDR. Previously it was shown that the rs-SDR could reach high gas to liquid mass transfer rates and therefore Chapter 3 contains the characterisation on higher gas/liquid flow ratios (1, 3 and 9 $m_G^3 m_L^{-3}$) and viscous systems (1, 5, 10 and 25 mPa*s). During this investigation, it was observed that increasing the gas/liquid ratio resulted in higher transfer rates, but decreased with increasing viscosity. Also, with increasing power input an increase in mass transfer was observed. As a result, the highest obtained mass transfer rate was 14 $m_L^3 m_R^{-3} s^{-1}$ for a viscosity of 1 mPa*s and a gas/liquid ratio of 9. This value is ~ 60-100 times higher than observed in bubble columns and stirred tank reactors (common equipment for industrial syngas fermentation). Additionally, correlations for the laminar and turbulent were fitted from the experimental results with R^2 values of 0.93 and 0.95 respectively.

After determining the mass transfer rates, the macromixing behaviour of the rs-SDR was investigated in Chapter 4 by combining experimental and numerical results. During this investigation a new and more realistic reactor model, based on axial dispersion, was proposed and validated with residence time distribution experiments. These results were used to validate the numerical work performed in OpenFOAM by applying Large Eddy Simulations (LES) for a complete rs-SDR. It was observed that the simulations were in good agreement with the experimental results for turbulent flows. Additionally, the simulations were compared with correlations from literature and it was concluded that LES predicts the behaviour in a complete rs-SDR well for turbulent flows. Lastly, it was observed that the turbulent energy in the centripetal flow was about 10% higher than in the centrifugal flow and that the plug flow regime (PFR) was larger for centrifugal flow. Also, the most turbulent intense region was found to be at the rim of the rotor and in general a better understanding of the hydrodynamic behaviour in the rs-SDR was obtained.

The micromixing efficiency in the turbulent boundary layers was investigated in Chapter 5. Micromixing times were determined experimentally at different locations between the rotor and stator by using the Villermaux-Dushman reaction. It was concluded that the mixing intensity was the highest in the Von Kármán layer and the lowest in the Bödewadt layer. Also, it was observed that the mixing times deviated from the engulfment model due to disturbances in the flow field by the injection probe. Next to the experimental work, simulations of a rotor-stator cavity with LES in OpenFOAM were performed. The simulations were validated with literature data and from the obtained flow field, micromixing times

were determined. Lastly, the simulated micromixing times were compared with the experimental times and it was found that the inviscid core was within the experimental error, but in the boundary layers it was slightly off. This is likely due to the difference in geometry, since different velocity gradients are present, hence different turbulent intensity and therefore different mixing times. Still, the simulations in combination with the experimental work provided more knowledge about the micro mixing behaviour in the rs-SDR.

In Chapter 6, fermentation with CO was performed in the rs-SDR. From the experiments a negative influence on the microbes were observed, since no growth or product formation took place. However, by analysing microscopic picture, no change in cell size or morphology was observed. As a last test, a single bacterial cell was created in a turbulent flowfield in OpenFOAM and a force analyses was performed on the cell. The turbulent field mimics the flow field of the rs-SDR and according to the Tresca and Von Mises criteria, theoretically the cells should not break due to the effects of shear. However, according to a death rate analysis, the cells should start decaying since the cells are bigger than the eddies. Therefore, it is likely that the cells are still intact, but are inactive or death. As a result, no productivity or growth took place and the cells are affected too much by the high shear forces in combination with the high CO availability.

Overall, this thesis showed that the fermentation process can be optimised further by applying more pressure in the system. Additionally, a better understanding of the mass transfer and hydrodynamics of the rs-SDR was obtained by using experimental and numerical studies. However, when applying the rs-SDR to a fermentation process, no improvements were obtained for the tested conditions and therefore more studies are required for this particular application.

7.2. OUTLOOK

To contribute to the transition from fossil into sustainable resources, process intensification is a key aspect for the chemical industry. Important aspects of process intensification are the reduction of mass transfer limitations and the utilisation of renewable resources. This work investigated both aspects by applying CO fermentation with *Clostridium autoethanogenum* at elevated pressures and studying the hydrodynamics and mass transfer rates of an intensified reactor, the rotor-stator spinning disc reactor. Fermentation has great potential, since this process utilises relatively low amounts of energy due to the mild temperatures and pressures. The process also reaches high selectivities, is not affected by

poisonous compounds (e.g. sulfur or phosphor) and is able to convert gaseous emissions into valuable chemicals, such as ethanol. Additionally, the rs-SDR has proven to overcome mass and heat transfer limitations, hence enhancing the productivity for numerous applications.

The results obtained during this thesis provided two main conclusions, syngas fermentation can be improved by increasing the pressure of continuous reactors without damaging the organisms and possible tools were provided by means of computational fluid dynamics that perfectly describe the hydrodynamic behaviour of the turbulent flow field inside the rs-SDR. However, combining syngas fermentation and the rs-SDR did not provide the productivity that is required to compete with the industrial standard. Therefore, improvements in operational methods are needed, since the rs-SDR still has great potential due to its high mass transfer rates.

For future work, it is essential to obtain higher biomass concentrations before operating with the rs-SDR. This to decrease the amount of dissolved gas available per cell and reduce the risk of CO poisoning, but also the increase in viscosity would reduce the turbulent intensity. Therefore, the higher cell density reduces the two main reasons that caused the negative influence by the rs-SDR. Another improvement would be a dynamic approach. This approach is about dosing the gas inflow by giving a burst of gas when the gas is almost depleted and reducing the saturation levels, hence reducing the risk of CO poisoning.

In order to further intensify fermentation processes, more engineering on the cells is required. It means that the cells need to be modified in order to speed up the metabolism, being more resistant to shear and CO or to produce chemicals with a lower market share. This would lead to a stronger organism that can be used in the rs-SDR and become a modular plant. Especially with the rs-SDR being suitable for modular processes, hence localising production and improve the utilisation of sustainable resources.

lastly, this work delivered a strong foundation for the continuation of computational fluid dynamics on a rs-SDR. With the developed models already a good insights can be obtained on the turbulent behaviour, but is missing the integration of an energy balance, multiphase flows and the ability to simulate reactions. The integration of multiphase flows will be computationally very hard and advances in hardware are required. However, the integration of an energy balance and reaction kinetics could improve the estimations towards the best injection point or locate local heat spots. This would increase the efficient usage of substrates and lead to a more sustainable operation.

BIBLIOGRAPHY

(1) F. Meng, A. Wagner, A. B. Kremer, D. Kanazawa, J. J. Leung, P. Goult, M. Guan, S. Herrmann, E. Speelman, P. Sauter, S. Lingeswaran, M. M. Stuchtey, K. Hansen, E. Masanet, A. C. Serrenho, N. Ishii, Y. Kikuchi and J. M. Cullen, *Proceedings of the National Academy of Sciences*, 2023, **120**, e2218294120.

(2) J. R. Puthalpet, *The Daunting Climate Change: Science, Impacts, Adaptation & Mitigation Strategies, Policy Responses*, CRC Press, London, 2022, pp. 1–523.

(3) S. Bilgen, *Renewable and Sustainable Energy Reviews*, 2014, **38**, 890–902.

(4) A. I. Stankiewicz and J. A. Moulijn, *Chemical Engineering Progress*, 2000, **96**, 22–34.

(5) S. Sitter, Q. Chen and I. E. Grossmann, *Current Opinion in Chemical Engineering*, 2019, **25**, 87–94.

(6) F. J. Keil, *Reviews in Chemical Engineering*, 2018, **34**, 135–200.

(7) A. Pudi, A. P. Karcz, S. Keshavarz, V. Shadravan, M. P. Andersson and S. S. Mansouri, *Chemical Engineering and Processing - Process Intensification*, 2022, **174**, 108883.

(8) J. J. Heijnen and K. Riet van 't, *Chemical Engineering*, 1984, **28**.

(9) K. van't Riet and J. Tramper, *Basic Bioreactor Design*, CRC Press, New York, 1991.

(10) J. Baldyga and J. R. Bourne, *Chemical Engineering Communications*, 1984, **28**, 243–258.

115

(11) A. N. Kolmogorov, *Proceedings of the Royal Society of London. Series A: Mathematical and Physical Sciences*, 1991, **434**, 15–17.

(12) H. Tennekes and J. L. Lumley, *A First Course in Turbulence*, MIT Press, 2018.

(13) P. Davidson, *Turbulence*, Oxford University Press, 2015.

(14) J. Van Der Schaaf and J. C. Schouten, *Current Opinion in Chemical Engineering*, 2011, **1**, 84–88.

(15) F. Visscher, J. van der Schaaf, T. A. Nijhuis and J. C. Schouten, *Chemical Engineering Research and Design*, 2013, **91**, 1923–1940.

(16) F. Haseidl, J. Pottbäcker and O. Hinrichsen, *Chemical Engineering and Processing: Process Intensification*, 2016, **104**, 181–189.

(17) M. M. de Beer, J. T. Keurentjes, J. C. Schouten and J. van der Schaaf, *International Journal of Multiphase Flow*, 2016, **83**, 142–152.

(18) F. Visscher, J. van der Schaaf, M. H. de Croon and J. C. Schouten, *Chemical Engineering Journal*, 2012, **185-186**, 267–273.

(19) A. Chaudhuri, K. P. Kuijpers, R. B. Hendrix, P. Shivaprasad, J. A. Hacking, E. A. Emanuelsson, T. Noël and J. van der Schaaf, *Chemical Engineering Journal*, 2020, **400**, 125875.

(20) A. Chaudhuri, W. G. Backx, L. L. Moonen, C. W. Molenaar, W. Winkenweder, T. Ljungdahl and J. van der Schaaf, *Chemical Engineering Journal*, 2021, **416**, 128962.

(21) E. R. van Kouwen, W. Winkenwerder, Z. Brentzel, B. Joyce, T. Pagano, S. Jovic, G. Bargeman and J. van der Schaaf, *Chemical Engineering and Processing - Process Intensification*, 2021, **160**, 108303.

(22) A. Chaudhuri, E. B. Temelli, C. J. Hop, V. P. Sureshkumar and J. Van Der Schaaf, *Industrial and Engineering Chemistry Research*, 2022, **61**, 6831–6844.

(23) M. Meeuwse, S. Lempers, J. V. D. Schaaf and J. C. Schouten, *Industrial and Engineering Chemistry Research*, 2010, **49**, 10751–10757.

(24) A. Chaudhuri, S. D. Zondag, J. H. Schuurmans, J. Van Der Schaaf and T. Noël, *Organic Process Research and Development*, 2022, **26**, 1279–1288.

(25) M. M. de Beer, L. Pezzi Martins Loane, J. T. Keurentjes, J. C. Schouten and J. van der Schaaf, *Chemical Engineering Science*, 2014, **119**, 88–98.

(26) J. Kleiner, F. Haseidl and O. Hinrichsen, *Chemical Engineering and Technology*, 2017, **40**, 2123–2133.

(27) M. M. de Beer, J. T. Keurentjes, J. C. Schouten and J. Van der Schaaf, *Chemical Engineering Journal*, 2014, **242**, 53–61.

(28) F. Haseidl, P. König and O. Hinrichsen, *Chemical Engineering and Technology*, 2016, **39**, 2435–2443.

(29) A. N. Manzano Martínez, R. Jansen, K. Walker, M. Assirelli and J. van der Schaaf, *Chemical Engineering Research and Design*, 2021, **173**, 279–288.

(30) A. N. Manzano Martínez, K. M. Van Eeten, J. C. Schouten and J. Van Der Schaaf, *Industrial and Engineering Chemistry Research*, 2017, **56**, 13454–13460.

(31) A. N. Manzano Martínez, A. Chaudhuri, M. Besten, M. Assirelli and J. van der Schaaf, *Industrial and Engineering Chemistry Research*, 2021, **60**, 8677–8686.

(32) U. Phadke and J. Owen, *International Journal of Heat and Fluid Flow*, 1988, **9**, 98–105.

(33) J. Owen and R. Rogers, *Flow and Heat Transfer in Rotating Disc Systems, Vol.1: Rotor-Stator Systems*, Research Studies Press, 1989.

(34) S. Poncet, M. P. Chauve and P. Le Gal, *Journal of Fluid Mechanics*, 2005, **522**, 253–262.

(35) T. V. Kármán, *ZAMM - Journal of Applied Mathematics and Mechanics / Zeitschrift für Angewandte Mathematik und Mechanik*, 1921, **1**, 233–252.

(36) U. T. Bödewadt, *ZAMM - Journal of Applied Mathematics and Mechanics / Zeitschrift für Angewandte Mathematik und Mechanik*, 1940, **20**, 241–253.

(37) J. W. Daily and R. E. Nece, *Journal of Fluids Engineering, Transactions of the ASME*, 1960, **82**, 217–230.

(38) B. Launder, S. Poncet and E. Serre, *Annual Review of Fluid Mechanics*, 2010, **42**, 229–248.

(39) S. Poncet, R. Schiestel and M. P. Chauve, *Journal of Fluids Engineering, Transactions of the ASME*, 2005, **127**, 787–794.

(40) S. Haddadi and S. Poncet, *International Journal of Rotating Machinery*, 2008, **2008**, DOI: 10.1155/2008/635138.

(41)   S. Poncet, M. P. Chauve and R. Schiestel, *Physics of Fluids*, 2005, **17**, 1–15.

(42)   E. Severac, S. Poncet, E. Serre and M. P. Chauve, *Physics of Fluids*, 2007, **19**, DOI: `10.1063/1.2759530`.

(43)   Z. Jiao and S. Fu, *Science China: Physics, Mechanics and Astronomy*, 2018, **61**, DOI: `10.1007/s11433-018-9228-x`.

(44)   K. M. van Eeten, J. van der Schaaf, J. C. Schouten and G. J. van Heijst, *Physics of Fluids*, 2012, **24**, DOI: `10.1063/1.3698406`.

(45)   K. M. van Eeten, J. van der Schaaf, G. J. van Heijst and J. C. Schouten, *Physics of Fluids*, 2013, **25**, DOI: `10.1063/1.4812704`.

(46)   N. Y. Bailey, J. M. Owen, I. F. Mear and H. Tang, *Physics of Fluids*, 2022, **34**, DOI: `10.1063/5.0107336`.

(47)   N. C. Markatos, *Applied Mathematical Modelling*, 1986, **10**, 190–220.

(48)   M. Nallasamy, *Computers and Fluids*, 1987, **15**, 151–194.

(49)   S. N. A. Yusof, Y. Asako, N. A. C. Sidik, S. B. Mohamed and W. M. A. A. Japar, *CFD Letters*, 2020, **12**, 83–96.

(50)   P. J. Mason, *Quarterly Journal of the Royal Meteorological Society*, 1994, **120**, 1–26.

(51)   Y. Zhiyin, *Chinese Journal of Aeronautics*, 2015, **28**, 11–24.

(52)   P. Moin and K. Mahesh, *Annual Review of Fluid Mechanics*, 1998, **30**, 539–578.

(53)   G. Alfonsi, *Applied Mechanics Reviews*, 2011, **64**, 1–33.

(54)   M. Lesieur, *Journal of Applied Mechanics*, 1987, **55**, 254–254.

(55)   M. M. Yung, W. S. Jablonski and K. A. Magrini-Bair, *Energy and Fuels*, 2009, **23**, 1874–1887.

(56)   M. R. Beychok, *Am Chem Soc, Div Fuel Chem1974*, 1974, **19**, 85–93.

(57)   O. Tezer, N. Karabag, A. Ongen, C. O. Colpan and A. Ayol, *International Journal of Hydrogen Energy*, 2022, **47**, 15419–15433.

(58)   J. Ma, N. Sun, X. Zhang, N. Zhao, F. Xiao, W. Wei and Y. Sun, *Catalysis Today*, 2009, **148**, 221–231.

(59)   X. Sun, H. K. Atiyeh, R. L. Huhnke and R. S. Tanner, *Bioresource Technology Reports*, 2019, **7**, 100279.

(60)   I. K. Stoll, N. Boukis and J. Sauer, *Chemie-Ingenieur-Technik*, 2020, **92**, 125–136.

(61) S. W. Ragsdale and E. Pierce, *Biochimica et Biophysica Acta - Proteins and Proteomics*, 2008, **1784**, 1873–1898.

(62) H. N. Abubackar, M. C. Veiga and C. Kennes, *Bioresource Technology*, 2015, **186**, 122–127.

(63) J. Daniell, M. Köpke and S. Simpson, *Energies*, 2012, **5**, 5372–5417.

(64) L. G. Pereira, M. O. Dias, A. P. Mariano, R. Maciel Filho and A. Bonomi, *Applied Energy*, 2015, **160**, 120–131.

(65) K. Asimakopoulos, H. N. Gavala and I. V. Skiadas, *Chemical Engineering Journal*, 2018, **348**, 732–744.

(66) F. R. Bengelsdorf, M. Straub and P. Dürre, *Environmental Technology (United Kingdom)*, 2013, **34**, 1639–1651.

(67) T.-D. Hoang and N. Nghiem, *Fermentation*, 2021, **7**, 314.

(68) M. Mohammadi, G. D. Najafpour, H. Younesi, P. Lahijani, M. H. Uzir and A. R. Mohamed, *Renewable and Sustainable Energy Reviews*, 2011, **15**, 4255–4273.

(69) I. K. Stoll, N. Boukis and J. Sauer, *Chemie Ingenieur Technik*, 2018, **90**, 1283–1284.

(70) A. Infantes, M. Zwick, I. K. Stoll, N. Boukis, F. Oswald and A. Neumann, *Chemie Ingenieur Technik*, 2018, **90**, 1283–1284.

(71) W. Van Hecke, R. Bockrath and H. De Wever, *Bioresource Technology*, 2019, **293**, 122129.

(72) P. C. Munasinghe and S. K. Khanal, *Biotechnology Progress*, 2010, **26**, 1616–1621.

(73) P. C. Munasinghe and S. K. Khanal, *Bioresource Technology*, 2010, **101**, 5013–5022.

(74) M. Yasin, M. Cha, I. S. Chang, H. K. Atiyeh, P. Munasinghe and S. K. Khanal, *Syngas fermentation into biofuels and biochemicals*, Elsevier Inc., 2nd edn., 2019, pp. 301–327.

(75) M. L. Collignon, A. Delafosse, S. Calvo, C. Martin, A. Marc, D. Toye and E. Olmos, *Biochemical Engineering Journal*, 2016, **108**, 30–43.

(76) H. N. Abubackar, F. R. Bengelsdorf, P. Dürre, M. C. Veiga and C. Kennes, *Applied Energy*, 2016, **169**, 210–217.

(77) J. Chen, J. Daniell, D. Griffin, X. Li and M. A. Henson, *Biochemical Engineering Journal*, 2018, **129**, 64–73.

(78) B. Gunes, *Renewable and Sustainable Energy Reviews*, 2021, **143**, 110950.

(79) K. Valgepea, R. De Souza Pinto Lemgruber, T. Abdalla, S. Binos, N. Takemori, A. Takemori, Y. Tanaka, R. Tappel, M. Köpke, S. D. Simpson, L. K. Nielsen and E. Marcellin, *Biotechnology for Biofuels*, 2018, **11**, 1–15.

(80) J. K. Heffernan, K. Valgepea, R. de Souza Pinto Lemgruber, I. Casini, M. Plan, R. Tappel, S. D. Simpson, M. Köpke, L. K. Nielsen and E. Marcellin, *Frontiers in Bioengineering and Biotechnology*, 2020, **8**, 204.

(81) J. R. Puthalpet, *The Daunting Climate Change*, CRC Press, London, 2022.

(82) E. A. Abdelaziz, R. Saidur and S. Mekhilef, *Renewable and Sustainable Energy Reviews*, 2011, **15**, 150–168.

(83) W. W. Russell and G. H. Miller, *Journal of the American Chemical Society*, 1950, **72**, 2446–2454.

(84) P. Forzatti and L. Lietti, *Catalysis Today*, 1999, **52**, 165–181.

(85) M. Köpke, C. Mihalcea, F. M. Liew, J. H. Tizard, M. S. Ali, J. J. Conolly, B. Al-Sinawi and S. D. Simpson, *Applied and Environmental Microbiology*, 2011, **77**, 5467–5475.

(86) K. Asimakopoulos, H. N. Gavala and I. V. Skiadas, *Chemical Engineering Journal*, 2018, **348**, 732–744.

(87) X. Li, D. Griffin, X. Li and M. A. Henson, *Biotechnology and Bioengineering*, 2019, **116**, 28–40.

(88) X. Li, J. Chen, D. Griffin, X. Li and M. A. Henson, *Integrated Metabolic and Process Modeling of Bubble Column Reactors for Gas Fermentation*, Elsevier Masson SAS, 2018, vol. 44, pp. 2491–2496.

(89) R. Sander, *Atmospheric Chemistry and Physics*, 2015, **15**, 4399–4981.

(90) J. Yue, G. Chen, Q. Yuan, L. Luo and Y. Gonthier, *Chemical Engineering Science*, 2007, **62**, 2096–2108.

(91) E. Cussler, *DIFFUSION: MASS TRANSFER IN FLUID SYSTEMS*, Cambridge University Press, Third Edit, 2009.

(92) H. Benkreira, in *A-to-Z Guide to Thermodynamics, Heat and Mass Transfer, and Fluids Engineering*, Begellhouse, 2011.

(93) H. N. Abubackar, Á. Fernández-Naveira, M. C. Veiga and C. Kennes, *Fuel*, 2016, **178**, 56–62.

(94) M. T. Allaart, R. Kleerebezem and M. Diender, 2023, 1–9.

(95) M. Mann, K. Miebach and J. Büchs, *Biotechnology and Bioengineering*, 2021, **118**, 253–264.

(96) F. Oswald, I. K. Stoll, M. Zwick, S. Herbig, J. Sauer, N. Boukis and A. Neumann, *Frontiers in Bioengineering and Biotechnology*, 2018, **6**, DOI: `10.3389/fbioe.2018.00006`.

(97) A. J. Straathof, *Biochemical Engineering Journal*, 2023, **191**, 108796.

(98) L. Puiman, M. P. Elisiário, L. M. Crasborn, L. E. Wagenaar, A. J. Straathof and C. Haringa, *Biochemical Engineering Journal*, 2022, **185**, 108505.

(99) R. O. Norman, T. Millat, S. Schatschneider, A. M. Henstra, R. Breitkopf, B. Pander, F. J. Annan, P. Piatek, H. B. Hartman, M. G. Poolman, D. A. Fell, K. Winzer, N. P. Minton and C. Hodgman, *Engineering Biology*, 2019, **3**, 32–40.

(100) M. Charles, *Trends in Biotechnology*, 1985, **3**, 134–139.

(101) F. R. Schmidt, *Applied Microbiology and Biotechnology*, 2005, **68**, 425–435.

(102) J. S. Crater and J. C. Lievense, *FEMS Microbiology Letters*, 2018, **365**, 1–5.

(103) R. Maya-Yescas, R. Aguilar-López and G. Jiménez-Garciá, *Dynamics, controllability, and control of intensified processes*, Springer, 2016, pp. 293–325.

(104) G. W. Cave, C. L. Raston and J. L. Scott, *Chemical Communications*, 2001, **21**, 2159–2169.

(105) B. M. Sahoo and B. K. Banik, *Solvent-less reactions: Green and sustainable approaches in medicinal chemistry*, Elsevier Inc., 2020, pp. 523–548.

(106) M. Meeuwse, J. Van Der Schaaf and J. C. Schouten, *Industrial and Engineering Chemistry Research*, 2010, **49**, 1605–1610.

(107) M. Meeuwse, J. van der Schaaf, B. F. Kuster and J. C. Schouten, *Chemical Engineering Science*, 2010, **65**, 466–471.

(108) M. Meeuwse, J. V. D. Schaaf and J. C. Schouten, *AIChE Journal*, 2012, **59**, 215–228.

(109) J. Kleiner and O. Hinrichsen, *Chemical Engineering and Processing - Process Intensification*, 2019, **136**, 152–162.

(110) M. Meeuwse, E. Hamming, J. van der Schaaf and J. C. Schouten, *Chemical Engineering and Processing: Process Intensification*, 2011, **50**, 1095–1107.

(111) K. M. van Eeten, R. Verzicco, J. van der Schaaf, G. J. van Heijst and J. C. Schouten, *Chemical Engineering Science*, 2015, **129**, 14–24.

(112) K. M. van Eeten, H. H. Houben, J. van der Schaaf and J. C. Schouten, *Chemical Engineering Science*, 2014, **109**, 251–263.

(113) K. Boodhoo, in *Process Intensification for Green Chemistry: Engineering Solutions for Sustainable Chemical Processing*, John Wiley & Sons, Ltd, Chichester, UK, First, 2013, pp. 59–90.

(114) J. R. Burns, C. Ramshaw and R. J. Jachuck, *Chemical Engineering Science*, 2003, **58**, 2245–2253.

(115) R. HIGBIE, *Trans. AIChE*, 1935, **31**, 365–389.

(116) J. C. Lamont and D. S. Scott, *AIChE Journal*, 1970, **16**, 513–519.

(117) B. D. Prasher and G. B. Wills, *Industrial and Engineering Chemistry Process Design and Development*, 1973, **12**, 351–354.

(118) Y. Kawase and M. Moo-Young, *Chemical Engineering Research and Design*, 1988, **66**, 284–288.

(119) D. Dijkstra and G. J. Van Heijst, *Journal of Fluid Mechanics*, 1983, **128**, 123–154.

(120) S. Sideman, O. Hortacsu and J. W. Fulton, *Industrial & Engineering Chemistry*, 1966, **58**, 32–47.

(121) G. Jacquet-Richardet, M. Torkhani, P. Cartraud, F. Thouverez, T. Nouri Baranger, M. Herran, C. Gibert, S. Baguet, P. Almeida and L. Peletan, *Mechanical Systems and Signal Processing*, 2013, **40**, 401–420.

(122) P. F. Orrù, A. Zoccheddu, L. Sassu, C. Mattia, R. Cozza and S. Arena, *Sustainability (Switzerland)*, 2020, **12**, DOI: 10.3390/su12114776.

(123) T. Lin, Z. Zhu, X. Li, J. Li and Y. Lin, *Renewable Energy*, 2021, **168**, 31–44.

(124) A. Hakansson, *Processes*, 2018, **6**, 32.

(125) B. H. Samani, M. Behruzian, G. Najafi, E. Fayyazi, B. Ghobadian, A. Behruzian, M. Mofijur, M. Mazlan and J. Yue, *Fuel*, 2021, **283**, 118821.

(126) G. K. Batchelor, *Quarterly Journal of Mechanics and Applied Mathematics*, 1951, **4**, 29–41.

(127) M. Itoh, Y. Yamada, S. Imao and M. Gonda, *Experimental Thermal and Fluid Science*, 1992, **5**, 359–368.

(128) A. N. Manzano Martínez, A. Chaudhuri, M. Assirelli and J. van der Schaaf, *Chemical Engineering Journal*, 2022, **434**, 134292.

(129) H. S. Fogler, *Elements of Chemical Reaction Engineering, 5th Edition*, Pearson, 2016.

(130) M. L. Michelsen, *The Chemical Engineering Journal*, 1972, **4**, 171–179.

(131) D. Bošković and S. Loebbecke, *Chemical Engineering Journal*, 2008, **135**, DOI: `10.1016/j.cej.2007.07.058`.

(132) C. Greenshields and OpenFoam Foundation Ltd, *OpenFOAM v9 User Guide*, The OpenFOAM Foundation, London, UK, 2021.

(133) J. Smagorisnky, *Monthly Weather Review*, 1963, **91**, 99–164.

(134) F. Durst, *Turbulent Flows*, Cambridge University Press, 2022, pp. 601–669.

(135) N. Jiang and W. Layton, *Computers and Mathematics with Applications*, 2016, **71**, 2352–2372.

(136) T. Holzmann, *Mathematics, numerics, derivations and OpenFOAM*, Holzmann CFD, 7.0, 2019.

(137) L. F. Chen, J. Zang, A. J. Hillis, G. C. Morgan and A. R. Plummer, *Ocean Engineering*, 2014, **88**, 91–109.

(138) Y. Tominaga and T. Stathopoulos, *Atmospheric Environment*, 2007, **41**, 8091–8099.

(139) F. Visscher, J. De Hullu, M. H. De Croon, J. Van der Schaaf and J. C. Schouten, *AIChE Journal*, 2013, **59**, 2686–2693.

(140) F. V. D. Woerd, in *The business of Climate Change*, Routledge, London, 1st, 2005, ch. 12.

(141) A. N. Manzano Martínez, M. Assirelli and J. van der Schaaf, *Chemical Engineering Science*, 2021, **242**, DOI: `10.1016/j.ces.2021.116706`.

(142) A. N. Manzano MartÍnez, A. S. Haase, M. Assirelli and J. Van Der Schaaf, *Industrial and Engineering Chemistry Research*, 2020, **59**, 21359–21370.

(143) C. J. W. Hop, R. Jansen, M. Besten, A. Chaudhuri, M. W. Baltussen and J. van der Schaaf, *Physics of Fluids*, 2023, 9–11.

(144) A. N. Manzano Martínez, K. M. Van Eeten, J. C. Schouten and J. Van Der Schaaf, *Industrial and Engineering Chemistry Research*, 2020, **59**, 16095–16097.

(145) M. Fournier, L. Falk and J. Villermaux, *Chemical Engineering Science*, 1996, **51**, 5187–5192.

(146) P. Guichardon, L. Falk and J. Villermaux, *Chemical Engineering Science*, 2000, **55**, 4245–4253.

(147) J. R. DeBonis, AIAA SCITECH 2022 Forum, American Institute of Aeronautics and Astronautics, Reston, Virginia, 2022.

(148) E. Robertson, V. Choudhury, S. Bhushan and D. K. Walters, *Computers and Fluids*, 2015, **123**, 122–145.

(149) L. W. Browne, R. A. Antonia and D. A. Shah, *Journal of Fluid Mechanics*, 1987, **179**, 307–326.

(150) A. Jafari, S. M. Mousavi and P. Kolari, *Communications in Nonlinear Science and Numerical Simulation*, 2008, **13**, 1615–1626.

(151) A. Jafari, P. Zamankhan, S. M. Mousavi and P. Kolari, *Communications in Nonlinear Science and Numerical Simulation*, 2009, **14**, 1396–1402.

(152) Z. Zhang, J. Xu and X. Chen, ASME 2014 International Mechanical Engineering Congress and Exposition, Montreal, 2014, pp. 1–6.

(153) C. Greenshields, *OpenFOAM v8 User Guide*, The OpenFOAM Foundation, London, UK, 2020.

(154) D. K. Lilly, *National Center for Atmospheric Research*, 1966, DOI: 10. 5065/D67H1GGQ.

(155) D. K. Lilly, in *Proceedings of the IBM Scientific Computing Symposium on Environmental Sciences*, White Plains, New York, 1967, ch. 14, pp. 195–210.

(156) S. Pirozzoli, M. Bernardini and P. Orlandi, *Journal of Fluid Mechanics*, 2014, **758**, 327–343.

(157) J. Abrini, H. Naveau and E. J. Nyns, *Archives of Microbiology*, 1994, **161**, 345–351.

(158) G. Bratbak and I. Dundas, *Applied and Environmental Microbiology*, 1984, **48**, 755–757.

(159) F. M. B. Coelho, M. Nele, R. R. Ribeiro, T. F. Ferreira and P. F. F. Amaral, *CHEMICAL ENGINEERING TRANSACTIONS*, 2016, **50**, 277–282.

(160) S. J. Kim, J. Chang and M. Singh, *Biochimica et Biophysica Acta (BBA) - Biomembranes*, 2015, **1848**, 350–362.

(161) N. H. Mendelson and J. J. Thwaites, *Journal of Bacteriology*, 1989, **171**, 1055–1062.

(162) J. J. Thwaites and N. H. Mendelson, *International Journal of Biological Macromolecules*, 1989, **11**, 201–206.

(163) J. J. Thwaites and N. H. Mendelson, *International Journal of Biological Macromolecules*, 1991, **32**, ed. A. H. Rose and D. W. Tempest, 173–222.

(164) V. W. H. Herschel and R. Bulkley, *Kolloid-Zeitschrift*, 1926, **39**, 291–300.

(165) G. R. Burgos, A. N. Alexandrou and V. Entov, *Journal of Rheology*, 1999, **43**, 463–483.

(166) K. E. Wardle and H. G. Weller, *International Journal of Chemical Engineering*, 2013, **2013**, DOI: 10.1155/2013/128936.

(167) J. U. Brackbill, D. B. Kothe and C. Zemach, *Journal of Computational Physics*, 1992, **100**, 335–354.

(168) T. J. Pedley and J. O. Kessler, *Proceedings of the Royal Society of London - Biological Sciences*, 1987, **230**, 47–70.

(169) S. Wegner, T. Börzsönyi, T. Bien, G. Rose and R. Stannarius, *Soft Matter*, 2012, **8**, 10950–10958.

(170) R. M. Jones, *Deformation theory of plasticity*, Bull Ridge Publishing, Blacksburg, Virginia, 2009, pp. 146–160.

(171) M. S. Croughan, J. F. Hamel and D. I. Wang, *Biotechnology and Bioengineering*, 2006, **95**, 295–305.

(172) J. M. Davis, *Animal Cell Culture: Essential Methods*, Springer, 2011.

(173) Bender, Madigan, Buckley, Sattley and Stahl, *Brock Biology of Microorganisms FIFTEENTH EDITION*, 2019, pp. 62–65.

(174) S. W. Ragsdale, *Annals of the New York Academy of Sciences*, 2008, **1125**, 129–136.

(175) J. Mock, Y. Zheng, A. P. Mueller, S. Ly, L. Tran, S. Segovia, S. Nagaraju, M. Köpke, P. Dürre and R. K. Thauer, *Journal of Bacteriology*, 2015, **197**, ed. W. W. Metcalf, 2965–2980.

(176) S. Wang, H. Huang, H. H. Kahnt, A. P. Mueller, M. Köpke and R. K. Thauer, *Journal of Bacteriology*, 2013, **195**, 4373–4386.

(177) C. M. Humphreys, S. McLean, S. Schatschneider, T. Millat, A. M. Henstra, F. J. Annan, R. Breitkopf, B. Pander, P. Piatek, P. Rowe, A. T. Wichlacz, C. Woods, R. Norman, J. Blom, A. Goesman, C. Hodgman, D. Barrett, N. R. Thomas, K. Winzer and N. P. Minton, *BMC Genomics*, 2015, **16**, 1–10.

(178) S. D. Brown, S. Nagaraju, S. Utturkar, S. De Tissera, S. Segovia, W. Mitchell, M. L. Land, A. Dassanayake and M. Köpke, *Biotechnology for Biofuels*, 2014, **7**, DOI: 10.1186/1754-6834-7-40.

(179) A. Sobachkin and G. Dumnov, *NAFEMS World Congress 2013*, 2013, 1–20.

(180) B. Trevelyan and S. Mason, *Journal of Colloid Science*, 1951, **6**, 354–367.

(181) C. M. Zettner and M. Yoda, *Journal of Fluid Mechanics*, 2001, **442**, 241–266.

APPENDIX A

SUPPORTING INFORMATION: HIGH PRESSURE
FERMENTATION

A.1. Metabolic Pathway

C. autoethanogenum has been investigated extensively and with that, more insight is gained on the conversion of H_2, CO_2 and CO into acetic acid, ethanol and butane-2,3-diol. *C. autoethanogenum* utilises the Wood-Ljungdal Pathway (WLP) to fix the carbon into acetyl-CoA, thereafter acetyl-CoA is converted into the different products. The metabolic system of *C. autoethanogenum* consists of two parts: the catabolism and anabolism. The anabolism concerns reactions that consume energy and catabolism reactions providing energy and should in total result in a net positive adenine triphospate (ATP) production [173]. PH and concentration changes of intracellular components can lead to changes in production and selectivity, affecting the ATP-gain, thus cell reproduction and maintenance. This section only focuses on the direct routes converting carbon into the described products and the energy conservation of *C. autoethanogenum*. The proposed metabolic system is based on the work of Ragsdale et al., Mock et al. and Wang et al. [174–176] and presented in Figure A.1.

An important part of the metabolism are the energy carriers, nicotinamide adenine dinucleotide phosphate (NADPH), nicotinamide adenine dinucleotide (NADH) and ferredoxin (Fd) as electron donors. Additionally, ATP functions as an energy carrier, and is used or produced in the metabolism. When NADPH, NADH and Fd are oxidised, *C. autoethanogenum* will reduce these compounds in order to maintain the availability of the energy carriers. The reduction steps are performed by the Hyt/FdhA, Nfn, ATPase and Rnf enzymatic complexes inside the organism. Mock et al. [175] and Wang et al. [176] determined the specific activities of the enzymes in *C. autoethanogenum*, which was later validated with transcriptional genome analyses performed by Humphreys et al. [177] and Brown et al. [178]. Therefore it was assumed that the enzymes with the highest specific activity are performing the reactions that are presented in Figure A.1.

When studying the energy carriers in Figure A.1, it can be observed that when the organisms are exposed to CO solely, CO first needs to be converted into CO_2. This reaction uses the carbon monoxide hydrogenase (CODH) enzyme, see Equation A.1. However, when only CO_2 is used, the organism will have difficulties in converting the reduced into oxidised ferredoxin, since the metabolic path utilises more Fd_{red}^{2-} than Fd_{ox}. Therefore, the organism prefers a presence of CO.

$$CO_2 + 2H^+ + Fd_{red}^{2-} <=> CO + H_2O + Fd_{ox} \qquad (A.1)$$
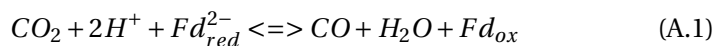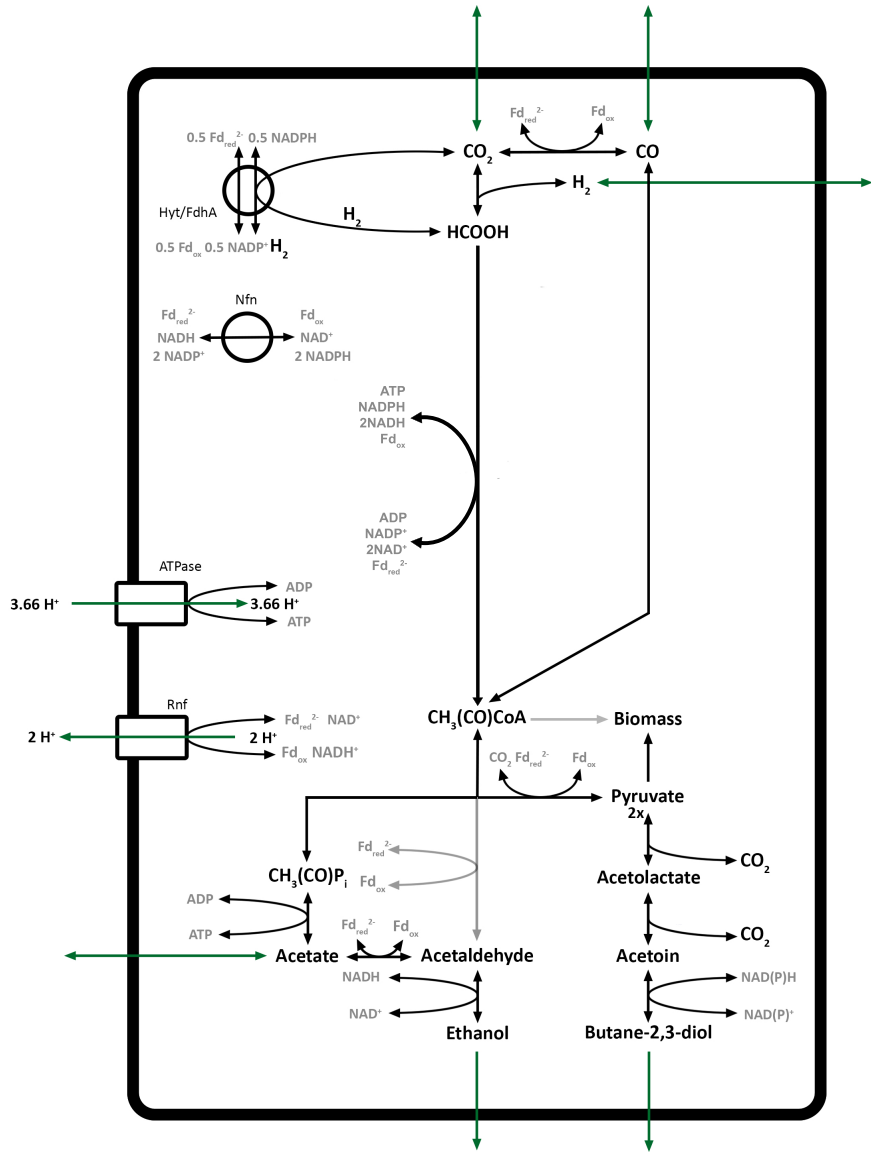
Figure A.1: Schematic overview of the proposed metabolism of *Clostridium autoethanogenum*

The next step is the formation of formate and this step requires H_2. The H_2 can be supplied in two ways, directly when H_2 is a substrate or indirectly via the enzematic Hyt/FdhA reaction. When H_2 is indirectly provided, the organism will require multiple additional steps, the utilisation of NADPH

A

and Fd_{red}^{2-} and the formation of NADPH and Fd_{ox}. The organism can function under a H_2 poor environment, but it will have a lower activity and therefore prefers an addition of H_2 in the substrate mixture. From this theoretical analyses, it appears that the optimal gas composition exists out of, CO, CO_2 and H_2.

Within Figure A.1, the intermediate steps from formate to acetyl-CoA are not presented and the energy carriers are lumped together into one reaction. Thereafter, acetyl-CoA can be reduced into acetate, ethanol, butane-2,3-diol or biomass and the selectivity depends on the availability of the energy carriers, internal/external concentration of acetate and the dissolved CO_2 concentration. The path from acetyl-CoA to acetaldehyde and biomass are presented in grey due to this being the less preferred option according to enzymatic activity from literature. Therefore, the ethanol productivity will be the highest in the presence of high acetate concentrations and butane-2,3-diol will be formed when there is a surplus of biomass and NAD(P)H. During the production of butane-2,3-diol, CO_2 is formed and in combination with the CODH path where CO is converted in CO_2, an accumulation CO_2 is possible. Therefore, the ideal gas composition should contain only CO and H_2 since CO_2 will be formed during the metabolism and thereafter be used as a substrate. This would optimise the gas utilisation and *C. autoethanogenum* should theoretically consume all the gas.

A.2. OPTICAL DENSITY TO CELL DRY WEIGHT

To convert measured optical density at 600 nm (OD_{600}) to dry cellular weight per liter (gDCW/L), a calibration was made. Samples of 60 mL with different OD_{600} values were taken from obtained bacterial colonies. Samples were centrifuged at 15000 rpm for 2.5 hours, creating a biomass 'cake' and liquid. The liquid was removed and refilled with 60 mL dH$_2$O. Samples were centrifuged again for 30 minutes. The formed biomass cake was spread over a alumina cup and placed in the oven at 80 °C for 48 hours to ensure complete removal of all liquid. Initial weight of the alumina cups was noted down. After 48 hours, samples are weighted again. Subtracting this weight from the initial weight of the alumina cup yields the dry cellular weight for 60 mL of the bacterial colony. This results in a relation between measured OD_{600} and gram dry cellular weight per liter. In A.2, the fit between experimental points and a correlation is made. This correlation is shown in Equation A.2 and yields in a R^2 of 0.92.

$$X = 0.0145 + \frac{OD}{3.9346} \tag{A.2}$$
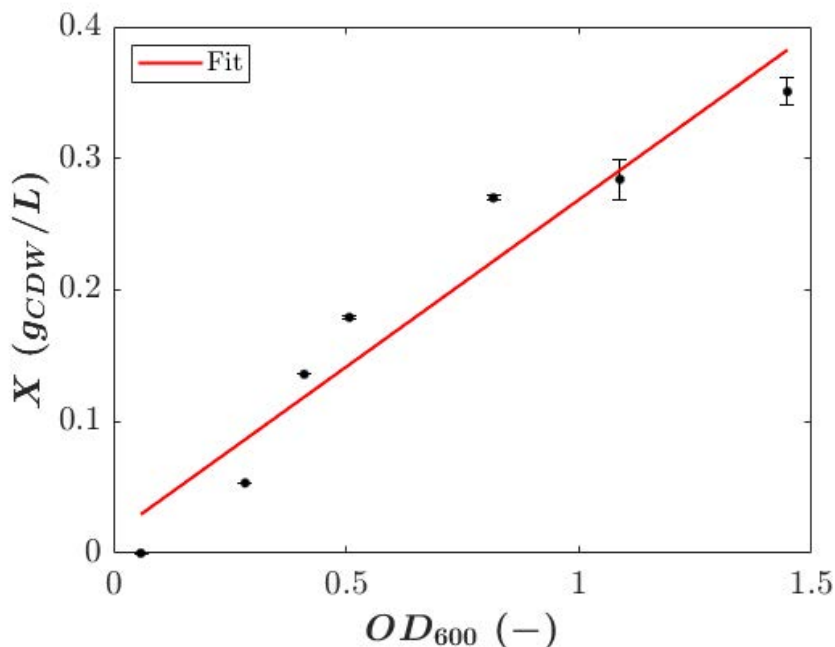
Figure A.2: Correlation between OD$_{600}$ and the grams of dry cellular weight.

A.3. CO CONCENTRATION

To determine the dissolved CO concentration along the length of stream 4 (Figure 2.1), a few assumptions had to be made:

- No reaction takes place in the tube.

- The flow is laminar ($Re_L \approx 460$) and therefore it was assumed that no dispersion took place and the flow could be assumed to be behaving as a plug flow reactor.

- The pressure remains constant along the length of the tube and therefore also the CO concentration.

- The tube was placed vertically and the hydrodynamic behavior was Taylor flow, therefore it was possible to use Equation 2.4.

- The incoming CO concentration was assumed to be 0 and the system was at steady state (no time dependency).

With these assumptions Equation A.4 was derived from a PFR mole balance (Equation A.3).

$$\frac{dN_L}{dt} = F_{in} - F_{out} + k_{GL}a_{GL}(P \cdot H - C_L)dV - r \cdot dV \tag{A.3}$$

$$\frac{dC_L}{dx} = \frac{k_{GL}a_{GL}}{v_L \epsilon_L}(P \cdot H - C_L) \tag{A.4}$$

Equation A.4 is solved by using Eulers method in Matlab and the results are depicted in Figure A.3. This graph presents the dissolved CO concentration along the length of stream 4. It depicts the 5 different experimental conditions that were tested, plus the saturation limit at the different pressures. This graph clearly shows the doubling in dissolved CO concentration when the pressure is increased from 5 to 10 bar(a). It also shows that the gas flow rate does not increase the mass transfer rate significantly and that after 1.5 m of tube length, the liquid is almost at the saturation limit.
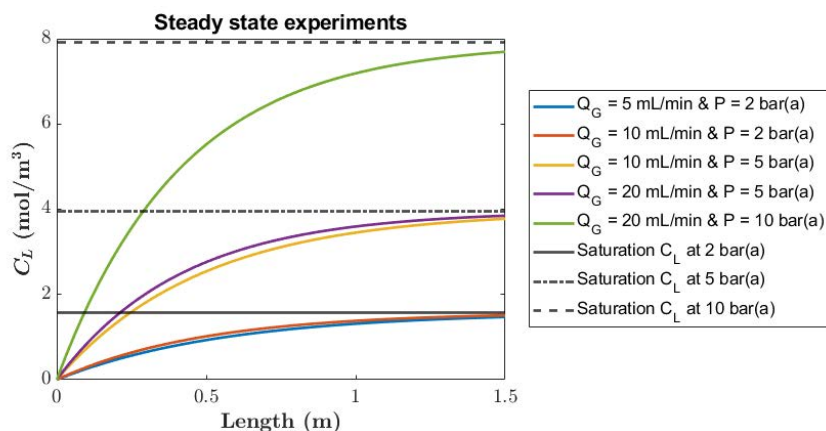
Figure A.3: The dissolved CO concentration (y-axis) in stream 4 (Figure 2.1) as function of the tube length (x-axis), with x = 0 the gas injection and x = 1.5 the autoclave (V_R). This graph depicts the dissolved CO concentration for the 5 different process conditions and the saturation limits based on Henry's law.

A.4. REPETITION EXPERIMENT

This section describes another fermentation experiment that was performed in the set up from Figure 2.1. During this experiment, three different conditions were tested and are listed in Table A.1. Unfortunately, steady state 3 was not completed due to a mismatch between the fresh medium inflow and the waste outflow and resulted in flooding of V_R. As a consequence, also the dilution rate is lower than was anticipated for steady state 2 and 3 since it was expected to start around 180 hours of operation. However, this experiment is still useful to compare trends and productivities with the experiment presented in Chapter 2.

Steady state	Total P bar(a)	Q_G mL/min	D h^{-1}	Time h
1	2	5	0.024	48
2	2	10	0.010	194
3	5	20	0.008	72

Table A.1: The experimental condition for every steady state is presented. Which include the pressures (P), gas flow rate (Q_G), dilution rate (D) and duration.

Figure A.4 shows the total experiment, with the steady states from Table A.1 highlighted by the colored regimes. It can be seen that with increasing gas flow and pressure, the biomass/product concentration

increases. This behaviour was also observed in Figure 2.2 and can be seen as a confirmation of the previously described behaviour. Since the pressure did not exceed 5 bar(a), the fermentation was kept below the regime where negative effects on the concentration were observed and it can not be confirmed if those effects were due to the high mass transfer rates or other influences.
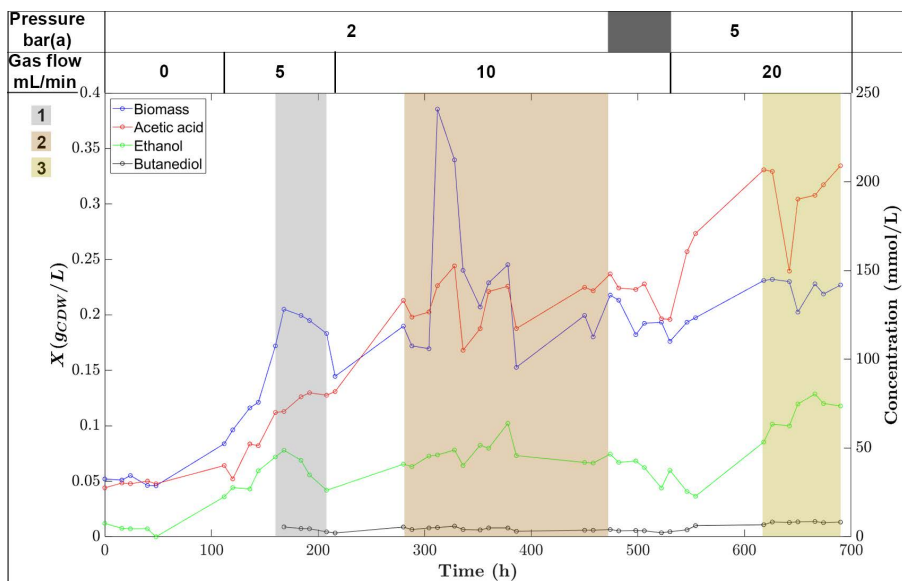
Figure A.4: Total experiment, with the biomass concentration on the left y-axis and the product concentrations on the right y-axis. The x-axis contains the time in hours and the color coded sections indicate the 3 experimental steady states that were reached during operation. Above the graph are the tested conditions and the numbers in the legend denote the different steady states as was shown in Table A.1.

The productivities for the proposed steady states are presented in Table A.2. Steady states 1, 2 and 3 are comparable with 1, 2 and 4 from Table 2.1 respectively. It can be concluded that SS 3 is not comparable, because it deviates 40 to 85% from experiment 4. This is most likely due to the much higher liquid hold up, since V_R over flooded with liquid during this run. Steady state 1 has the best agreement (below 15%), except for the butane-2,3-diol productivity and number 2 agrees for biomass and acetic acid (below 15%) and butane-2,3-diol is slightly more off (~22%), but ethanol productivity is much lower (~60%).

Steady state	Productivity mg/L/h			
	Biomass	**Acetic acid**	**Ethanol**	**butane-2,3-diol**
1	4.58 ± 0.32	109.65 ± 7.67	43.76 ± 10.00	9.44 ± 2.49
2	2.25 ± 0.68	79.63 ± 8.24	21.33 ± 3.01	4.02 ± 0.76
3	1.79 ± 0.08	92.82 ± 9.85	25.45 ± 3.50	5.80 ± 0.43

Table A.2: Growth rate and product formation at the 3 different steady states as was shown in Table A.1.

A.5. Supporting Information Figure 2.2

This section contains a more detailed explanation of Figure 2.2 and every event that took place during the fermentation is denoted in Figure A.5. The events are listed in Table A.3.

Event	Time (h)	Description
A	475	Started with dilution and Q_G to 5 mL/min
B	595	Q_G to 10 mL/min
C	675	Started stirrer
D	771	Stopped stirrer and dilution
E	1147	Restarted dilution
F	1243	Power shortage for 20 h
G	1267	Start pressure increase to 3 bar(a) with 0.353 bar/h
H	1292	Start pressure increase to 4 bar(a) with 0.353 bar/h
I	1315	Start pressure increase to 5 bar(a) with 0.353 bar/h
J	1346 - 1411	Malfunction of the pump system for the dilution
K	1635	Malfunction in the liquid refreshment pumps
L	1675	Q_G to 20 mL/min
M	2083	Start pressure increase to 10 bar(a) with 0.625 bar/h
N	2188	Sampling break
O	2613	Continued sampling without gas samples due to GC issues

Table A.3: Events that took place during the fermentation that was presented in Figure A.5.
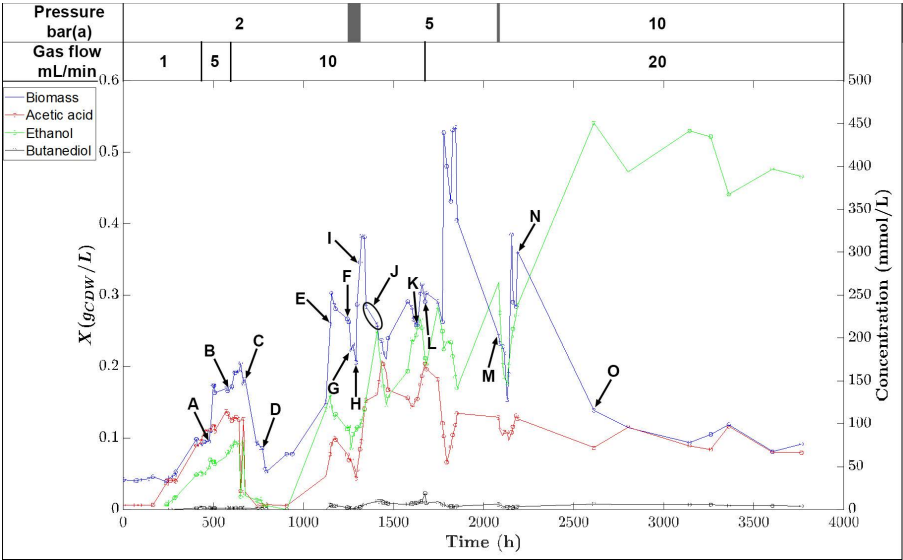
Figure A.5: The total experiment with a notation at every event that happened during the fermentation. The description of every letter is shown in Table A.3.

APPENDIX B

SUPPORTING INFORMATION: MASS TRANSFER STUDY

B.1. FILM REGION COMPARISON

To determine the mass transfer coefficient in the thin film region, a dynamic approach was used. This method switches between operation with gas flow and without gas flow and the system will re-saturate with O_2. From experience the amount of time needed to obtain the mass transfer rate in the film region was determent. The gas flow kept zero for another minute to average over five residence times. An example of the dynamic operation for two different viscosities was given in Figure B.1. Figure B.1a is a clear representation of the dynamic operation for water with one repetition. In this graph the clear distinction between operation with (minimum) and without (maximum) gas flow is shown in the peaks, the rpm was changed after every peak. When this experiment was performed for a water/glycerol mixture with μ = 10 mPa*s, no consistency between the experiments could be obtained, see Figure B.1b. This experiment was repeated twice and on the left side of the dashed line is the operation with gas flow and the right side without gas flow. Due to the big differences in three runs, it was therefore decided not to determine the thin film mass transfer coefficient.

(a) Water, $\mu = 1$ mPa*s
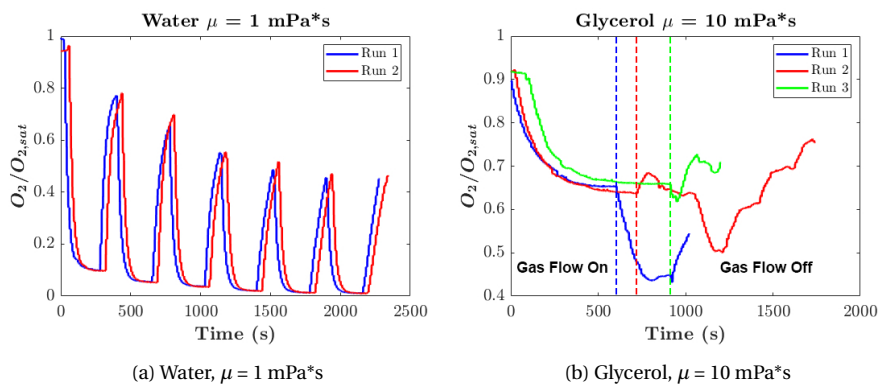
(b) Glycerol, $\mu = 10$ mPa*s

Figure B.1: The O_2 profiles for the dynamic operation with a) two water runs and b) three runs of glycerol-water mixture with $\mu = 10$ mPa*s.

B.2. FLOW DIRECTION

Within literature it was not clearly shown how the flow direction would affect the performance of the rs-SDR. For this, we investigated what would happen to the mass transfer rate if the rs-SDR was operated by co-feeding from the top to bottom and co-feeding from the bottom to the top at $\psi = 1$. These results are plotted in Figure B.2, with B.2a presenting the different flow directions for the overall mass transfer coefficient and B.2b the difference within the film region. From the Figures it seems that for both cases the bottom to top flow reaches a limitation in mass transfer coefficient at 50 rad/s. The reason for this different behaviour is likely due to the formation of two liquid thin film layers, one on the stator and one on the rotor [16]. According to literature, this phenomena exists by a reflux of liquid from the radial gap clearance creating another thin liquid layer, hence two thin film layers surrounding the gas phase.

(a) Overall mass transfer coefficient   (b) Film region contribution
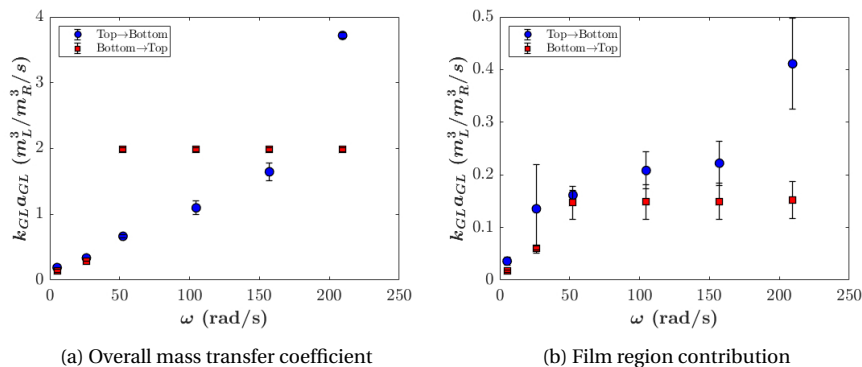
Figure B.2: Volumetric mass transfer coefficient for the two different flow directions at $\psi = 1$ for water with a) the total mass transfer coefficient and b) the film region mass transfer coefficient

APPENDIX C

SUPPORTING INFORMATION: LES OF THE RS-SDR

C.1. RESOLVED TURBULENT KINETIC ENERGY

In order to determine the amount of resolved turbulent kinetic energy, it is important to specify the measurement locations. OpenFOAM has a built-in function that measures user specified scalar/vector fields over time, named *probes*. First, the probes are placed according to the schematic representation in Figure C.1. There are 10 probes placed over an equal radial distance and this was repeated for three different heights in the top rotor stator cavity (blue zone), the same holds for the bottom rotor stator cavity (red zone) only with different radial positioning due to the shaft. Lastly, probes were placed in the vicinity of the rotor rim and is highlighted with the green box.

Secondly, the user defined values for the probe inputs were the velocity field (u_x, u_y and u_z), sub grid scale turbulent kinetic energy (k_{SGS}) and the sub grid scale energy dissipation rate (ϵ_{SGS}). These values were logged for 100 time steps. Due to our modeling technique, OpenFOAM only logs the sub grid scale TKE and a conversion is required to determine the total TKE (k). This conversion is given by Equations C.1 and C.2. With $\langle k \rangle$ denoting the resolved TKE, $\overline{(u'_x)^2}$ as the root mean square velocity fluctuation in the x-direction and TKE as the total turbulent kinetic energy [134].

$$\langle k \rangle = \frac{1}{2} \left(\overline{(u'_x)^2} + \overline{(u'_y)^2} + \overline{(u'_z)^2} \right) \tag{C.1}$$
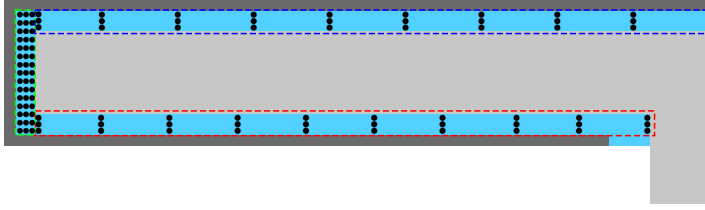
C

Figure C.1: Probe locations for the determination of the resolved turbulent kinetic energy inside the rs-SDR flowfield, with the blue zone denoting the probes placed in the top and red for the bottom rotor stator cavity. The green zone denote the probes placed at the vicinity of the rotor rim. Note that the sizes of the system are not scaled, this to make the probe locations more visible.

$$k = \langle k \rangle + k_{SGS} \qquad (C.2)$$

With both the resolved and total TKE known, it is possible to determine the percentage of resolved TKE at every probe location. These results are plotted in Figure C.2, with the x-axis the probe number in every region and the y-axis the fraction of resolved TKE. The colors represent the same regions as was depicted in Figure C.1. From this figure it can be concluded that the resolved TKE is on average higher than 70% (96.4% to be precise) and the grid is assumed to be sufficiently accurate to perform proper LES.
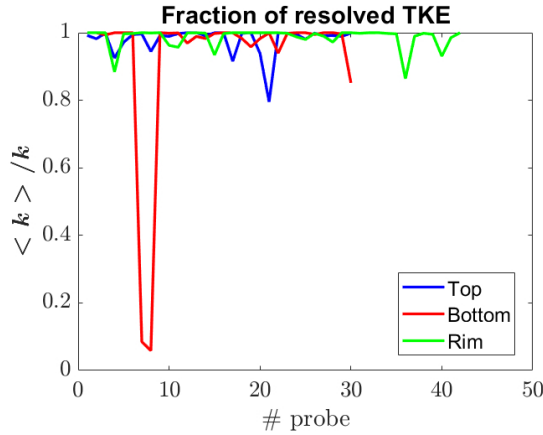
Figure C.2: The time averaged resolved TKE fraction at the probe locations from Figure C.1.

C.2. COMPARISON REACTOR MODELS

Previously, a comparison between the dispersion and De Beer model was made. This comparison was based on the goodness of the fit on the experimentally obtained outlet concentration. Another comparison that can be made, is the PFR volume fraction and these results can be found in Figure C.3a. The first observation is the difference in the experimentally obtained value by the fits, the De Beer model has a constant decline and the dispersion model shows first an increase followed by a constant decline. But, with increasing Reynolds the volume fraction seem to go towards a similar value. This behaviour can be explained by the fitted number of ideally mixed tanks, see Figure C.3b. In this figure, an increase in number of tanks is observed and is followed by a constant decrease with increasing Reynolds numbers. With the dispersion model assuming a single CSTR, it was expecting for the PFR volumes to reach a similar value, since the number of CSTRs drop towards one with increasing Reynolds numbers. Also, the difference in PFR volume is likely due to the different number of CSTRs, because they show a similar trend with respect to Reynolds. Lastly, the simulated PFR volumes and number of tanks are also plotted (asterisks). It seems that the PFR volumes for the De Beer model are underestimating the volume fraction (46.1 and 63.6% deviation from the mean), while the dispersion model falls within the experimental errors (5.4 and 6.5% deviation from the mean). For the number of CSTRs, there seems to be no match between the trends.
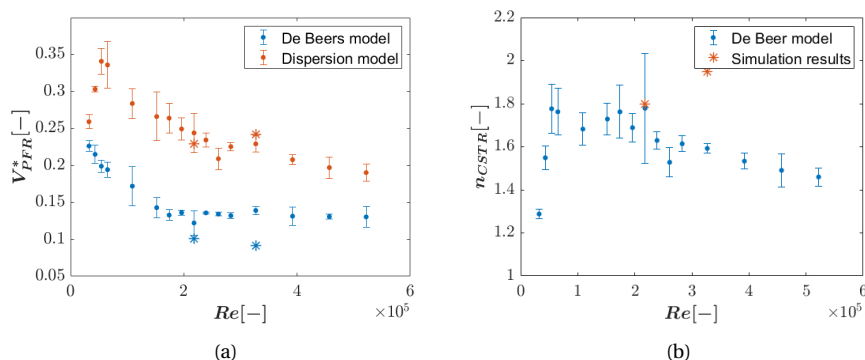
Figure C.3: (a) A comparison between the experimentally obtained results represented by the dispersion model (orange) and the model proposed by De Beer (blue). The simulated results for both models are depicted by the asterisks and in (b) the experimentally obtained number of tanks in series, with the asterisks as the computational results.

C.3. CONCENTRATION PROFILES 10 AND 75 RAD/S

This section show the difference in distribution of the tracer through the rs-SDR for 10 rad/s and 75 rad/s. From Figures C.4, C.5 and C.6 it can be concluded that the tracer moves in a more PFR way for the 10 rad/s case. This was also shown in Figure 4.7. At 75 rad/s it is clearly visible that the tracer moves in a homogeneous way through the rs-SDR and therefore it can be concluded that the system behaves more like a CSTR.
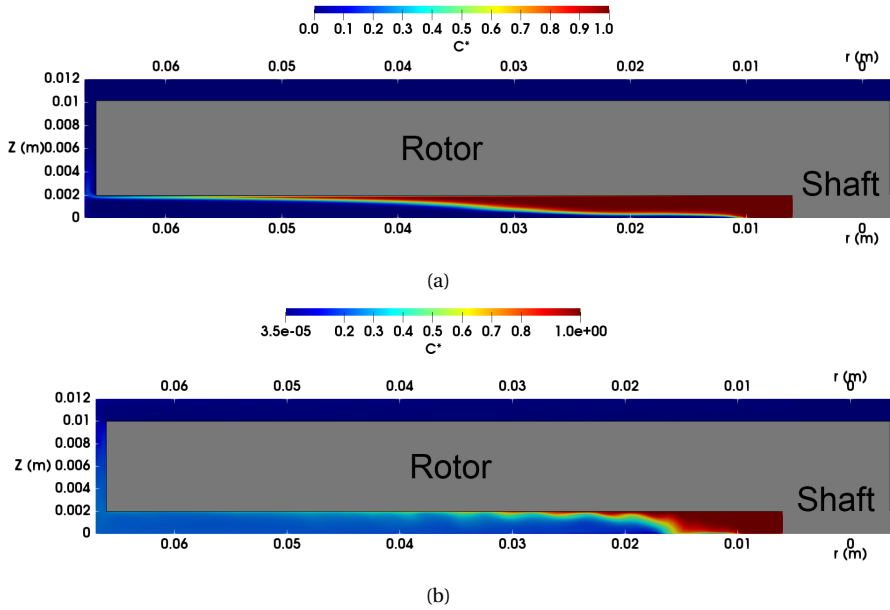
Figure C.4: The dimensionless concentration profiles for (a) 10 rad/s after 0.8 s and (b) 75 rad/s after 0.9 s.
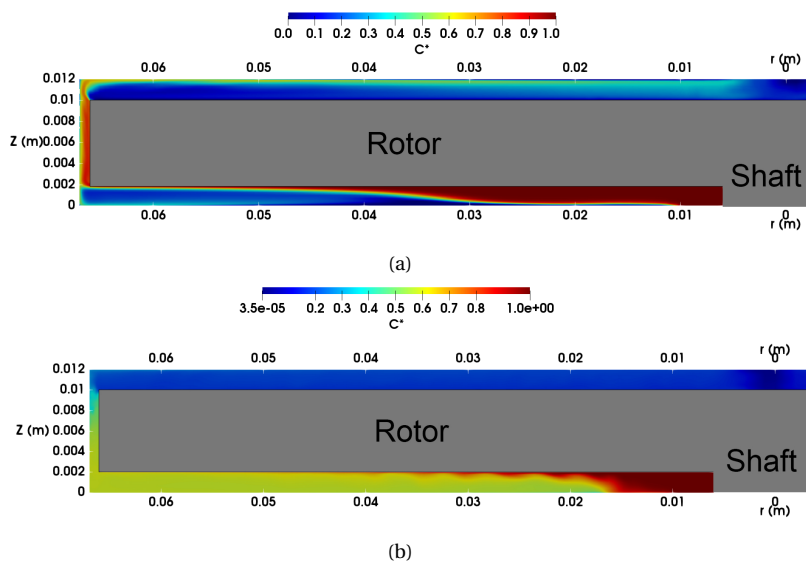
Figure C.5: The dimensionless concentration profiles for (a) 10 rad/s after 2.0 s and (b) 75 rad/s after 2.5 s.
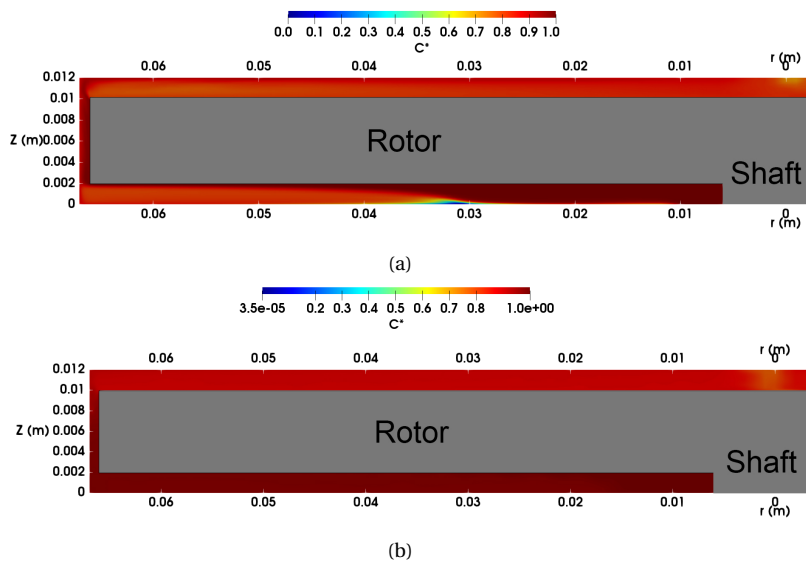
Figure C.6: The dimensionless concentration profiles for (a) 10 rad/s after 11 s and (b) 75 rad/s after 10.5 s.

C.4. ENTRAINMENT COEFFICIENT

Another option for validation can also be obtained from the entrainment coefficient (K), Equation 4.9, which is defined as the ratio between the

core tangential velocity and the tangential velocity of the rotor [39]. K was determined from Equation C.3 at $0.5R_D$ in the top rotor stator cavity, with $u_{\theta,core}$ the time averaged velocity at Z = 0.5.

$$K = \frac{|u_{\theta,core}|}{|u_{\theta,rotor}|} \tag{C.3}$$

A parity plot of the simulation results and Equation 4.9 is shown in Figure C.7. This figure clearly shows that the results in the turbulent regime correspond well with the correlation, i.e., the results are within the 5% error margin. The laminar case does not match the correlation, which is expected as the correlation is only applicable for the turbulent regimes [39].
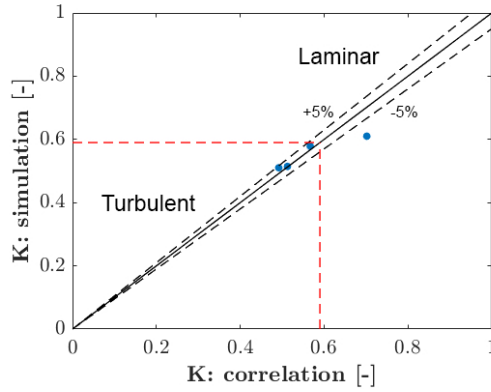
Figure C.7: Parity plot of the simulated entrainment coefficient and the coefficient defined by the correlation from Equation 4.9. Five percent deviation lines are included. Also the difference between the laminar and turbulent regimes is shown.

C.5. RADIAL VELOCITY PROFILES TOP AND BOTTOM ROTOR STATOR CAVITY

Figure C.8 shows the radial velocity profiles for every simulated case in both rotor stator cavities. The top cavity is depicted in Figure C.8a and it shows clearly a different pattern in the vicinity of the outlet ($0.01R_D$) compared to the other radial positions. This behaviour is due to the effect of the outlet. As it was expected, this effect becomes less when the rotational velocity increases, due to the flow becoming less throughflow dominated. In the bottom cavity (Figure C.8b), the profiles are different and seem to follow a Stewartson-like flow behaviour [36] at the inlet. In this case the bulk fluid is at rest and only a Von Kármán layer is formed.
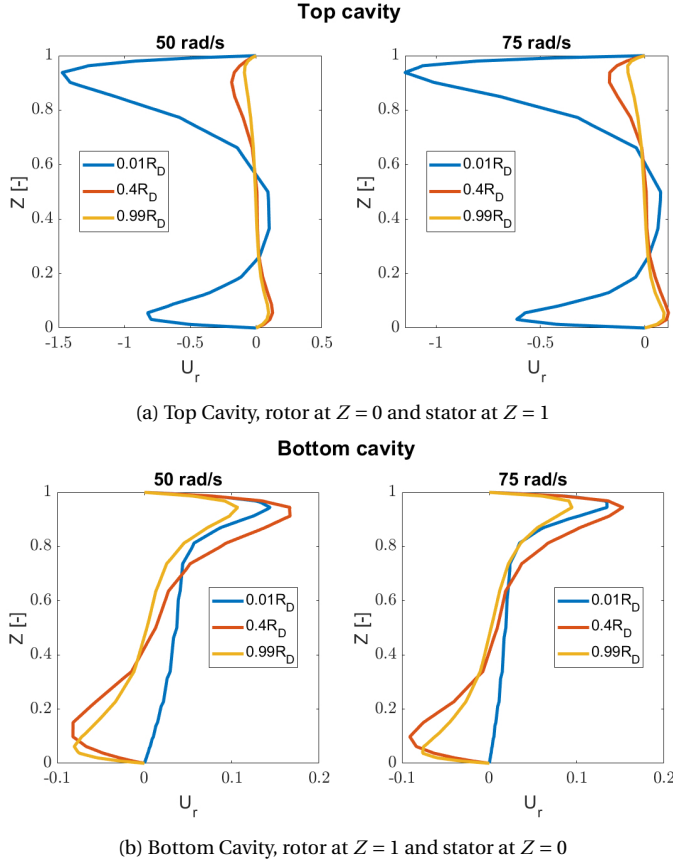
C

Top cavity

(a) Top Cavity, rotor at $Z = 0$ and stator at $Z = 1$

Bottom cavity

(b) Bottom Cavity, rotor at $Z = 1$ and stator at $Z = 0$

Figure C.8: Shows the radial velocity profiles of 50 and 75 rad/s at three different radial positions, with the rotor at $Z = 0$ and the stator at $Z = 1$, for figure (a). Note that for (b), the rotor ($Z = 1$) and the stator ($Z = 0$) locations are inverted. (a) Represents the top cavity, (b) the bottom cavity.

C.6. MEAN FIELDS 10 AND 25 RAD/S

Figures C.9 and C.10 depict the tangential and radial velocities for the centripetal (Figure C.9) and the centrifugal flow (Figure C.10) from 10 and 25 rad/s. When these figures are compared with the 50 and 75 rad/s cases, it can clearly be seen that the Batchelor flow is still present due to the inviscid core at the tangential velocity. This means that the simulations are not fully turbulent, as was also shown in Figure 5.2. Also, in the centrifugal flow a much bigger effect of flow rate is visible since the patterns of R_D = 0.01 and 0.4 are different from R_D = 0.99. As was also seen with 50 and 75 rad/s, the outlet (C.9, R_D = 0.01) shows a different velocity profile in

comparison with the higher radial positions.
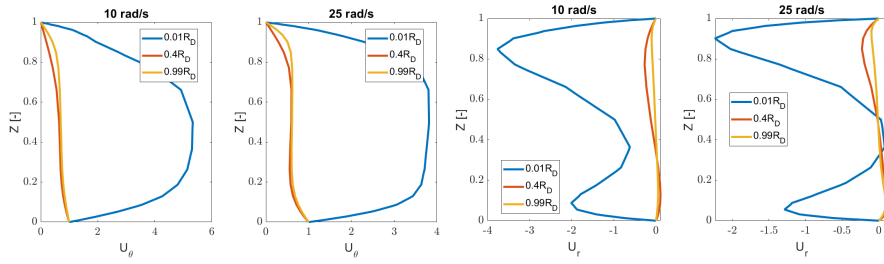
Figure C.9: Shows the radial and tangential velocity profiles of 10 and 25 rad/s at three different radial positions for the top cavity, rotor at $Z = 0$ and stator at $Z = 1$.
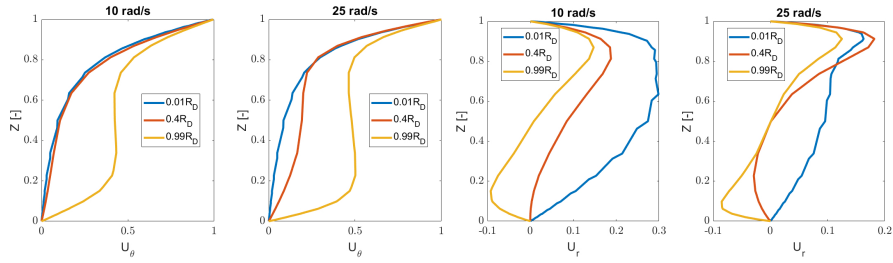
Figure C.10: Shows the radial and tangential velocity profiles of 10 and 25 rad/s at three different radial positions for the bottom cavity, rotor at $Z = 1$ and stator at $Z = 0$.

C

C.7. TURBULENT STATISTICS 50 RAD/S

Figure C.11 and C.12 visualize respectively the TKE and the EDR at 50 rad/s. Both figures show the profiles at $0.4R_D$ and (left graph) and $0.99R_D$ (right graph) and within these graphs the results for the top and bottom rotor stator cavities are plotted. The TKE for the 50 rad/s is within the same order of magnitude between the two rotor stator cavities and indicates that the system does not experience effects due to the inlet. Only near the rim of the rotor, a difference in the core is visible and is likely due to the centripetal flow being more turbulent as an effect of the flow passing the rotor stator radial gap. From the EDR it can be seen that there is a clear difference in radial positions for both cavities and is likely due to the shift from throughflow into rotational governed regimes for the centrifugal flow. For the centripetal flow this can be due to the additional turbulence that is present in the radial rotor stator cavity, as was also shown in the TKE.
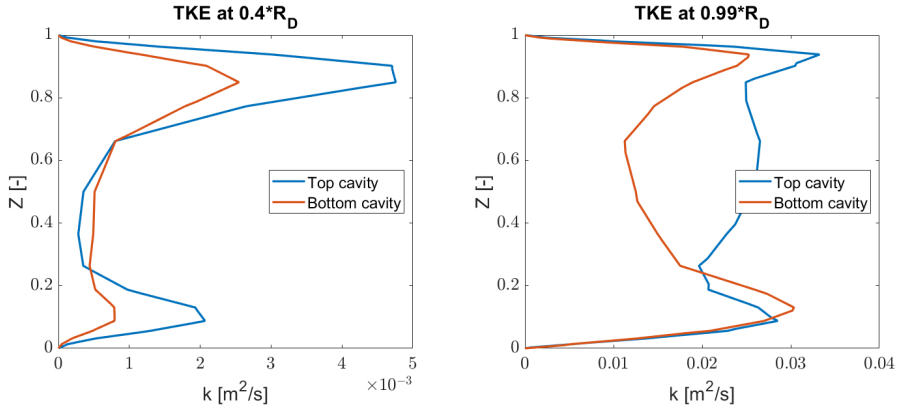
Figure C.11: Time averaged turbulent kinetic energy at 50 rad/s, with Z = 0 denoting the rotor and Z = 1 the stator. The blue line represents the rotor stator cavity above the rotor and the orange line under the rotor.

C
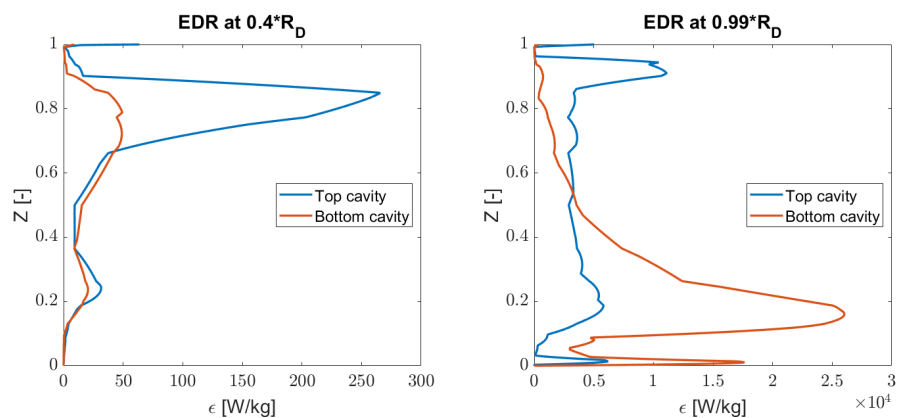
Figure C.12: Time averaged energy dissipation rate at 50 rad/s, with Z = 0 denoting the rotor and Z = 1 the stator. The blue line represents the rotor stator cavity above the disc and the orange line under the disc.

APPENDIX D

D.1. LOCAL ENERGY DISSIPATION RATE

In order to get an estimation of the local energy dissipation rate at different radial positions based on the torque exerted by the rs-SDR, a derivation analogous to the Beer et al. is performed [27]. The frictional torque over a cylindrical surface is given as follows [37]:

$$M = \int_0^{R_D} \int_0^{2\pi} r^2 \tau_r \, dr \, d\theta \tag{D.1}$$

τ_r denotes the shear stress at the rotor (Nm^{-2}). Daily and Nece [37] define a dimensionless moment coefficient:

$$C_M = \frac{2M}{\rho \omega^2 r_d^5} \tag{D.2}$$

For turbulent separated boundary layers (Batchelor flow) C_M is given as such [37]:

$$C_M = 0.0051 \left(\frac{s}{R_D} \right)^{1/10} Re_\Omega^{-1/5} \tag{D.3}$$

Combining Equations D.1 to D.3 gives:

$$0.002502 \rho s^{1/10} v^{1/5} \omega^{9/5} R_D^{9/2} = \int_0^{R_D} \int_0^{2\pi} r^2 \tau_r \, dr \, d\theta \tag{D.4}$$

Finding an expression for τ_r satisfying Equation D.4 yields:

$$\tau_r = 0.001794 \rho s^{1/10} v^{1/5} \omega^{9/5} r^{3/2} \tag{D.5}$$

The power exerted by the rotor on the fluid is given by the frictional torque (Equation D.1) times the rotational velocity. The local energy dissipation at a ring at a certain radial position can be found by dividing the surface integral of $\tau_r \omega r$ by the mass of the ring:

$$\epsilon_{loc} = \frac{\int_{r_b}^{r_f} \int_0^{2\pi} \tau_r \omega r^2 \, dr \, d\theta}{\rho \int_{r_b}^{r_f} \int_0^{2\pi} \int_0^{s} r \, dr \, d\theta \, dz} \tag{D.6}$$

The total frictional power exerted by both sides of the rotor on the fluid is consequently given by the surface integral of $\tau_r \omega r$ over the entire disc:

$$E_{dr} = 2 \int_{R_s}^{R_D} \int_0^{2\pi} \tau_r \omega r^2 \, dr \, d\theta \tag{D.7}$$

Substituting Equation D.5 into Equation D.7 and lumping all variables except r into a constant α_ϵ yields:

$$E_{dr} = 2\alpha_\epsilon \int_{R_s}^{R_D} r^{5/2} r dr \tag{D.8}$$

The total frictional power can also be experimentally assessed using the torque (M) of the motor exerted on the rotor, I being the current supplied to the motor and I_0 and M_c motor characteristics:

$$E_{dr} = \omega M = \omega(I - I_0)M_c \tag{D.9}$$

By equating Equations D.8 and D.9 an experimental value for α_ϵ can be obtained. Introducing α_ϵ in Equation D.6 gives:

$$\epsilon_{loc} = \frac{\alpha_\epsilon \int_{r_b}^{r_f} r^{5/2} r dr}{\rho \int_{r_b}^{r_f} \int_0^{2\pi} \int_0^s r dr d\theta dz} \tag{D.10}$$

Equation D.10 gives a radial dependency of the local energy dissipation rate using the theory of Daily and Neece [37], but by the introduction of the parameter α_ϵ based on experimental results.

D.2. Resolved turbulent kinetic energy

To the determine the resolved turbulent kinetic energy, probes were placed to record the velocity and sub-grid scale kinetic energy at every timestep. The probes were placed at three different axial positions (0.1Z, 0.5Z and 0.9Z) and for every axial position three radial positions (0.21R_D, 0.42R_D and 0.64R_D) were used. Next to that, 6 equally spaced azimuthal positions were used for every axial and radial position and in total 54 probes were placed. The *probe* function logged for 200 time steps. Since LES with WALE only calculates the sub-grid scale kinetic energy in OpenFOAM the resolved kinetic energy needed to be calculated based on the velocity field. The equations are given below:

$$\langle k \rangle = \frac{1}{2} \left(\overline{(U_x')^2} + \overline{(U_y')^2} + \overline{(U_z')^2} \right) \tag{D.11}$$

$$k = \langle k \rangle + k_{SGS} \tag{D.12}$$

The equations denote $\langle k \rangle$ as the resolved TKE, $\overline{(u_x')^2}$ as the root mean square velocity fluctuation in the x-direction and k as the total turbulent kinetic energy [134]. With this it is possible to determine the percentage of resolved kinetic energy at every probe location. Figure D.1 contains the fraction of resolved kinetic energy and it can be concluded that $\langle k \rangle >$ 99.7% at every measured point in the rotor-stator cavity. Therefore it can be concluded that the grid size is sufficient to simulate the flow field with LES.
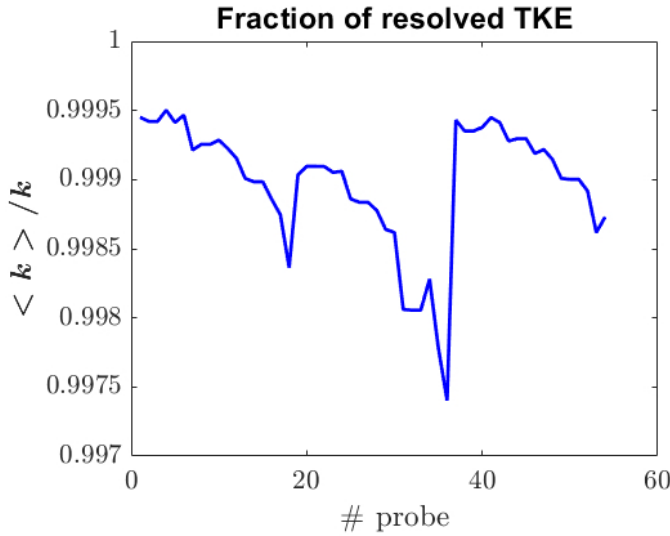
Figure D.1: Time averaged resolved turbulent kinetic energy at every probe location.

D.3. FLOW AROUND INJECTION TUBE

Micromixing experiments to probe the local hydrodynamics is an invasive technique because the tube used to inject the acid influences the flow pattern. The effect of the injection tube on the hydrodynamics is not taken into account in the simulation. To get a picture of the influence of the injection tube on a flow field, a qualitative investigation using the 3D modeling (CAD) program *Solidworks* was performed. *Solidworks* has the functionality to perform a flow simulation around, or inside, a designed 3D object (CAD embedded CFD). *Solidworks* was used instead of OpenFOAM because modeling the injection tube in OpenFOAM requires a very fine mesh around the injection tube to resolve the curvature. This increases the computational effort significantly compared to solving the undisturbed flow field. *Solidworks* allows for a swift assessment of the flow patterns around the injection tube using a relatively coarse grid and hence limited computational effort. It should be stressed out that this is only a qualitative survey to illustrate general trends. In SolidWorks, the tube used in the micromixing experiments was modeled. This tube was cylindrical in shape with a flattened side at the top where the outlet was located with a diameter of $0.5 \cdot 10^{-3}$ m. Around the injection tube a box was constructed and the dimensions of the box can be seen in Table D.1. A Couette type of flow was used to limit the computational effort and simplify the implementation. In the flow simulation utility of *Solidworks*, boundary conditions were

assigned to the box. At the inlet, a velocity profile was imposed of a steady-state turbulent flow, imported from the OpenFOAM simulation. At the top wall a translating velocity of 6.3 m s^{-1} was imposed (velocity rotor at injection location) and at the bottom wall a no-slip boundary was set (real wall in *Solidworks*). At the side and outlet a zero gradient boundary condition was set (standard option in *solidworks*) while for the injection tube a no-slip condition was set. A base computational mesh was specified, see Table D.1 for the number of cells in each direction. Additionally, a local mesh refinement was introduced around the injection tube and the top and bottom wall of the computational box. A refinement level of 2 was used, yielding a four-time finer grid at these locations compared to the base mesh. At the outlet of the injection tube, an even finer grid was used with a refinement level of 5. The computational mesh contained in total roughly 100 000 cells. Tripling the number of cells did not yield a qualitatively different result. The simulation was run till steady-state was achieved (constant mean velocity). The *Solidworks* flow solver uses the k-ϵ turbulence model (RAS), including a damping function, on a Cartesian grid (the mesh is not aligned with round objects such as in OpenFOAM using the *snappyHexMesh* utility) [179]. The functions, *Cut Plots* and *Flow Trajectories* were used to display the velocity and turbulence profiles and the trajectory of the fluid element from the tube outlet respectively.

Direction	Size	Number of cells
Streamwise (x)	12h	50
Wall normal (y)	2h	50
Spanwise (z)	h	10

Table D.1: Computational grid characteristics flow around injection tube simulation case with half-length h = 0.005 m.
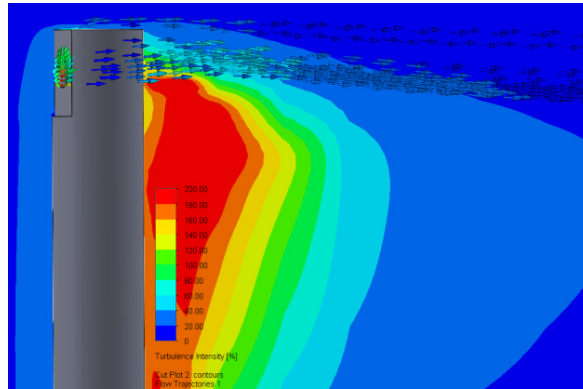
The turbulence intensity in a turbulent Couette flow field disturbed by an injection tube can be seen in Figure D.2. Three possible injection directions are shown (centripetal and centrifugal direction give the same result for a Couette flow hence referred to as perpendicular) and the trajectory of the injected acid, e.g. mixing zone, is displayed. Figure D.2 shows that the turbulence intensity is increased significantly in the wake of the cylinder compared to the main (undisturbed) flow field. Other turbulence quantities, such as the kinetic energy or energy dissipation rate follow the same (qualitative) profile, e.g. a strong increase in the wake of the injection tube. It can be noted that injecting the acid perpendicular to the flow direction exposes the acid to a higher turbulence intensity compared

to the other injection directions, where the acid or mixing zone is mainly transported to the outside of the wake (lower turbulence intensity).
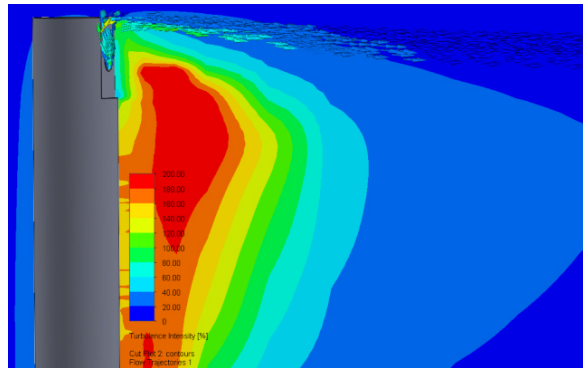
D
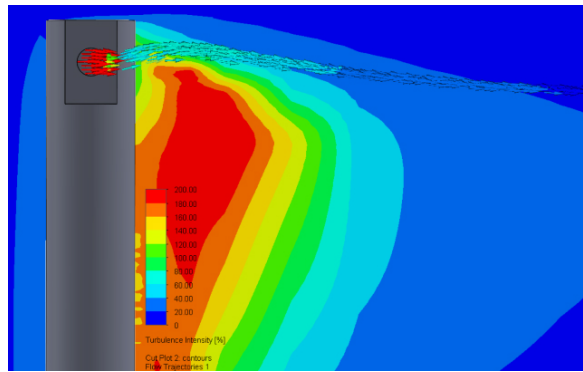
(a) Perpendicular

(b) Anti

(c) Con

Figure D.2: Qualitative representation of the flowfield around the injection tube for the different injection directions. The colours indicate the turbulence intensity and the vectors the flow trajectory of the mixing zone, red denoting the highest intensity and blue the lowest.

APPENDIX E

E.1. FERMENTATIONS AT HIGHER RPMS
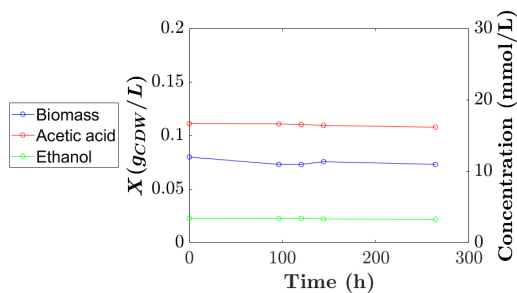
Figure E.1: 500 rpm experiment, with the biomass concentration on the left y-axis and the product concentrations on the right y-axis and the time in hours on the x-axis.
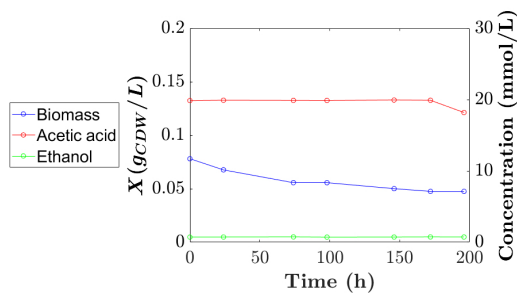
Figure E.2: 1000 rpm experiment, with the biomass concentration on the left y-axis and the product concentrations on the right y-axis and the time in hours on the x-axis.
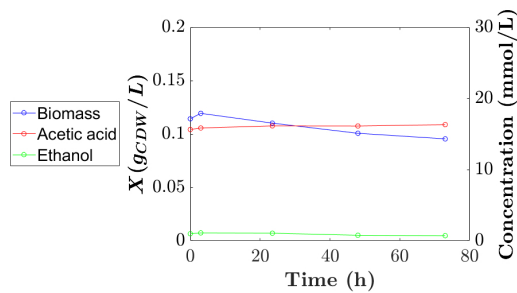
Figure E.3: 1500 rpm experiment, with the biomass concentration on the left y-axis and the product concentrations on the right y-axis and the time in hours on the x-axis.

E.2. MICROSCOPIC IMAGES

(a) t = 0 h, 1

(b) t = 0 h, 2

(c) t = 380 h, 1

(d) t = 380 h, 2
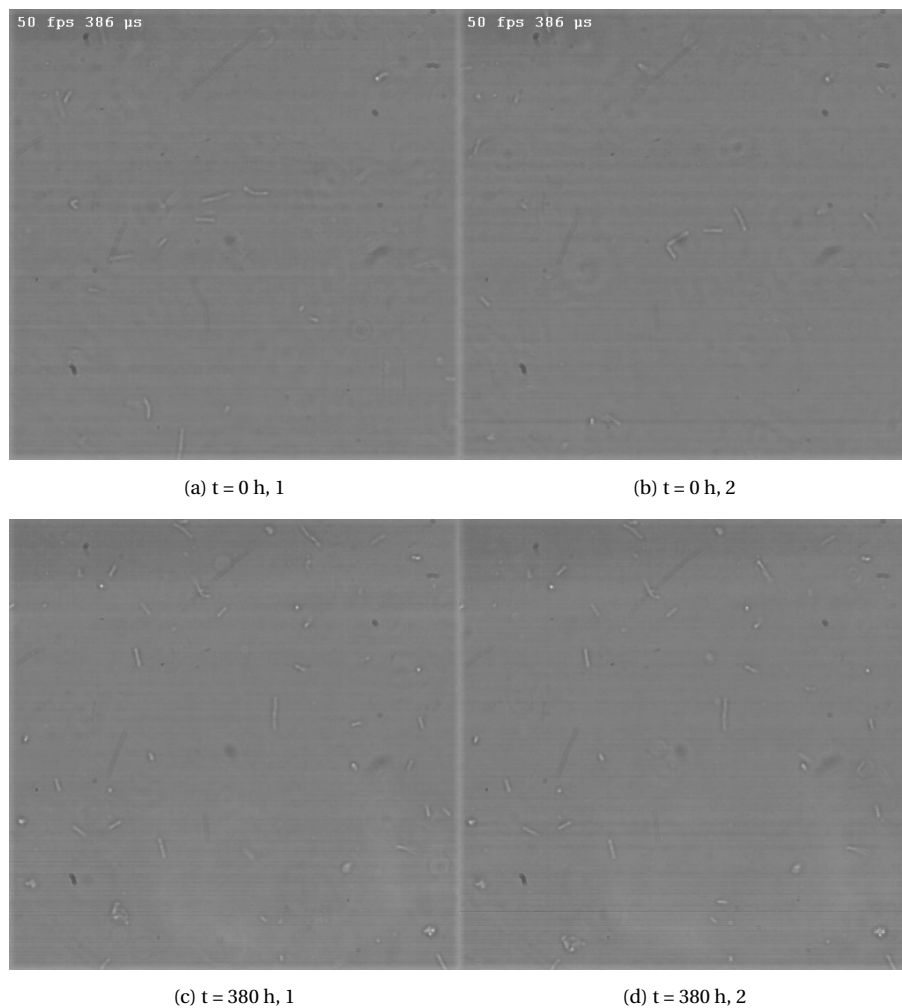
Figure E.4: Microscopic pictures made before (a and b) and after (c and d) the operation in the rs-SDR at 100 rpm. The images are taken with a zoom of 67x and were analysed with a threshold of 5 pixels, so all objects with an area below 5 pixels are not taken into account.
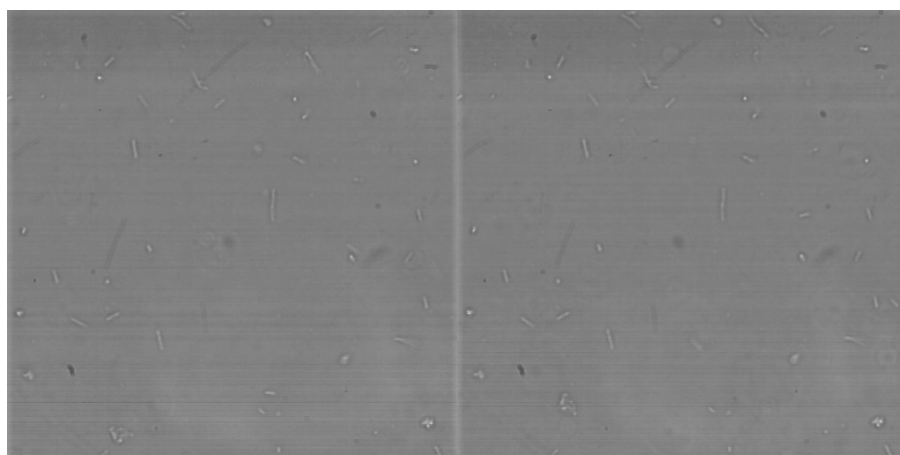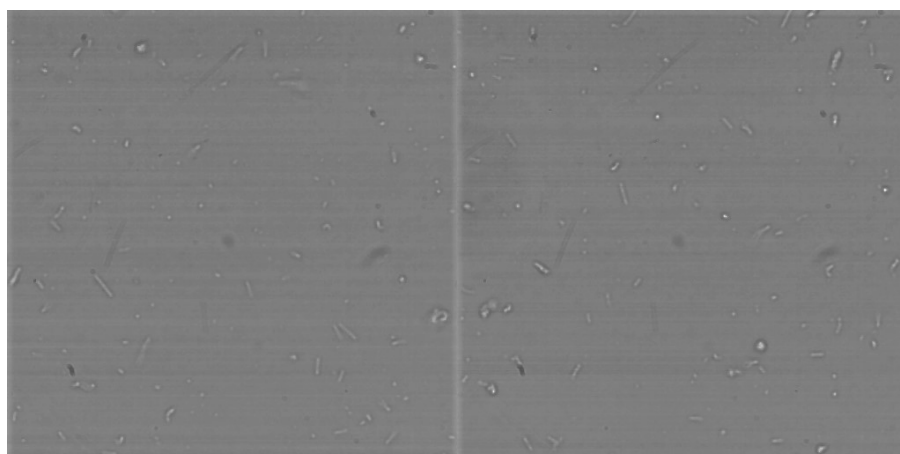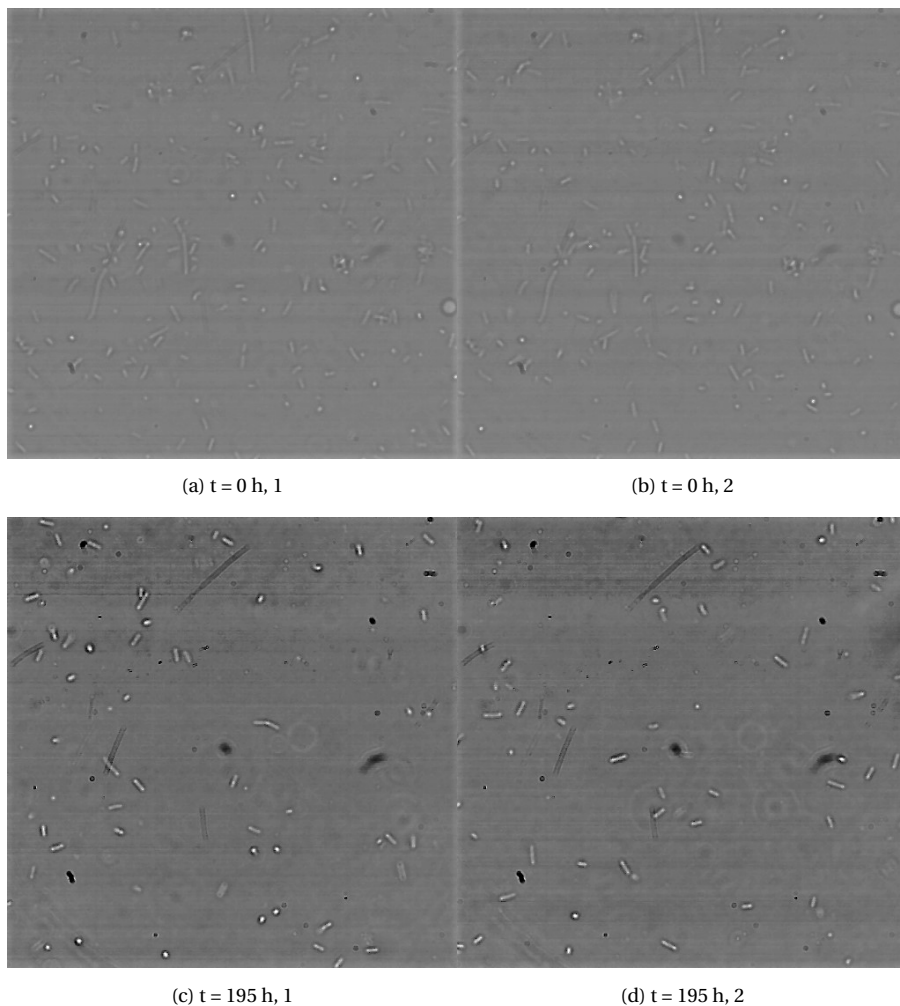
(a) t = 0 h, 1

(b) t = 0 h, 2

(c) t = 265 h, 1

(d) t = 265 h, 2

Figure E.5: Microscopic pictures made before (a and b) and after (c and d) the operation in the rs-SDR at 500 rpm. The images are taken with a zoom of 67x and were analysed with a threshold of 5 pixels, so all objects with an area below 5 pixels are not taken into account.
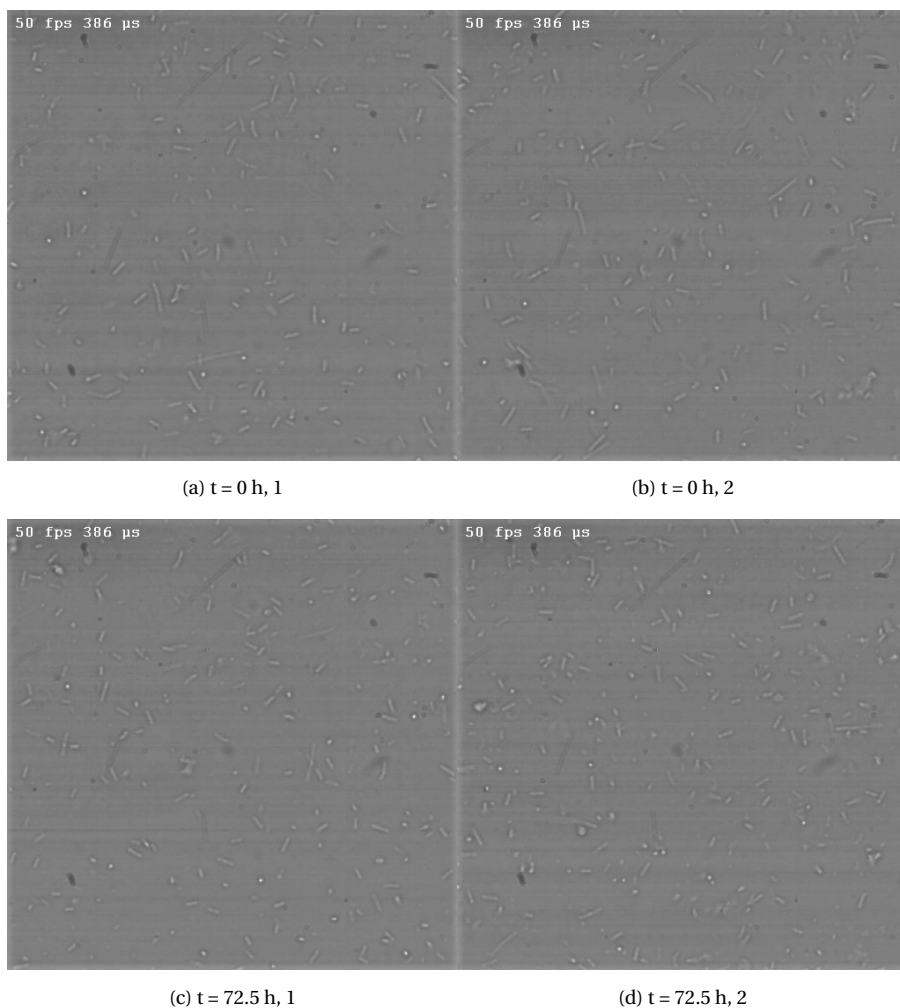
(a) t = 0 h, 1

(b) t = 0 h, 2

(c) t = 195 h, 1

(d) t = 195 h, 2

Figure E.6: Microscopic pictures made before (a and b) and after (c and d) the operation in the rs-SDR at 1000 rpm. The images are taken with a zoom of 67x and were analysed with a threshold of 5 pixels, so all objects with an area below 5 pixels are not taken into account.

(a) t = 0 h, 1   (b) t = 0 h, 2

(c) t = 72.5 h, 1   (d) t = 72.5 h, 2

Figure E.7: Microscopic pictures made before (a and b) and after (c and d) the operation in the rs-SDR at 1500 rpm. The images are taken with a zoom of 67x and were analysed with a threshold of 5 pixels, so all objects with an area below 5 pixels are not taken into account.

E.3. CAVITY FLOWFIELD VALIDATION

In order to validate the simulation procedure of LES in OpenFOAM, DNS data of a Couette flow from Pirozolli et al. was used [156]. The Couette geometry was 0.05 m in all three dimensions and the gridsizes from Table E.1 were tested as a grid dependency study. Additional to the three different mesh sizes (coarse, middle and fine), there is also an unresolved mesh and it is implemented without wall functions. The mesh was constructed using the *blockMesh* utility and in the y-direction an expansion coefficient of 200 was used to ensure wall resolving and place grid cells in the viscous sublayer.

	N_x	N_y	N_z
Coarse	40	85	40
Middle	50	110	50
Fine	65	100	65
Unresolved	50	50	50

Table E.1: The number of gridcells for the grid dependency study of the Coutte validation.

As a numerical implementation, *Crank-Nicolson* with a blending coefficient of 0.9 was used for the time discretisation, *Guass linear* for the gradient and divergence terms, *Gauss linear corrected* for the laplacian operator, a *linear* inerpolation scheme and the surface-normal gradients were solved with the *orthogonal* scheme. These numerical schemes are the standard schemes in OpenFOAM and were found to be sufficient. Lastly, the PISO algorithm was selected with two correctors and WALE as the LES sub-grid-scale model with a cutoff width *cubeRootVol* [135, 136].

The sides of the domain are treated as *cyclic* boundaries and resemble an infinite plate situation. The pressure field was initialised at 0 and the top and bottom walls were given a *zeroGradient* boundary condition. Spalding's wall function was applied for the turbulent viscosity to force the correct viscosity near the wall and it was initialised at the kinematic viscosity of the system. The velocity at the top and bottom wall was set with a no-slip boundary condition and the initial field was acquired by applying Gaussian perturbations in all direction to a linear velocity profile to ensure a turbulent initial velocity field.

The flowfield was resolved by using the *pisoFoam* solver in parallel with the *mpirun* utility on 16 cores with the *scotch* method. The timestep was manually selected to maintian the CFL number below 0.2. The flowfield was assumed steady state when the relative difference between

E

two timesteps was around 0.

The results of the Couette validation together with the grid dependency study are depicted in Figure E.8. It can be seen that all simulations match the DNS profile well and that the unresolved simulation is almost identical to the coarse mesh. However, the coarse and unresolved cases have a slight mismatch near the wall, this is related to a y^+ value that is too large for resolving the viscous sublayer. The middle and fine mesh did not suffer this problem and are not deviating much from each other. Therefore, in order to limit computational time, it was chosen to apply the middle mesh size for the remaining simulations.

E
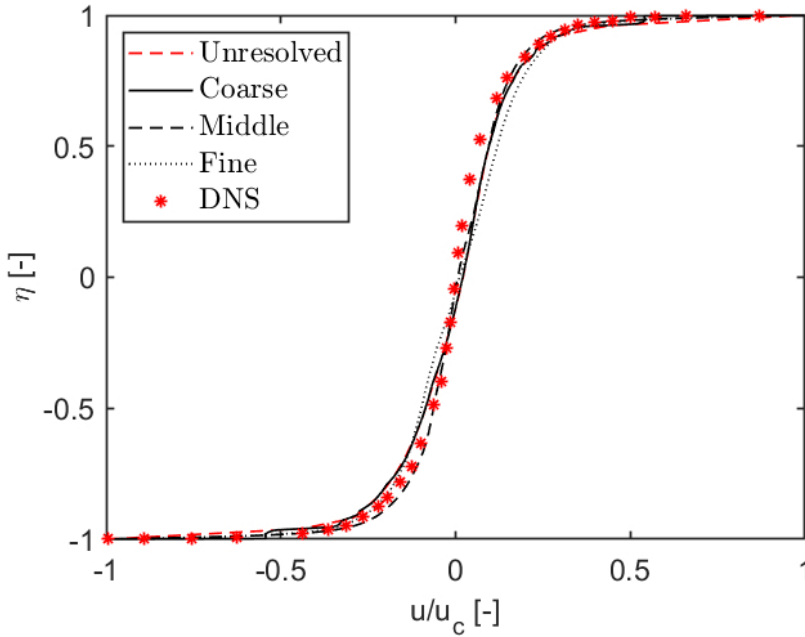
Figure E.8: Validation of the Coutte flow at Re = 21333 with DNS data obtained by Pirozolli et al. [156] and three different mesh sizes as denoted in Table E.1. The unresolved case is a mesh without wall-resolving.

E.4. BACTERIAL CELL IMPLEMENTATION

In order to incorporate a single bacterial cell in the Couette flow (Supporting Information E.3), the cell was initialized in the center of the domain and is schematically depicted in Figure E.9. The dimensions were taken from the microscopic pictures as depicted in Supporting Information E.2 and the shape can be described as a cylinder with two hemispherical caps.
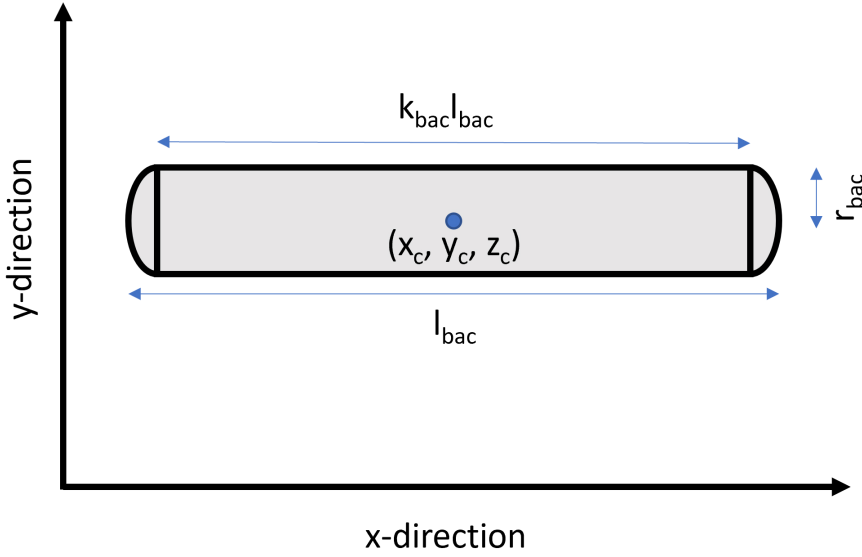

Figure E.9: Schematic overview of a bacterial cell in the Couette flow case.

The cylinder is implemented in OpenFOAM according to the following relation:

$$(y - y_c)^2 + (z - z_c)^2 \leq r_{bac}^2 \qquad \wedge \qquad x_{begin} \leq x \leq x_{end} \qquad \text{(E.1)}$$

The hemispherical caps are represented by the following two relations:

$$\frac{(x - (x_c - 0.5 k_{bac} l_{bac}))^2}{((1 - k_{bac}) l_{bac})^2} + \frac{(y - y_c)^2}{r_{bac}^2} + \frac{(z - z_c)^2}{r_{bac}^2} \leq 1 \qquad \text{(E.2)}$$

$$\frac{(x - (x_c + 0.5 k_{bac} l_{bac}))^2}{((1 - k_{bac}) l_{bac})^2} + \frac{(y - y_c)^2}{r_{bac}^2} + \frac{(z - z_c)^2}{r_{bac}^2} \leq 1 \qquad \text{(E.3)}$$

Due to the turbulent field, it is most likely that the cell will start rotating from its original orientation. This rotation corresponds to a matrix

operation as is defined in Equation E.4 and θ as the rotation angle around the z-axis. The coordinate transformation is described by Equations E.5 to E.7, and can be applied to the equations that describe the geometry. These equations already have the rotation around the center point implemented (x_c, y_c, z_c).

$$\begin{bmatrix} x' \\ y' \\ z' \end{bmatrix} = \begin{bmatrix} cos\theta & -sin\theta & 0 \\ sin\theta & cos\theta & 0 \\ 0 & 0 & 1 \end{bmatrix} \tag{E.4}$$

$$x' = (x - x_c)cos\theta - (y - y_c)sin\theta + x_c \tag{E.5}$$

$$y' = (x - x_c)sin\theta + (y - y_c)cos\theta + y_c \tag{E.6}$$

$$z' = z \tag{E.7}$$

The rotation as described above is implemented in OpenFOAM and visualised in Figures E.10 to E.12 for Reynolds numbers of 21333, $5 \cdot 10^5$ and $1 \cdot 10^6$ respectively. The vectors in the figures are not scaled in comparison to the other figures and streamwise denotes the x-direction, wall-normal the y and spanwise the z-direction. The simulations were simulated for 0.2 eddy turn-over times ($t_{eddy} = $ h $uwall^{-1}$) and this time scale is the characteristic time at which one large eddy is dissipated into heat according to the energy cascade. From the figures it is clear that the drag forces will cause a rotation in the shear plane, and it is an effect of the shear acting on the elliptical cylinders as was also previously observed by numerical simulations and experiments [169, 180, 181]. Next to that, deformation is observed at Re = $1 \cdot 10^6$ in the wall-normal direction and this is corresponding to the predictions from the Von Mises and Tresca criteria and the simulated shear stress in the organism [170].
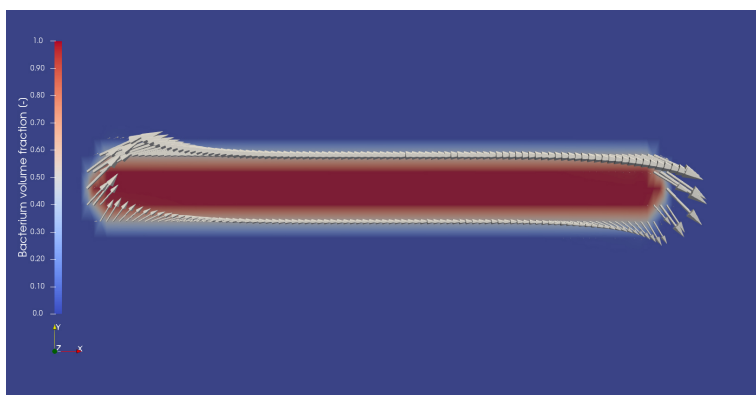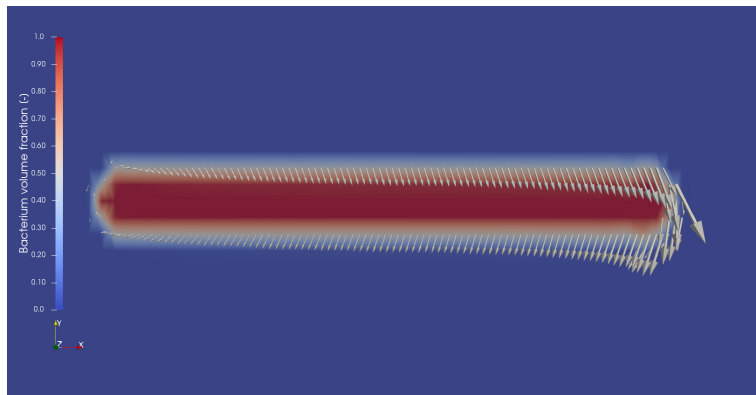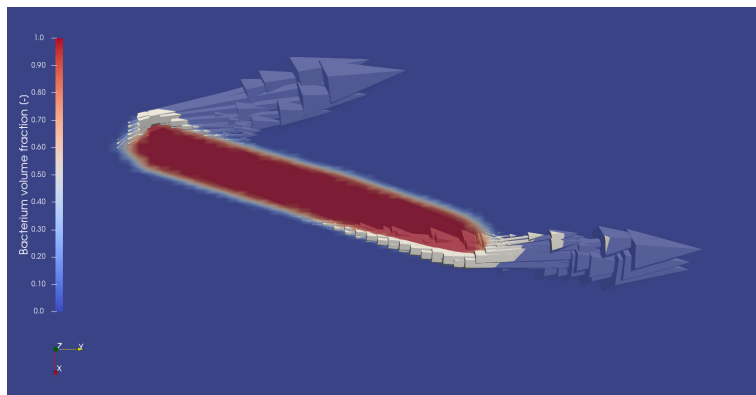
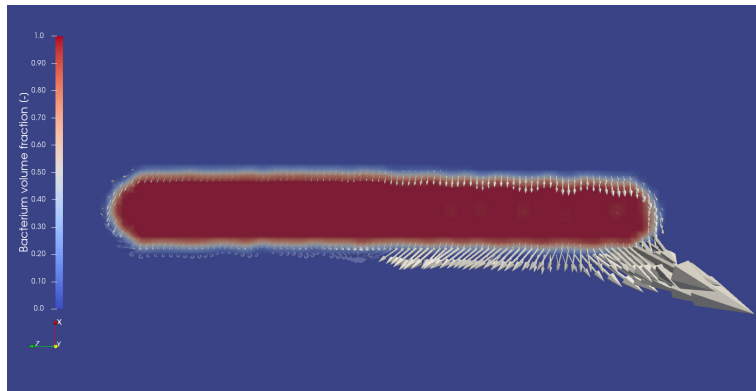(a) Streamwise
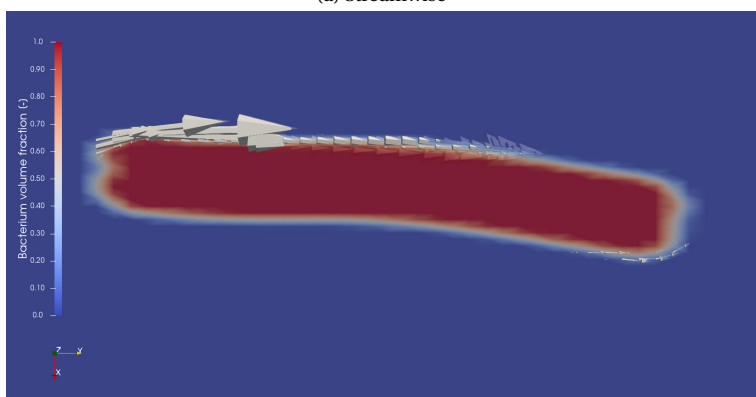
(b) Wall-normal
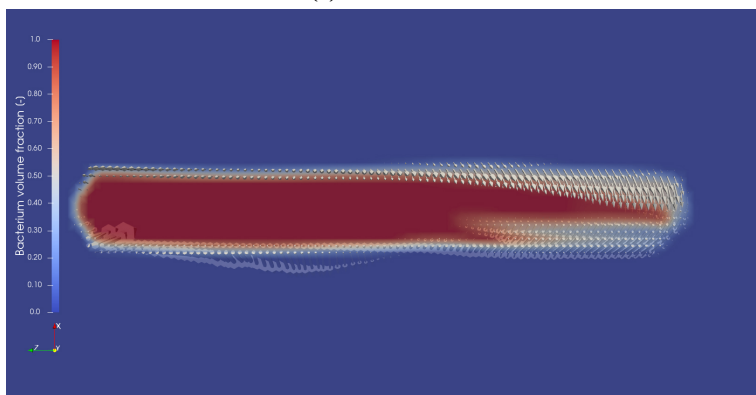
(c) Spanwise

Figure E.10: The drag forces that act on a bacterial cell at Re = 21333 for the different cell orientations. Note, the magnitude of the vectors are not scaled with respect to each individual figure.

(a) Streamwise

(b) Wall-normal

(c) Spanwise

Figure E.11: The drag forces that act on a bacterial cell at Re = $6 \cdot 10^5$ for the different cell orientations. Note, the magnitude of the vectors are not scaled with respect to each individual figure.

(a) Streamwise

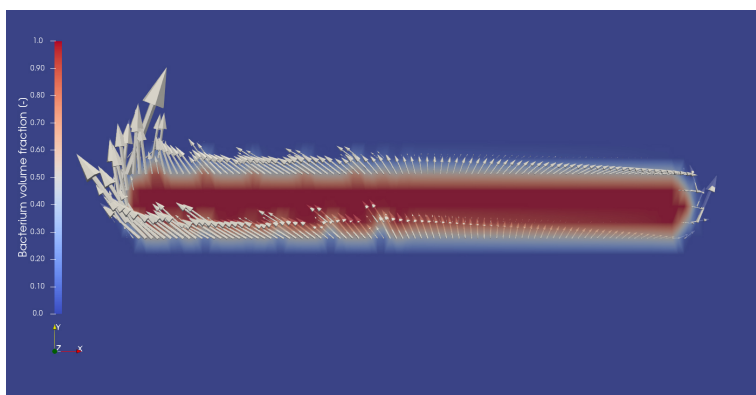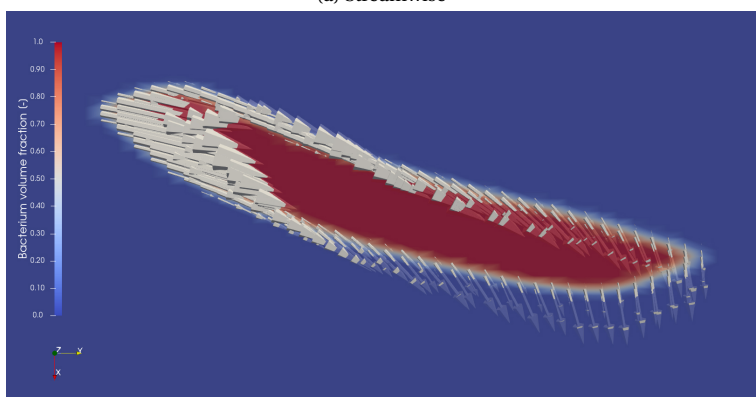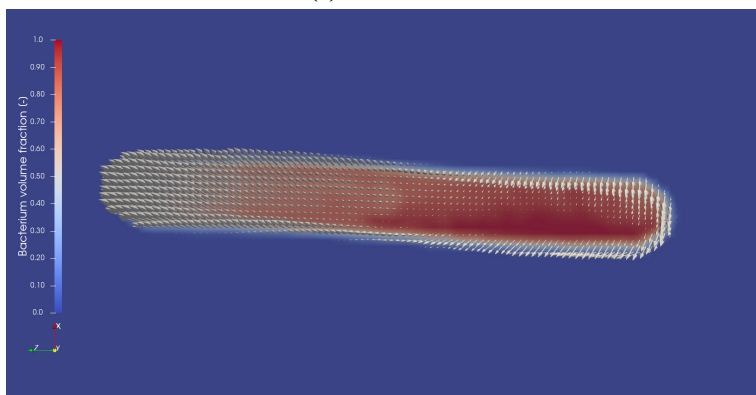(b) Wall-normal

(c) Spanwise

Figure E.12: The drag forces that act on a bacterial cell at Re = $1 \cdot 10^{6}$ for the different cell orientations. Note, the magnitude of the vectors are not scaled with respect to each individual figure.

LIST OF PUBLICATIONS

Journal Publications

1. C.J.W. Hop, R. Jansen, M. Besten, et al., "The hydrodynamics of a rotor stator spinning disc reactor: Investigations by Large Eddy Simulations," Physics of Fluids, pp. 9–11, Feb. 2023, ISSN: 1070-6631. DOI: 10.1063/5.0137405. [Online]. Available: https://aip.scitation.org/doi/10.1063/5.0137405

2. C.J.W. Hop, B. Zwaan, R. Dees, et al., "Syngas fermentation with Clostridium autoethanogenum at elevated pressures," 2023: In preparation

3. C.J.W. Hop, A. Chaudhuri, A. Meijer, et al., "Gas-Liquid Mass Transfer of Viscous Liquids in a Rotor-Stator Spinning Disc Reactor," 2023: In preparation

4. C.J.W. Hop, M. Besten, A. N. Manzano Martinez, et al., "Micromixing efficiency in the turbulent boundary layers in a rotor-stator spinning disc reactor," 2023: In preparation

Oral Presentations

1. C.J.W. Hop, A. Meijer, A. Chaudhuri and J. van der Schaaf, "Gas-liquid behavior of (non-) Newtonian fluids in a multistage spinning disc reactor" (ECCE), Berlin (online), September 2021

2. C.J.W. Hop, M. Benschop, B.B. Zwaan, and J. van der Schaaf, "A study on the effect of shear on Clostridium autoethanogenum in a rotor-stator spinning disc reactor" (NPS 17), Delft, April 2022

3. C.J.W. Hop, A. Chaudhuri, A. Meijer and J. van der Schaaf, "Gas-liquid mass transfer of viscous liquids in a rotor-stator spinning disc reactor" (CHISA 26), Prague, August 2022

4. C.J.W. Hop, R. Jansen, M. Besten, A. Chaudhuri, M.W. Baltussen, and J. van der Schaaf, "Large Eddy Simulations of a complete rotor-stator spinning disc reactor" (AIChE), Phoenix, November 2022

Poster Presentations

1. C.J.W. Hop and J. van der Schaaf, "New design for syngas converting bioreactors" (NPS 16), Eindhoven, October 2019

ACKNOWLEDGEMENTS

During my PhD journey there were a lot of ups and downs and this period has taught me some valuable lessons; no matter how bad it gets, with hard work, perseverance and the right attitude, things will get better and that even tough the PhD is lonely path, you are never alone. Therefore I would like to thank some very important people that helped me along this journey.

John, thank you for giving me the opportunity to continue doing research in your group after my Master thesis. I have learned so much during these 4 years and really enjoyed working with you. You gave me all the freedom to try new things and were always thinking with me when my bacteria were doing some random stuff again. I also appreciated that you pushed for critical thinking and high standards, which eventually made me more confident about my own work. Your mentality, knowledge and input really helped me go through this journey and made it possible to present this thesis. I also appreciated our informal conversations about solving world problems, education and the future. Also, is Evelyn still enjoying her nice motorbike?

Fausto, thank you for also accepting me for this PhD position. We did not collaborate much, but I enjoyed our informal talks during the car rides to the MicroSynC meetings, borrels and group outings. Also thank you for allowing me to organise the group outings and borrels, they really created a nice atmosphere in the SPE group.

Diana, I would not only like to thank you for being in my committee, but also for helping me with learning about microbiology, which was a complete new field to me. You allowed me to come over to Wageningen and with the help of Timon to learn how to work with the microbes and

helped me to organise my results.

I would also like to thank the remainder of the committee: Professor van Sint Annaland, Professor Deen and Professor Hinrichsen; for taking the time and effort to attend my defense and for reading my thesis.

A big shout-out to the SPE staff, which made my journey much more pleasant. Carlo, without your help designing the nice SDB set-up, it would have taken much longer to order and design all the parts in the set-up. Thank you for always be ready to help and thinking with me for the best solutions, even when it was 7:30 and you were still removing your jacket. You can now take some rest without my endless interruptions and questions. I enjoyed our talks and I wish you all the best with your nice camper and maybe we will see each other in one of the "crossjes" of 2024. Erik, I want to thank you for helping me with all the mechanical work. You really took the effort in making everything perfect and paid attention to all the small details, I also appreciated that you were learning me how to do these things myself in the best way possible. I also enjoyed our talks about motorbikes, it was nice to see someone with the same passion. Joris, we did not work together that much, but I enjoyed your dark humor and the borrels together. Madan, I want to wish you first of all a happy retirement and I want to thank you for all your help regarding the assembly/disassembly of the reactors. You really knew all the details and exactly what to do when strange sounds were coming from somewhere and how to fix it. Marlies, thank you for the nice talks at the coffee machine or in the corridor and all the help with installing the GC and with creating the HPLC methods. Without your expertise, I would not have been able to analyse my products in this way. Peter, I think that Consort is losing a lot of money without me continuously breaking their pH probes. Thank you for all the help regarding the pH probes, gas bottles and it was nice that they still send the resazurin with only 2.5 years delay. I appreciated our moments in the F.O.R.T. and at the borrels. Last but definitely not least, Saskia I want to thank you for all the help. You really pushed everything forward and made sure that every little thing was arranged during my PhD. I really enjoyed all our talks about everything that was possible and that I could always come to your office when I needed a break and a quukske.

Throughout this journey I had the opportunity to work with some amazing students who pushed me everyday to keep on learning, improving and helped me put together this thesis. Aram, you were my first student and were given a project that eventually was harder than I anticipated. However, you worked very hard in the lab and helped me set-up the correct method, which eventually lead to the results in Chapter 3. We had some

nice conversations and moments on Stratum as well pre-COVID times, thank you for your work. Usama, I had the pleasure to help you get your Batchelor degree and in return you gave me a nice model and the results that are presented in Supporting Information A.2, thank you for the hard work. Matthijs, unfortunately we did not meet each other in person that often due to the COVID situation. However, you did amazing work in OpenFOAM and created the foundation for Chapter 4. Additionally, in collaboration with Arturo you created the contents for Chapter 5 also. I was very impressed by your work and I would like to thank you a lot for the work. Raoul, I think your thesis should have called "The experimental validation of Murphy's law". However, every time that something did not work, broke or just did not made any sense, you always found a way to keep your head high and come with a solution. You were an amazing student, with lots of motivation and perseverance and without your help I would never have been able to get the microbes to work and put down the foundation of chapter 2 and 6. Even when we were working some days 12 hours and during some holidays, you kept motivated and with that you also kept me motivated. I also really enjoyed our moments in the lab, during the coffee breaks and drinks, thanks a lot for your devotion to the project. Mitchell thank you for your work on the spinning disc with the microbes, unfortunately it did not work out that well. Rick, I was very impressed with how fast you were able to understand the code from Matthijs and adapted it into what it is currently. You were very hard working and even wrote the paper of Chapter 4 with me together. Additionally, you also improved the simulation for Chapter 5 and made the entire shear stress analyses of Chapter 6 on your own. The amount of work you delivered was very impressive and I want to thank you for that and also the informal talks we had. Boris, when I finally thought that, with the knowledge from Raoul, I had the microbes under control, unfortunately it appeared not to be the case. However, this did not stop you from making it work perfectly. Your adjustments to the process made big improvements and allowed us to write down a publication based on Chapter 2. Your hard work and detailed adaptations created a much better understanding of the microbes and your results contributed to Chapter 6 as well. I really enjoyed the moments in the lab and the social gatherings, thank you. Pim, unfortunately your project changed a few times due to delivery times and other problems, however you still worked hard and made a nice Batchelor thesis. Walter and Maurits, even though your work is not presented in this thesis, I want to thank you for the hard work.

I would like to thank my paranymphs Arnab and Brandon. Brandon,

we started this journey together in the Masters and we are finishing it together. You were always a great support and we had many amazing nights in the F.O.R.T., outings, stratum and basically every activity where we went to. We were going full beast mode in the gym, at the groene toren during COVID and in the gym again. I am really proud to call you one of my best friends and I am sure we will have many more moments together. Dr. (B)Arnab, first of all I want to thank you for being my self-proclaimed (by me) supervisor and for all the collaborations that we did together. You also helped me a lot with my writing and designing my thesis. Additionally, we had some great memories during our nightly endeavors. You were a true friend and inspiration to me, thank you for everything.

I want to say thank you to my co inhabitants of STW 1.25, Alexei and Roel. Alexei, my climbing partner and multiple times an almost winner of the famous push-up competition. We had some great times together and I really appreciated you being my office mate. I wish you all the best and I miss our climbing experiences. Roel, it was always nice to talk about sports as we had some common interests, climbing and (mountain) biking. I really appreciated that you got me into DENS and am sad that is eventually didn't work out. Also, I want to thank you for helping me with some small administrative work in the beginning of my PhD and to choose the right parts for my workstation.

I would also like to thank all the people from SPE who were present during this journey and the outings, coffee breaks, drinks and activities. Adarsh Patil, thanks for the fun moments we had in the corridor. Thank you for always be willing to help and making the department less serious. Alperen, our journey started during the HBO already and continued throughout the TU/e. I want to thank you for all the memories and being around as a friend. Anke, I want to thank you for introducing me to the HIIT, it got me addicted and after four years it is still a nice relief. You also brought a lot of energy when we went partying and especially with the famous headshots. Amin, thank you for joining the countless smoke brakes with Arnab and the nice discussions about whatever was going on at that time. Arturo, I want to thank you for all your help and believing in me. You were one of the few people who thought it was possible to simulate the rs-SDR and from that believe, a paper was published. Thank you also for the good times we had and the conversations. Carola, we also started this journey at the same time and had some good times. You were always in for the outings and for the well deserved breaks. Thank you for your kindness, willingness to listen and distraction from all the work. We really had some good memories during this journey and maybe you can still join one of

the HIIT sessions or buy your own squash racket. Jasper, it was always nice hanging out with you. We had some good game nights during COVID times and you were always in for a drink. I enjoyed your company and the dinners we had, as well as our "serious" drunk conversations we had. Thank you for being there. Vishnu, thank you for always bringing a positive vibe. Keep your smile up man, you are a nice guy, unless you put your music up on a road trip. Roy, you were my Master supervisor and asked me to continue doing a PhD. Without you asking/believing in me, I would not have considered doing a PhD and never would have come this far, thank you for that. Rylan, even though your time over here was short, we had some amazing times. You did also some amazing work and I promise you that those publications are still coming.

All the other people that I did not work with directly, I want to thank you all for being at there in the coffee/lunch breaks, going to the F.O.R.T. and to stratum. We had some amazing times and I am sure, this atmosphere will continue without me.

I want to give a special thanks for the help of some people outside the SPE department. Maike, thank you for helping me structure, organise and the input for adaptations on the CFD work. Your expertise in OpenFOAM helped me publish Chapter 4 and to finish the work of Chapter 5. Timon, without my "internship" with you and the meetings we had about the microbes, I would not have been able to make them grow. Thank you for taking the time to teach me and sending the vitamin/trace solutions for the growing medium. James, I want to thank you for the acetic acid trick. Adding a small amount to the initial growing medium sped up the growing process significantly and made the staring phase more consistent. Martijn, I want to thank you for taking the time to give your input on the paper from Chapter 2. This made the article much better.

To the gang from Dongen, thanks for the distractions and keeping me sane. En nou is deze jonge officieel een doctor. Also, thank you Nick for our dinners that somehow always ended up discussing about LES and giving me ideas to try.

I would like to thank my parents for always believing in me, even when I thought that I was not good enough and listening to my complaints about what was going on in this place. I would also like to thank Hedi, Pedro and Daphne for supporting me.

A special thanks to Anke, you were always there for me when I needed. Even when I was stressing and not that fun or talkative anymore. You got me through the tough times and cheered me up when needed, thank you and I love you.

About the Author

Christianus Johannes Wouterus (called Vince) Hop was born on the 1st of April, 1995, in Dongen, the Netherlands. After finishing high school in 2012, he started studying Chemische Technologie at the Avans Applied University in Breda and graduated in 2016. As a follow up, he finished his Pre-Master, Chemical Engineering and Process Technology, at the Technical University of Eindhoven (TU/e) in 2017. He continued his studies at TU/e in the master track, Chemical Engineering, and defended his master thesis titled "A detailed numerical study on the micromixing behavior of turbulent flow fields at low Schmidt numbers" under the supervision of prof.dr.ir. J. van der Schaaf and ir. R. van Kouwen in 2019. He started his PhD in May 2019 in the Sustainable Process Engineering group (subgroup Chemical Reactor Engineering) under the supervision of prof.dr.ir. J. van der Schaaf, in the MicroSynC consortium. This resulted in his PhD thesis titled "Rotor-Stator Spinning Disc Reactor - A Study on the Use in Fermentation Processes". Since June 2023, Vince is employed at Process Design Center.